

The influence of interfacial heat transfer on stable flame propagation in small channels

Graeme Mark Glean Watson



Department of Mechanical Engineering
McGill University
Montreal, Canada

August 2012

A thesis submitted to McGill University in partial fulfillment of the requirements for the degree of Doctor of Philosophy.

© 2012 Graeme Watson

Abstract

Flames in heated tubular channels, with radii on the order of the flame thickness, are investigated experimentally and numerically to understand the various effects of flame / wall interfacial heat transfer. First, combustion is studied in a burner-stabilized configuration, with an imposed temperature profile along the tube wall, to isolate and understand the role of flame / wall heat loss, without heat recirculation. The flames are found to be influenced by competition between energy required to preheat the reactants, heat released by combustion, and heat lost to the wall.

To model such flames, an extension to the standard 1-D, volumetric formulation is proposed which uses detailed chemistry, mixture-averaged transport, and an interfacial heat transfer sub-model. The interfacial heat transfer sub-model uses a non-linear, radially-varying heat source to account for combustion and captures enhanced interfacial heat transfer inside the reaction zone. The degree of heat loss in the reaction zone is found to be sensitive to non-linear heat release. Heat release, from chemical reactions, acts as a local thermal discontinuity resulting in steep temperature gradients and high heat loss. This is absent in present volumetric formulations and in standard interfacial heat transfer correlations; which do not account for chemical reactions and treat the flow as thermally fully-developed.

The model is, then, validated with experiments. In the experiments, strongly burning, axisymmetric methane / air flames, stabilized inside the wall temperature profile, are found to be “flat” for sufficiently small tube dimensions. The extended model is also found to be in agreement with experimental results and gives improved quantitative predictions for flame stabilization position, compared to the standard volumetric approach.

Temperature and species profiles are also compared to those obtained from a detailed multi-dimensional formulation; which is assumed to predict the actual structure of the flame. Again, the extended volumetric model shows significant improvement compared to the standard formulation. Deviations between the extended model and the detailed model are also investigated to determine the nature of the unconsidered multi-dimensional effects.

Finally, propagation and extinction in a participating channel is modeled to understand the combined effects of flame / wall heat transfer and heat recirculation on burning rate. These phenomena are deemed to be the leading-order effects for this case. The interfacial heat transfer sub-model is reformulated to use a non-linear heat source, for combustion,

and radial convection, for flow redirection. The model is evaluated for stoichiometric flames over a range of channel inlet flow velocities and confirms the existence of regimes for fast and slow flame propagation, which have non-monotonic variation for burning rate. Peak heat loss is also found to coincide with peak heat release, rather than the maximum temperature location. The numerical model is, once again, found to give improved quantitative predictions over other approaches which neglect the effects of heat release, without the additional computational cost of multi-dimensional, detailed simulations.

Abrégé

Les flammes réalisées à l'intérieur de canaux tubulaires chauffés sont étudiées expérimentalement et numériquement pour comprendre les effets du transfert de chaleur entre la flamme et la paroi. Tout d'abord, le processus de combustion est étudié dans une configuration de brûleur à flamme stabilisée, avec un profil de température imposé le long du tube. Ceci permet d'isoler et de comprendre le rôle de la perte de chaleur de la flamme vers la paroi, sans recirculation de la chaleur. Il est alors observé que les flammes sont influencées par la compétition existant entre l'énergie requise pour le préchauffage des réactifs, la chaleur dégagée par la combustion, et la perte de chaleur.

Pour modéliser ces flammes, une extension à la formulation volumétrique et unidimensionnelle, typiquement utilisée, est proposée. Cette nouvelle formulation inclue la chimie détaillée, le transport moyenné du mélange, et un sous-modèle de transfert de chaleur interfaciale. Le sous-modèle de transfert de chaleur interfaciale utilise une source de chaleur non-linéaire pour tenir compte de la combustion, et saisit l'effet de transfert de chaleur interfaciale à l'intérieur de la zone de réaction. La quantité de perte de chaleur dans la zone de réaction se trouve à être sensible au dégagement de chaleur non-linéaire. Le dégagement de chaleur lié aux réactions chimiques agit comme une discontinuité thermique locale, entraînant des gradients de température importants et une perte de chaleur. Ceci est absent des formulations volumétriques typiques et des corrélations de transfert de chaleur standard, qui ne tiennent pas compte des réactions chimiques, et traitent l'écoulement comme thermiquement établi.

Le modèle est ensuite comparé à des expériences. Dans les expériences, des flammes axisymétriques à brûlage fort, de méthane et d'air, sont stabilisées le long du profil de température de la paroi. Les flammes sont plates pour les tubes de petites dimensions. Le modèle nouveau est en accord avec les résultats expérimentaux et donne des prédictions améliorées pour la position de la flamme, par rapport à l'approche volumétrique standard.

Les profils de température et d'espèces chimiques sont également comparés à ceux obtenus à partir d'une formulation détaillée multidimensionnelle, qui hypothétiquement prédit la structure réelle de la flamme. Encore une fois, le nouveau modèle volumétrique montre une amélioration significative par rapport à la formulation standard. Les écarts entre le nouveau modèle et le modèle détaillé sont également étudiés afin de déterminer la nature des effets multidimensionnels non-considérés.

Finalement, la propagation et l’extinction de la flamme, dans un canal participant, est modélisé pour comprendre les effets du transfert de chaleur et de la recirculation de la chaleur sur la vitesse de combustion. Le sous-modèle de transfert de chaleur interfaciale est reformulé afin d’utiliser une source de chaleur non-linéaire, pour la combustion, et de convection radiale, pour la redirection de l’écoulement. Le modèle est résolu pour les flammes stoechiométriques à différentes valeurs de vitesses d’entrée, et confirme l’existence de régimes de propagation rapide et lente, qui présentent une variation non-monotone de la vitesse de combustion. Aussi, la perte de chaleur maximale coïncide avec le dégagement de chaleur maximal, et non avec le point de température maximale. Le modèle numérique implémenté démontre, une fois de plus, une amélioration des prédictions quantitatives par rapport aux autres approches qui négligent les effets du dégagement de chaleur, sans le coût de calcul supplémentaire lié aux simulations multidimensionnelles détaillées.

Acknowledgments

I received a tremendous amount of help and support over the course of this project. This dissertation would not have been completed without the following.

I have benefited greatly from the knowledge and expertise of my advisor Dr Jeffrey Berghorson. He gave me the freedom to pursue my own ideas, which at times was difficult and frustrating, but ultimately led to a deeper understanding that I would, otherwise, not have obtained. I also thank other members of the Alternative Fuels Lab (AFL) for many helpful discussions and their suggestions. In particular, I acknowledge George Gauthier, who performed the detailed multi-dimensional simulations included in this dissertation. The results from this model were important for understanding the multitude phenomena at play in flame-in-channel problem and our discussions led to large improvements in the quality of this research.

Special thanks to the technicians, machinists and office staff at McGill who provided critical support. First, I thank Georges Kopp for assistance in building the quartz channels used in the experiment. The experiment would not have been possible without these critical pieces. Mario Iacobaccio and George Tewfik were instrumental in providing electronics support. Experiments would not have been a success without Gary Savard, Tony Micozzi, Andy Hofmann, John “The Dungeon Master” Boisvert, Raymond Lemay, and Sam Minter who provided a multitude of technical help, design experience, and machining support. The 1337, Jeffrey McDonald and Vladimir Timochevski at CLUMEQ support also deserve acknowledgment. Finally, I thank the office staff, particularly Barbara Lapointe, who helped with the multitude of paperwork and kept things running so that we can focus on research.

The models developed as part of this thesis are built on top of software packages which are freely available. Model development would not have been possible without the CANTERA software package developed by David Goodwin, SUNDIALS by Alan Hindmersh, and OPENFOAM created by Henry Weller. I am also indebted to the GNU scientific library community for developing a versatile, and quick, mathematical library. The fact that these powerful packages exist at all, and are offered “free” and open-source, is a testament to their generosity, and is a boon to scientific research.

The AFL hosts undergraduate research scholars in the school year and during the summer; many of whom offered assistance as well as invaluable ideas. Thanks to Gavin Fried-

man, Lim Gyu-Hyeong and Gideon Balloch.

Finally, but not least, I thank my family for their constant support over these years. I especially wish to thank my wife, Patricia Pernica, whose support was critical for completing this degree. She has kept me sane, even in my darkest times, and our daily Skype “hangouts” are always the highlight of my day.

Computing resources for this study were provided by the “Consortium Laval, Université du Québec, McGill and Eastern Quebec” (CLUMEQ). Funding from the Natural Sciences and Engineering Research Council of Canada and additional funding from the “Fonds Québécois de la Recherche sur la Nature et les Technologies” is also acknowledged.

Graeme M.G. Watson

Contents

1	Introduction	1
1.1	Fundamentals	4
1.2	Excess enthalpy burning	5
1.3	Non-equilibrium considerations	7
1.4	Interfacial heat transfer	11
1.5	Heterogeneous chemistry	13
1.6	Flame curvature	15
1.7	Methodology	18
2	Stationary flame in a steady wall temperature profile	20
2.1	Problem formulation	21
2.1.1	Bulk parameters	22
2.2	Solution from an asymptotic model	23
2.3	Numerical model	25
2.3.1	1-D, volumetric flame	25
2.3.2	Interfacial heat transfer sub-model	27
2.3.3	Source convolution profile	30
2.4	Assembly of the model	34
2.5	Solution profiles	35
3	The effect of chemical energy release	39
3.1	Solution with frozen chemistry	40
3.2	Solution with combustion	43
3.3	The weak flame	48

4	Experimental investigation	52
4.1	The apparatus	52
4.2	Wall temperature profile	56
4.3	Flame stabilization and curvature	57
4.4	Uncertainties due to local wall heating	58
4.5	Model validation	61
4.6	Conclusions	66
5	Detailed simulations	67
5.1	The detailed numerical model	68
5.1.1	Discretization and solution procedure	69
5.1.2	Transport and chemistry	70
5.1.3	Reduced kinetics mechanisms	71
5.2	Summary of data for stabilization position	73
5.3	Comparison of the models	75
5.3.1	Solution contours	75
5.3.2	Species profiles	78
5.3.3	Momentum	79
5.4	Conclusions	82
6	Propagating flame in a participating channel	84
6.1	Solution from an asymptotic model	85
6.2	Volumetric model with detailed chemistry	87
6.2.1	1-D, volumetric flame	88
6.2.2	Interfacial heat transfer sub-model	89
6.3	Representative solution profiles	91
6.3.1	Bulk profiles	91
6.3.2	Radial profiles	93
6.4	Global solution results	95
6.4.1	Isothermal walls	95
6.4.2	Participating walls	97
6.4.3	Influence of wall properties	100
6.5	Conclusion	101

7	Conclusions	103
7.1	Synopsis	103
7.2	Contributions	105
A	Analytical models	107
A.1	Stationary flame in a steady wall temperature profile	107
A.2	Propagating flame in a participating channel	111
B	Furnace heat transfer analysis	117
C	Mixture composition	125
D	Solution of the channel boundary layer equations	130
E	Model sensitivity	134
F	Flame Simulations	137
F.1	Flame solution scripts	137
	References	145

List of Figures

1.1	The principle of excess enthalpy burning, (a) conventional flame, (b) high temperature flame with preheating, (c) excess enthalpy flame with heat recirculation. Figure adapted from [1].	6
1.2	Combustion modes for propagating flames in a heat recirculating channel: (a) counter-current flame propagation, (b) concurrent flame propagation. Profiles are generated from the asymptotic model of Ju and Xu [2]. Temperatures are normalized by the inlet and adiabatic flame temperatures, $(T - T_u)/(T_{af} - T_u)$	8
1.3	Quenching distances, D_q , of reactive and inert stainless steel plates with wall temperature, T_w . Figure adapted from [3].	14
1.4	Quenching distances, D_q , of reactive and inert quartz plates with wall temperature, T_w . Figure adapted from [3].	15
1.5	Structure of adiabatic flames for selected values of S_u/S_L . $\varepsilon = 0.1$ (thin line) and 1.0 (thick line). The flames are represented by isotherms $\theta = 0.4$ and 0.8. Here, r is a channel half-width. Figure adapted from [4].	16
1.6	Normalized burning rate, Ω , versus inlet flow speed, S_u/S_L , for adiabatic flames with differing ε . The dashed lines are based on a two-dimensional, thermo-diffusive formulation. The solid line is based on leading terms in an asymptotic formulation for $U/S_L \rightarrow 0$ and $\varepsilon = O(1)$. Figure adapted from [4].	17

2.1	Global solution behaviour from an asymptotic model for a flame stabilized in a channel with a axial wall temperature gradient. Normalized inlet velocity, S_u/S_L , and flame / wall temperature difference, $\theta_f - \theta_w$, as a function of dimensionless stabilization position, ξ_f . $S_L = 0.18$ m/s, $T_u = 300$ K, $T_{af} = 1800$ K, $Nu = 4$, $Le = 0.9$, $\beta \rightarrow \infty$	23
2.2	Structure of a 1-D, lean, adiabatic methane / air flame, $\phi = 0.7$. Profiles for temperature, T , heat release, Q_{rxn} , CH_4 and O_2 species, and a progress variable for bulk chemical enthalpy, Z	32
2.3	Normalized bulk gas temperature, T , heat source, Q_s , and Z profiles. $\phi = 1.0$, $S_u = 0.85$ m/s, $T_u = 300$ K, $T_{af} = 2223$ K, $Le = 1.0$	36
2.4	Effect of Lewis number, Le , on ζ (left) and normalized gas temperature, $(t - T_u)/(T_{af} - T_u)$ (right) profiles from interfacial heat transfer sub-models with chemical energy release. Heat release contours, Q_{rxn} , are also superimposed as thick lines. Temperature contours are $0.5T_{af} \leq t \leq 0.85T_{af}$ in intervals of $0.05T_{af}$. ζ contours are $0.9 \geq \zeta \geq 0.3$, decreasing in intervals of 0.1 . Heat release contours are $fQ_{rxn}/Q_{rxn,peak} = 0.5, 0.75, 1.0$ and 1.25 . $\phi = 1.0$, $S_u = 0.85$ m/s, $T_u = 300$ K, $T_{af} = 2223$ K, $Le = 1.0$	37
3.1	Simulated gas (—) and wall temperature profiles (— —) for a non-reacting flow (air). The gas/wall temperature difference, $T - T_w$, is plotted below for reference. $\phi = 0.0$, $S_u = 1.00$ m/s, $T_u = 300$ K.	40
3.2	Radial gas temperature, $t(r, z)$, profiles for a non-reacting flow (air). These profiles are normalized by the bulk gas temperature, $T(z)$. $z_1 = 0.001$ m, $z_2 = 0.011$ m, $z_3 = 0.396$ m, $z_4 = 0.509$ m. $\phi = 0$, $S_u = 1.00$ m/s, $T_u = 300$ K.	41
3.3	Simulated Nusselt number profile, Nu_z , for a non-reacting flow (air). The Nusselt number settles to a, more or less, constant value of $Nu_z = 4.34$ downstream of z_0 . $\phi = 0$, $S_u = 1.00$ m/s, $T_u = 300$ K.	42
3.4	Simulated gas bulk temperature, T , profiles from models which use an interfacial heat transfer sub-model with frozen chemistry (thin line) and with heat release, $Le = 1.0$ (thick line). $\phi = 1.0$, $S_u = 0.85$ m/s, $T_u = 300$ K, $T_{af} = 2223$ K. Detailed chemistry is provided by the GRI-Mech 3.0 kinetics mechanism [5].	44

3.5	Radial gas temperature, $t(r, z)$, profiles from the interfacial heat transfer sub-model with heat release, $Le = 1.0$. These profiles are normalized by the gas temperature, $T(z)$. $z_1 - z_f = -2.7$ mm, $z_2 - z_f = -0.5$ mm, $z_3 - z_f = 0.0$ mm, $z_4 - z_f = 1.2$ mm, $z_5 - z_f = 28.4$ mm. $\phi = 1.0$, $S_u = 0.85$ m/s, $T_u = 300$ K.	45
3.6	Comparison of Q_w profiles obtained from interfacial heat transfer sub-models which neglect (thin line) and include heat release, $Le = 1.0$, (thick line) to calculate interfacial gas/wall energy heat transfer. $\phi = 1.0$, $S_u = 0.85$ m/s, $T_u = 300$ K.	46
3.7	Local Nusselt number, Nu_z , profile from the interfacial heat transfer sub-model with heat release, $Le = 1.0$. $\phi = 1.0$, $S_u = 0.85$ m/s, $T_u = 300$ K.	47
3.8	Simulated bulk temperature, T , heat release, Q_{rxn} , Z and a selection of species profiles for weak, stoichiometric n – C ₇ H ₁₆ /air combustion. $\phi = 1.0$, $S_u = 2.0$ cm/s, $T_u = 300$ K. An interfacial heat transfer sub-model is used with heat release, $Le = 1.0$ (thick lines), or frozen chemistry (thin lines) to model interfacial heat transfer. The positions z_1 , z_2 and z_3 show the locations of peak heat release for the cool, blue and hot flames, respectively.	49
3.9	Locations of peak heat release for weak, stoichiometric n – C ₇ H ₁₆ /air combustion at low inlet flow velocities, S_u . An interfacial heat transfer sub-model is used with frozen chemistry (open circles) or with heat release, $Le = 1.0$ (closed circles) to model interfacial heat transfer. Dashed lines to the left and right of the model with heat release show the limits $Le = 0.0$ and $Le \rightarrow \infty$, respectively.	50
4.1	Schematic of apparatus. A detailed view of the furnace assembly is in Figure 4.2.	53
4.2	Schematic of furnace assembly. The schematic is not to scale.	54
4.3	Measured wall temperature profile, $T_w(z)$. Measured data points are the open squares in this figure. The length of the profile and the maximum wall temperature is $z_b = 0.5714$ m and $T_{w,b} = 1312$ K, respectively. The measurements are fit via linear regression by two sigmoidal profiles (—) which are connected at z_0 for input into the computational model. The inside tube diameter is 1 mm.	56

- 4.4 CH emission from stoichiometric flames in the heated channel ($D = 2$ mm). The solid and dashed lines show the approximate positions of the inner and outer walls of the tube, respectively. Flames move further downstream with increasing flow velocity, however the actual change in position between these cases is on the order of 1 cm, which is larger than what is depicted in this figure. (a) $S_u = 0.7$ m/s, (b) $S_u = 1.0$ m/s, (c) $S_u = 1.4$ m/s. 57
- 4.5 $\phi = 1.0$, $S_u = 0.80$ m/s, $T_u = 300$ K. Position of peak CH location versus time for one experimental trial. The experimental track (squares) captures flashback, stabilization between $z_{f,u}$ and $z_{f,d}$, and the subsequent wall-controlled flame propagation due to local wall heating. $z_{f,u}$ is at the intersection of a fitted polynomial and straight line (—). The velocity thresholds for $z_{f,d}$ are $10S_f$ and $100S_f$. For this trial, the final countercurrent propagation speed after stabilization is $S_f = 1.4 \times 10^{-5}$ m/s, or less than 0.002% of the inlet flow velocity. 59
- 4.6 Inlet flow velocity, S_u , versus simulated (—) and experimentally determined stabilization position, z_f . Experimental data is shown as a range of locations by horizontal lines between the upstream, $z_{f,u}$ (squares), and downstream bounds, $z_{f,d}$ (vertical lines), of the stabilization regime. The thin and thick vertical lines are for $z_{f,d}$ determined at $10S_f$ and $100S_f$, respectively. The model uses an interfacial heat transfer sub-model with frozen chemistry (open circles) or with heat release, $Le = 1.0$ (closed circles), and the GRI-Mech 3.0 kinetics mechanism. Dashed lines to the left and right of the model with heat release show the limits $Le = 0$ and $Le \rightarrow \infty$, respectively. 62
- 4.7 Error in the predicted wall temperature, T_w , at the simulated flame position, $z_{f,sim}$, compared the experimental flame, z_f , for a variety of detailed kinetics mechanisms. Legend as in Figure 5.2. The shaded error band represents the $\pm 2\sigma$ total uncertainty in the model with heat release due to experimental operating parameters and measured boundary conditions using GRI-Mech 3.0 as the reference. 64
- 5.1 Computed structure of a stoichiometric, adiabatic, planar flame at standard inlet conditions, $T_u^\circ = 298$ K, $p^\circ = 1$ atm: temperature, major species, radicals and heat release. 72

5.2	Inlet flow velocity, S_u , verses simulated wall temperature at the flame stabilization position, $T(z_f)$, in a $D = 1$ mm tube. Models are the 1-D volumetric model which uses $Nu = 4.0$ (squares) and a solution for interfacial heat transfer which incorporates heat release, $Le = 1.0$ (triangles), and the detailed model (circles).	74
5.3	Computationally derived flame temperature structure from the volumetric model, with the standard $Nu = 4.0$ assumption, the volumetric model with an interfacial heat transfer sub-model, with heat release, and the detailed model. $\phi = 1.0$, $S_u = 0.85$ m/s.	75
5.4	The two center plots show a comparison of the contour profiles obtained from a volumetric flame model coupled to an interfacial heat transfer sub-model with heat release ($Le = 1.0$), and the detailed model in a $D = 1$ mm tube: $\phi = 1.0$, $S_u = 0.85$ m/s. The plot shows identical Q_s (thick line) and ζ (thin line) contours in the left plot and the identical gas temperature, $t - T_w$, contours in the right plot. ζ contours are $0.9 \geq \zeta \geq 0.3$, decreasing in intervals of 0.1. Heat release contours are $fQ_{rxn}/Q_{rxn,peak} = 0.5, 0.75, 1.0$ and 1.25. The two plots are flanked by ζ (thin line) and Q_s (thick line) solutions from the volumetric model at the extremes of Lewis number, Le	77
5.5	2-D, axisymmetric contours of the permanent and intermediate species predicted by the detailed model. $\phi = 1.0$, $S_u = 0.85$ m/s.	78
5.6	Comparison of bulk species profiles: Permanent species, radials and intermediate species. Operating conditions as in Figure 5.5.	80
5.7	2-D, axisymmetric contours of free radicals from the detailed model. Operating conditions as in Figure 5.5.	81
5.8	Deviations in axial (a) and radial (b) mass flow from an assumed parabolic profile. Profiles are extracted from the detailed model at axial locations $z - z_f = -0.5, -0.1, 0.0, 0.1, 2.0$ mm. $\phi = 1.0$, $S_u = 0.85$ m/s.	81
6.1	Dependence of normalized burning rate, S_b/S_L , on dimensionless interfacial heat transfer coefficient, H , for multiple forced inlet flow speeds, S_u/S_L in a participating channel. $S_L = 0.18$ m/s, $T_u = 300$ K, $T_{af} = 1800$ K, $Nu = 4$, $Le = 0.9$, $\beta \rightarrow \infty$	85

6.2	Dependence of flame burning rate, S_b/S_L , on inlet flow speed, S_u/S_L for fixed dimensionless interfacial heat transfer coefficients, H for strongly-burning flames. Flame profiles (a) and (b) for fast and slowly-propagating flames are shown in Appendix A.2. $S_L = 0.18$ m/s, $T_u = 300$ K, $T_{af} = 1800$ K, $Nu = 4$, $Le = 0.9$, $\beta \rightarrow \infty$	87
6.3	Typical profiles for a fast-propagating methane / air flame ($\phi = 1.0$) near a quartz channel wall, $S_u = 1.5$ m/s, $T_\infty = 1100$ K, $r_w = 1.0$ mm, $r_\infty = 1.5$ mm.	92
6.4	Typical profiles for a slowly-propagating flame, $S_u = 3.5$ m/s. Solution parameters as in Figure 6.3.	93
6.5	Axial velocity, u/S_L , and temperature, $(t - T_\infty)/(T_{af} - T_\infty)$, profiles for a fast (thin line) and slowly-propagating (thick line) flames. Solution parameters as in Figures 6.3 and 6.4.	94
6.6	Simulated quenching curves for stoichiometric freely-propagating flames in an isothermal channel, $T_w = 1100$ K. Constant Nu curves, from left to right, are $Nu = 4, 5, 10, 20, 30, 40, 50, 100$	96
6.7	Burning velocities for stoichiometric propagating flames opposed by inlet mass flow. Solution parameters as in Figure 6.3.	98
6.8	Interfacial heat transfer profiles for volumetric models. Solution parameters as in Figure 6.3.	99
6.9	slowly-propagating regime for quartz, alumina, and silicon carbide walls. Solution parameters as in Figure 6.3.	101
A.1	Typical profiles obtained from the propagating solution: (a) fast flame, (b) slow flame.	114
A.2	Solution for normalized burning rate versus dimensionless interfacial heat transfer coefficient, H , for the Spalding [6] solution of a flame in an isothermal channel. The value S_{cr} represents the critical burning rate where extinction occurs.	116
B.1	Fundamental cell geometries: (a) unit cell of concentric cylinders [7], (b) offset cylinders [8] separated by a distance, L , and (c) parallel cylinders [9].	119
B.2	Unit cell stack for calculation of radiant furnace and tube view factors, of N faces.	119

B.3	Predicted furnace surface, T_{rad} , and tube wall, T_{w} , temperature profiles compared to experimentally obtained temperatures (squares) for the tube wall.	120
B.4	A code to calculate furnace and tube view factors.	122
B.4	View factor code, continued.	123
B.4	View factor code, continued.	124
C.1	Experimental (symbols) and simulated (lines) trends in flame stabilization wall temperature, $T_{\text{w}}(z_{\text{f}})$, due to flame speed, S_{L} . Stoichiometric (\circ) mixture A, lean (\square) mixture B, rich (\diamond) mixture C. Three images of the stoichiometric flame front, which becomes more curved with increasing inlet velocity, are also shown.	126
C.2	Experimental (symbols) and simulated (lines) trends in flame stabilization wall temperature, $T_{\text{w}}(z_{\text{f}})$, with flame speeds, S_{L} , matched via nitrogen-to-oxygen ratio. (a) Lean (\square) mixture B is matched with stoichiometric (\circ), diluted mixture D. Rich (\diamond) mixture C is matched with stoichiometric, diluted mixture E. (b) Stoichiometric mixture A is matched with lean, enriched mixture F and rich, enriched mixture G.	127
C.3	Experimental (symbols) and simulated (lines) flame stabilization wall temperature, $T_{\text{w}}(z_{\text{f}})$, verses inlet flow velocity of S_{u} . Flame thickness is given in terms of the dimensionless value, $\varepsilon = \delta_{\text{f}}/r_{\text{w}}$. Legend as in Figure C.2. . . .	129
D.1	Stencil for the finite-difference representation of the DAE system for the channel boundary layer. The solution procedure is the Method of Lines. . .	133
E.1	Flame stabilization position logarithmic sensitivities to the boundary conditions of models which use a boundary layer for interfacial heat transfer with frozen chemistry (white) and with heat release, $\text{Le} = 1.0$ (black). $\phi = 1.0$, $S_{\text{u}} = 1.00$ m/s, $T_{\text{u}} = 300$ K.	135
E.2	Flame propagation speed logarithmic sensitivities to the boundary conditions for freely-propagating slow fast (white) and slow (white) flames, $\text{Le} = 1.0$, $\phi = 1.0$, $T_{\infty} = 1100$ K.	136
F.1	Script for a flame stabilized in a monotonically varying wall temperature profile.	138

F.1	Burner-stabilized flame script, continued.	139
F.1	Burner-stabilized flame script, continued.	140
F.1	Burner-stabilized flame script, continued.	141
F.2	Script for a freely-propagating flame in a participating channel.	142
F.2	Freely-propagating flame script, continued.	143
F.2	Freely-propagating flame script, continued.	144

List of Tables

1.1	Langmuir-Hinshelwood surface reaction mechanisms. * indicates a vacant surface sites, while ()* denotes an absorbed radical.	13
5.1	Comparison of the simulated global parameters of a stoichiometric adiabatic, planar flame calculated from different kinetics models: Laminar burning velocity, adiabatic flame temperature and thermal thickness. The simplified mechanism uses a global reaction where the forward rate is expressed as $k = AT^n \exp(-E_A/RT)[CH_4]^a[O_2]^b$, where $A = 2.29 \times 10^{13} \text{ (kmol cm}^{-3}\text{)}^{-0.5} \text{ s}^{-1}$, $n = 0$, $a = 0.2$ and $b = 1.3$	73
6.1	Wall thermal properties.	100
C.1	Mixture parameters. Normalized equivalence ratio, $\Phi = \phi/(1 + \phi)$. Flame thickness, $\delta_f = (T_{af} - T_u)/(dT/dz _{\max})$. All parameters are calculated from an adiabatic free flame with the GRI-Mech 3.0 kinetics mechanism.	126

Nomenclature

c_p	Specific heat capacity	J/kg/K
D	Diameter	m
\mathcal{D}	Molecular diffusivity	m/s ²
E_A	Activation energy	J/mol
h	Specific enthalpy	J/kg
h	Local heat transfer coefficient	W/m ² /K
h_V	Volumetric heat transfer coefficient	W/m ³ /K
H	Enthalpy	J
$j_{k,i}$	Diffusive mass flux of species k in direction i	kg/m ² /s
p	Thermodynamic pressure	Pa
R	Universal gas constant	J/kmol/K
\dot{q}	Heat flux	W/m ²
q_s	Local heat source	W/m ³
Q_c	Heat of combustion	J / kg
Q_{cond}	Bulk heat transfer by conduction	W/m ³
Q_{inter}	Bulk heat transfer by interspecies diffusion	W/m ³
Q_{rxn}	Heat of reaction	W/m ³
Q_s	Bulk heat source	W/m ³
Q_{th}	Bulk thermal flux	W/m ³
Q_w	Interfacial heat transfer	W/m ³
r	Radial coordinate	m
S_b	Flame burning velocity	m/s
S_f	Flame propagation speed	m/s
S_L	Laminar flame speed	m/s

S_u	Inlet flow speed	m/s
\hat{t}	Time	s
t	Local gas temperature	K
T	Bulk temperature	K
T_A	Activation temperature	K
u	Local axial velocity	m/s
U	Average flow velocity	m/s
v	Local radial velocity	m/s
$V_{k,i}$	Diffusion velocity of species k in direction i	m/s
W_k	Molar mass of species k	kg/kmol
\bar{W}	Mean molar weight	kg/kmol
z	Axial coordinate	m
z_f	Flame stabilization location	m
δ_f	Flame thickness	m
$\dot{\zeta}$	Rate of consumption of ζ	1/s
ψ	Stream function	m ² /s
λ	Thermal conductivity	W/m/K
μ	Viscosity	kg/m/s
ρ	Density	kg /m ³
α	Thermal diffusivity	m ² /s
σ	Stephan Boltzmann constant	W/m ² /K ⁴
$\dot{\omega}$	Net production rate	kg/s
$\dot{\omega}_k$	Production rate of species, k	kmol/m ³ /s
ψ	Stream function	kg/m/s
Δh_f°	Standard enthalpy of formation	J/kg

Dimensionless variables:

a	Reduced reaction enthalpy, $(T_{af} - T_u)/T_{af}$
C	A constant
\mathcal{C}	Heat capacity ratio
f	Heat of reaction convolution profile
H	Bulk heat transfer coefficient

Le	Lewis number, α/\mathcal{D}
Nu	Nusselt number, hD/λ
Pe	Peclet number, UD/α
\mathcal{S}_f	Dimensionless flame propagation speed
\mathcal{S}_u	Dimensionless inlet flow speed
\mathcal{U}	Dimensionless axial velocity
Y	Mass fraction
Z	Bulk progress variable for chemical enthalpy
β	Zeldovich number, $-E_A T_{af}^2/R(T_{af} - T_u)$
ε	Normalized flame thickness, δ_f/r_w
φ	Porosity, ratio of volumes V/V_w
ϵ	Wall surface emissivity
ζ	Local progress variable for chemical enthalpy
θ	Dimensionless temperature
ξ	Stretch coordinate, z/δ_f
ϕ	Equivalence ratio

Subscripts:

af	Adiabatic flame
b	Burned
d	Downstream
f	Flame
k	Index for chemical species
s	Source term
u	Upstream / unburned
w	Wall
∞	Ambient environment
+	Hot side (right)
−	Cold side (left)
\pm	Middle

Chapter 1

Introduction

The study of flames in small channels (in tubes or plates), where the channel has a dimension on the order of the flame thickness, is a fundamental problem in combustion [10]. The earliest investigations were by Davy [11], in which flame propagation was studied in cold channels. When the walls are cold, flame extinction is found to occur when the distance between the channel walls is made small, so that it reaches a critical dimension where the flame can no longer propagate. This dimension is called the quenching distance. Interfacial heat transfer, from the flame to the wall (cooling of the reaction zone), as well as the removal of reactive intermediates are the reasons for extinction. The quenching distance has been measured for a wide variety of hydrocarbon fuel / air mixtures and is on the order of 1–4 mm for standard channel configurations [12]. This principle is used in the design of flame holders, flash-back arrestors and other safety applications.

The concept of quenching distance was so successful that, for some time, there was a generally held view that combustion below the standard quenching distance was not possible [13]. However, other modes of propagation are possible, if controlling parameters are modified in the system. Peak temperatures in a flame are directly related to the energy content of reactants in a fuel / air mixture. In traditional combustion applications, this temperature is the adiabatic flame temperature, T_{af} , which is computed as the equilibrium temperature of a constant-pressure, adiabatic process. When there is significant heat loss in a flame, the peak temperature is found to be lower than the adiabatic flame temperature. Heat loss inhibits the rates of chemical reactions and the burning velocity [14] of a flame. However, in a non-traditional, specially designed burner, it is possible to exceed the adia-

batic flame temperature, by recirculating heat from the products to preheat the reactants. This mechanism effectively generates excess enthalpy in a flame, producing super-adiabatic temperatures and higher burning velocities, which widens flammability limits [1] and reduces the dimensions in which flames can propagate.

A combustion process that exhibits excess enthalpy, via heat recirculation, occurs when a reacting gas mixture flows through small channels in an inert solid medium. These channels have dimensions that are on the order of the quenching distance or less, such that there is high thermal coupling via interfacial heat transfer. For some conditions, it is possible to generate a heterogeneous combustion mode, or filtration wave [15], which consists of a combustion wave in the gas and a thermal wave in the solid. This combustion mode is heterogeneous, not because of the type of chemical reaction, but rather because of the active participation of both the solid and gas phases in the transport of energy to sustain combustion. As a result, filtration waves exhibit phenomena that are typically not observed in homogeneous flames. It is the nature of the flame / wall interaction, via interfacial heat transfer, that changes the nature of wave propagation.

Many burners have been developed which use a flame's proximity to channel walls to "borrow heat" [1] from combustion heat release to sustain chemical reactions. This renders lean mixtures flammable, well outside standard flammability limits [16], and also results in vastly reduced high temperature NO_x pollutants and CO emissions [17]. These ultra-lean, small channel burners also have firing rates which are broader than conventional burners [13, 18]. A notable design which uses this concept is the spiral heat exchanger, or "swiss-roll," combustor [17, 19], in which a well-stirred reaction is stabilized at the centre of a spiral heat exchanger. Such burners have been shown to burn lean mixtures at very low stoichiometry, with almost all heat released being recirculated for preheat.

Reactors for non-catalytic reformation of conventional [20] or bio-fuels [21] into syngas (H_2 and CO), via partial oxidation, is also a promising technology which relies on small channels and energy recirculation to sustain chemical reactions. Reformation requires sustained operation at ultra-rich equivalence ratios, outside conventional flammability limits, for optimum conversion efficiency ($\phi \approx 3$ for methane) [22]. Such conditions are possible when combustion is stabilized in porous media [23–25] and counter-flow [26–29] heat recirculating burners.

There is now recognized potential for such systems. Many *micro-combustors* for power generation, propulsion, chemical sensing, and heating are also currently under development.

Micro gas turbines have been built [30] which are capable of producing up to 50 W of power with as little as 7 g/hr of jet fuel. Researchers have also developed several liquid fueled rotary engines which are also at the micro-scale, based on Wankel rotary motion [31].

There has also been a recent surge of commercial interest in micro-scale combustion devices to replace batteries in portable electronics. This interest is attributed to the high volumetric energy density of hydrocarbon fuels, which are at least two orders on magnitude higher than battery storage devices. Micro-reactors have been coupled to micro-solid oxide fuel cells (SOFCs) [32] to make compact generation systems [33]. With the rapid growth of portable devices, such as cell phones and notebook computers, the market demand for small-scale power generators is expected to grow [34].

There is also interest in micro-satellite thrusters for station keeping, which require small thrust and high specific impulse to have an operational period that could last years. Battery based thrusters do not have the ability to provide this impulse and have excessive thrust-to-weight ratios due to low storage capacities [35].

Micro-sensing and chemical analysis systems also use micro-reactor flow channels for power generation and as a heat source to raise reaction temperatures [36]. The use of ultra-lean combustors ($\phi < 0.06$) as “air filters” to protect against dangerous chemical or biological agents has also been proposed [19].

There are significant technological hurdles that need to be overcome to make such systems marketable. These problems include: material constraints, thermal and chemical stability, and scaling issues due to the large surface-to-volume ratios of small channels. Devices must also be optimised such that peak power corresponds with the maximum attainable efficiency [37]. Some of these gains will come with improved models of the process which lead to a better understanding of the combustion phenomena in such systems.

To facilitate further technological development, there is a need to create simple models that can account for essential phenomena, so that the influence of design parameters can be estimated. The objective of this work is to develop such a model for stable flame propagation in a single channel. This model depends on chemical heat release and on flame / wall coupling by interfacial heat transfer to account for heat loss to the channel walls, and heat recirculation through them, to improve predictions for flame temperature, solid temperature and burning rate.

1.1 Fundamentals

Flames in channels are influenced by phenomena which can either quench or enhance flame propagation and stabilization. Flame dynamics are controlled by thermal-diffusive and hydrodynamic effects, interfacial heat transfer between the gas and channel walls [38], and heat recirculation through them [1, 16], surface reactivity [3], and other phenomena that depend on channel geometry and surface-to-volume ratio [39]. The focus of this dissertation is on interfacial heat transfer. This phenomenon results from energy transfer by conduction between the gas and the solid channel wall, and is the leading-order phenomenon on this system.

There is currently active research to determine the intricate interplay of these phenomena in a unified combustion model. Numerical modeling using computational fluid dynamics (CFD) is an important tool in this effort. The proximity of the wall to the reaction zone generates multiple axial and transverse length scales. Multi-dimensional codes with multi-component physics, transport and detailed chemical kinetics are, therefore, needed to accurately model all phenomena in this problem. Advances in these models have come with increased computational power. Hackert et al. [40] looked at stable combustion in tubes, channels and irregular geometries using a multidimensional code with simplified global chemistry models. Norton and Vlachos [41] then used a similar methodology to carry out a detailed analysis of stable combustion in a single channel, which captured mass and thermal gradients near the channel wall.

Flames in channels also exhibit transient behavior. A thermo-diffusive model was used by Kurdyumov et al. [42] to study stabilized flames when symmetry was not assumed. Asymmetric flame dynamics result that are not found in classical flames. This behavior persists with the inclusion of detailed chemistry and transport. Pizza et al. [43] in a set of articles [43, 44] obtains a range of symmetric and asymmetric structures, and transient dynamics for hydrogen/air flames which is also confirmed in an updated model in three dimensions [45].

It is difficult to isolate the influence of specific physical effects in the above models due to the complex interaction of the phenomena and the number of parameters involved, but interfacial heat transfer is thought to be a principal phenomenon responsible for the observed flame behavior [42].

Others use a combined approach of experiments and simplified models to understand

the underlying physics of this problem [2, 46–48]. These studies suggest that the principal physics which govern the combustion wave are similar to those in classical burner-stabilized flames. As in the classical case, combustion depends on a balance between the rates of heat release and loss in the system. However, it is interfacial heat transfer between the gas and channel wall, and not heat loss to an inlet boundary, which principally governs flame dynamics and stabilization. In a flow channel, this is accomplished through a closed-loop mechanism whereby heat is lost from the flame to the wall via interfacial heat transfer and is then recirculated to preheat the reactants. This produces a concentration of enthalpy in the flame zone and higher burning rates [16]. The experiments of Zamashchikov [49, 50], and Ju and Xu [2] show multiple fast and slow propagation speeds of flames concurrent and counter-current to the inlet flow velocity. Similar behavior is also found in porous media burners [15]. The combustion wave propagates at a steady velocity which depends on tube diameter, inlet flow velocity and the thermal properties of the wall.

The heat transfer problem is further simplified by looking at an open-loop system where the flame is decoupled from heat recirculation by a constant temperature wall [38]. In these systems, the combustion wave stabilizes at a unique location within a steady, monotonically increasing axial wall temperature profile [46].

1.2 Excess enthalpy burning

The principle of excess enthalpy burning is shown in Figure 1.1. In a conventional flame, in Figure 1.1(a), peak temperatures in the combustion zone (F) are directly related to the chemical enthalpy of the reactants, Q_c , stored, initially, in the fuel/air mixture. This energy is converted into sensible heat inside the flame, $\Delta H = H_b - H_u = Q_c$.

The reactivity of a flame is exponentially related to temperature. Therefore, a way to increase burning rate is by injecting sensible heat, Q_r , into the reactants before the flame, raising the initial temperature [51]. This is shown in Figure 1.1(b). The strategy results in higher final temperatures and burning rates [12], but is, overall, inefficient due to the fact that the energy input to preheat the gas is ultimately lost out the outlet of the combustor.

A better way to achieve higher flame temperatures is to lock Q_r in the system by recirculating this heat from the products to preheat the reactants [1]. This can be done using a counterflow heat exchanger, in Figure 1.1(c). This mechanism effectively generates excess total enthalpy in the combustion zone, producing super-adiabatic temperatures.

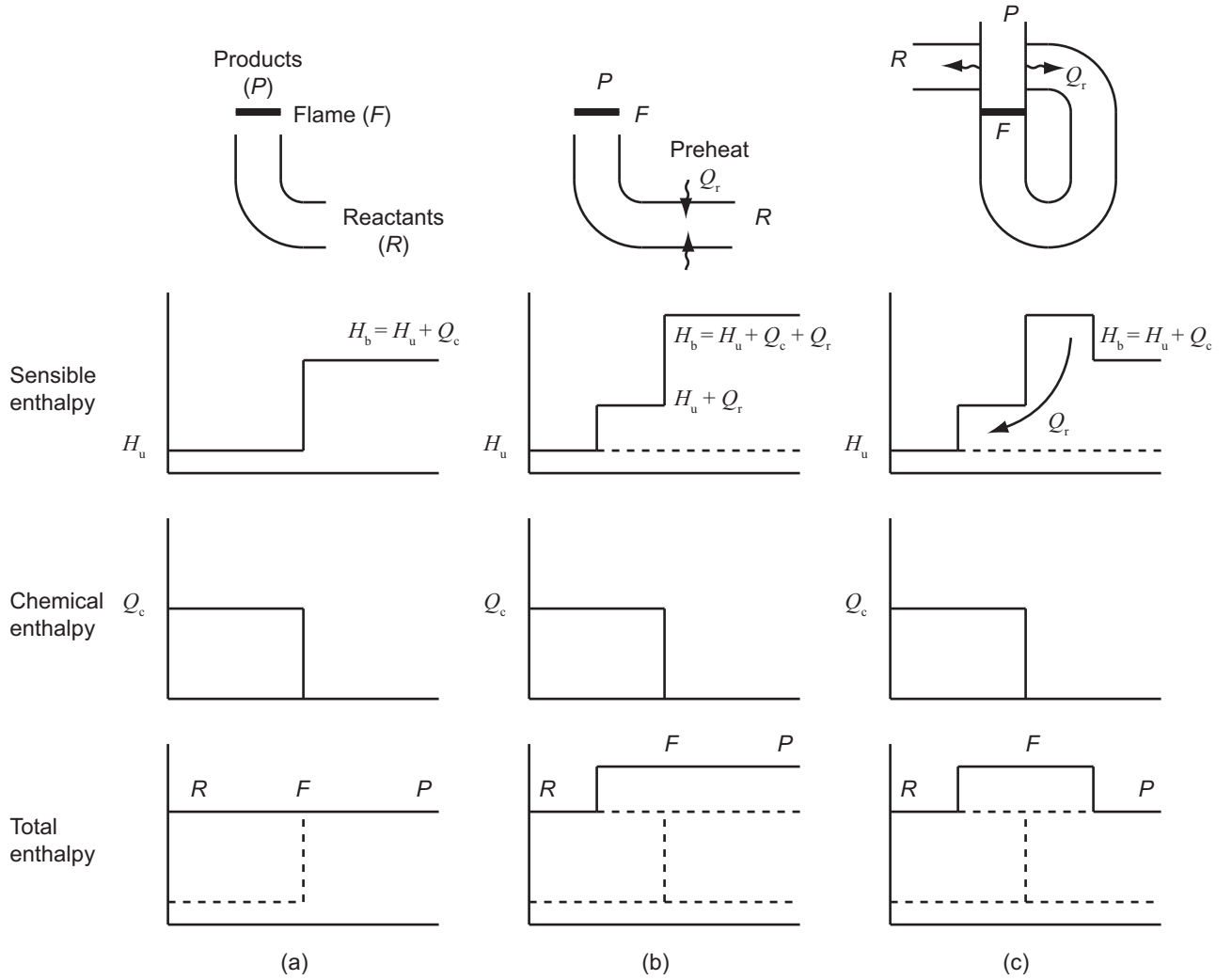


Figure 1.1 The principle of excess enthalpy burning, (a) conventional flame, (b) high temperature flame with preheating, (c) excess enthalpy flame with heat recirculation. Figure adapted from [1].

The strategy also produces burning rates that are higher than those attainable by the combustible mixture alone without the disadvantage of a high final temperature.

This idea also forms the basis for the design of heat-recirculating burners, which extend the conventional limits of flammability [13]. Interfacial heat transfer is an important process which governs this behaviour.

1.3 Non-equilibrium considerations

In Section 1.2, it is demonstrated that, with a heat exchanger and equilibrium considerations, residual sensible heat, in the products of an exothermic chemical reaction, can be utilized to increase consumption rates by energy recirculation. A more direct method, first suggested by Takeno and Sato [16], is to stabilize a flame in a solid matrix, either in small channels or a porous medium. In such a system, heat will be recirculated through the walls, of the higher thermal conductivity solid, upstream of the flame to preheat the reactants. Such a method changes the internal structure of the flame, and, for some conditions, produces excess enthalpy and higher burning rates inside the reaction zone.

A flame in a channel is a two-phase, thermo-diffusive wave process that cannot be described by equilibrium considerations, alone. The simplified equations describing the steady-state propagation of the combustion wave, in a coordinate system fixed on the flame, are

Gas energy:

$$\rho c_p (S_u - S_f) \frac{dT}{dz} = \lambda \frac{d^2 T}{dz^2} - \frac{4h_V}{D} (T - T_w) + Q_c \dot{\omega}, \quad (1.1)$$

Gas species:

$$\rho (S_u - S_f) \frac{dY}{dz} = \mathcal{D} \frac{d^2 Y}{dz^2} - \dot{\omega}, \quad (1.2)$$

Solid energy:

$$-\rho_w c_w S_f \frac{dT_w}{dz} = \lambda_w \frac{d^2 T_w}{dz^2} + \frac{4h_V}{D} (T - T_w), \quad (1.3)$$

where S_u and S_f are characteristic speeds for the inlet flow and flame propagation, respectively. The difference of these velocities, $S_b = S_u - S_f$, is the burning velocity of the flame, which is linked to the rate at which reactants are consumed. Therefore, there are two characteristic velocities: S_b for the combustion wave in the gas and S_f for the thermal wave in the solid.

For now, Equations 1.1 to 1.3 are written as an isolated system with no heat loss to the ambient environment and constant properties are assumed. The term $\frac{4h_V}{D} (T - T_w)$ is a simplified model for interfacial heat transfer between the gas and the wall, where h_V is an average volumetric heat transfer coefficient. The importance influence of interfacial heat transfer shall be shown throughout this dissertation.

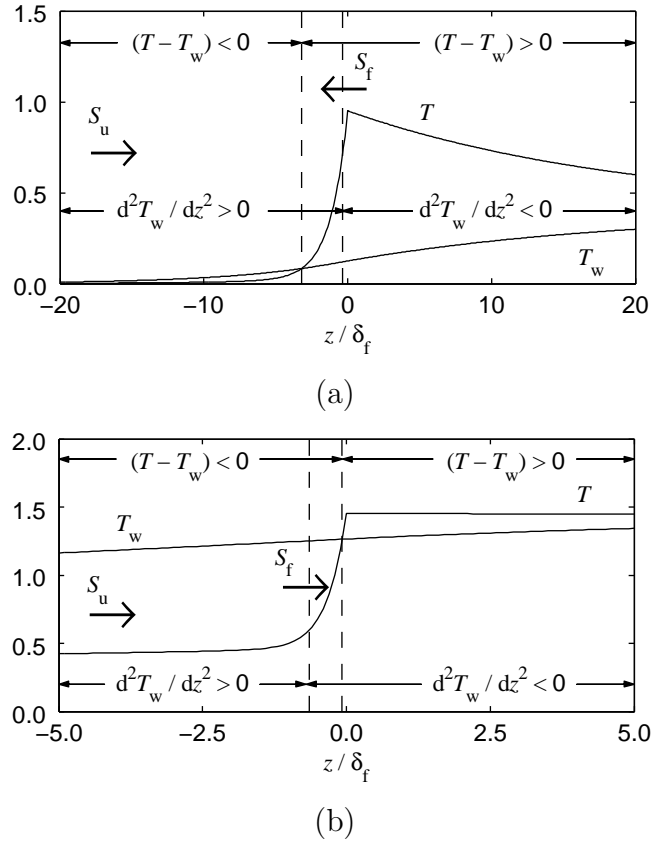


Figure 1.2 Combustion modes for propagating flames in a heat recirculating channel: (a) counter-current flame propagation, (b) concurrent flame propagation. Profiles are generated from the asymptotic model of Ju and Xu [2]. Temperatures are normalized by the inlet and adiabatic flame temperatures, $(T - T_u)/(T_{af} - T_u)$.

Theorists have had considerable success describing the physics of steady filtration waves. A review by Babkin [15] covers the body of work in this area. In these studies, equations similar to those above are solved with simplified transport and one-step kinetics to determine the approximate structure of the filtration wave. Figure 1.2 shows typical profiles obtained for the gas and solid wall generated from the Ju and Xu [52] model. Details of the solution procedure are described in Appendix A.2. The structure of the filtration wave depends on the direction of propagation. For certain conditions, flames in a solid matrix propagate concurrent or counter-current to the flow direction.

Three zones can be identified in the figure. The first is a zone where the gas temperature is lower than the solid temperature. In this region, heat is transferred from the solid to the

gas until both temperatures reach thermal equilibrium. In the second zone, heat exchange is not the dominant mechanism driving changes in temperature. Instead, the activation of chemical reactions cause a rapid rise in temperature due to a concentration of enthalpy in this zone. The gas reaches a maximum temperature, which for certain conditions, can be above the adiabatic flame temperature of the mixture, as shown in Figure 1.2(b). After reaching the maximum temperature, the gas temperature drops abruptly in the third and final zone due to intense interfacial heat exchange causing a corresponding rise in solid temperature. Filtration waves are heterogeneous processes which are controlled by a combustion wave in the gas and a thermal wave in the solid. The energy in the final zone is then recirculated by enhanced diffusion to the preheat zone which sets up a self-sustaining ignition process.

The structure of a filtration wave has features that are different from homogeneous flames. These include: temperature differences between the combustion wave in the gas and the thermal wave in the solid, excess enthalpy in the reaction zone which causes enhanced temperatures and reaction rates, and two zones with opposite signs of interfacial heat transfer. The maximum temperatures of the gas and the solid depend on values of the parameters of the system, which includes the inlet flow velocity, S_u , and the resulting velocity of the propagating flame, S_f .

The ability for the filtration wave to propagate in forward and reverse directions without a change in the direction of the inlet mass flow is a feature of this system which deserves further comment. To illustrate the phenomenon, Equation 1.3 is rewritten to isolate the wave propagation speed [53]:

$$-S_f = \frac{\frac{\lambda_w}{\rho_w c_w} \frac{d^2 T_w}{dz^2} + \frac{4h_V}{\rho_w c_w D} (T - T_w)}{\frac{dT_w}{dz}}. \quad (1.4)$$

The temperature gradient in the solid is always positive; therefore, the direction of propagation depends on the relative value of the conduction and interfacial heat transfer terms in the numerator of the equation. When the wave moves, there will be a zone in the wave, between the inflection point in the wall temperature profile and the point $T = T_w$ (see the dashed lines in Figure 1.2), where the terms in the numerator have the same sign. This generates a net energy imbalance which must be corrected by wave motion. When the numerator is positive, the solid phase heats up and the wave moves against the flow, as it will do in Figure 1.2(a); but when the numerator is negative, the solid cools and

the wave moves, in Figure 1.2(b), in the direction of the flow. A stationary flame is also possible when conduction and interfacial heat transfer is balanced at every point in the profile. Therefore, this simple theory allows for three burning modes: 1) propagation in the direction of the combustion products and concurrent to the mass flow, 2) combustion wave motion counter-current to the flow, and 3) a stationary-combustion mode with zero wave velocity. Once again, interfacial heat transfer is an important process, which, in this case, sets the burning mode.

Equilibrium temperature is determined by the properties of the solid medium, the inlet flow rate and the thermodynamic properties of the combustion wave [54]. The expression for the final burnt temperature, in an isolated system, takes the form:

$$T_b = T_u + \frac{Q_c}{c_p} \frac{(S_u - S_f)}{S_u - (1 + \sigma)S_f}, \quad (1.5)$$

where σ is a geometric term which is a function of the relative volumetric heat capacities of the phases and the porosity, φ , of the system:

$$\sigma = \frac{(1 - \varphi)}{\varphi} \frac{c_w \rho_w}{c_p \rho}. \quad (1.6)$$

The burnt temperature is, therefore, a function the of propagation velocity. When the wave is stationary, the above expression recovers the standard form for a standard adiabatic flame. However, for a finite propagation speed, the burnt temperature is not equal to the adiabatic temperature due to energy re-distribution amongst the phases. The solid, consequently, acts as a “storage battery” [53] for the storage of sensible heat. For counter-current propagation, a portion of the energy released by combustion is soaked up by the solid resulting in $T_b < T_{af}$; whereas, for concurrent propagation, a portion of the energy stored in the solid goes to gas resulting in $T_b > T_{af}$. This unusual property allows for the propagation speed to be decoupled from the laminar flame speed. Fuel consumption, instead, depends on burning velocity, $S_u - S_f$, resulting from the thermal properties of the heterogeneous system.

Having accurate predictions for this system requires that the above equations be solved with varying properties, detailed transport and chemistry, and a more realistic model for interfacial heat transfer. Furthermore, the simplified model above is for an isolated system. It would be beneficial to compare this behaviour to one where there is heat loss to the

environment. This shall be done in Chapter 6.

1.4 Interfacial heat transfer

The main difficulty in using Equations 1.1 to 1.3 is to accurately account for gas / wall interfacial heat transfer due to the development of the thermal boundary layer in the channel. Since the bulk temperature and composition are known, an expression is often cast based on Newton's law of cooling, which gives [55]:

$$\frac{4h_V}{D}(T - T_w) = \frac{\lambda \text{Nu}}{r_w^2}(T - T_w). \quad (1.7)$$

Equation 1.7, depends on knowledge of the local Nusselt number:

$$\text{Nu} = \frac{2hr_w}{\lambda}. \quad (1.8)$$

The heat transfer coefficient, h , is not known a priori for a volumetric model. Estimates must be determined by from some form of empiricism, or by formulation of an interfacial heat transfer sub-model.

Choice of an appropriate value for Nu are made easier by the assumption that the flow is thermally fully-developed. This assumption is often made for filtration waves (see [2, 15, 24, 37, 54, 56–59], among others). This condition is reached in flows when the ratio h/λ no longer depends on the axial flow co-ordinate. Furthermore, for a simple, fully-developed, laminar flow, where the diameter does not change, Nu would also be constant. This is a standard assumption in all present volumetric formulations. While the condition is eventually reached in flows when there are no chemical reactions [60], one might legitimately question if thermally-fully developed conditions could exist through a flame where there are strong thermal and species gradients. Such a question necessitates further study to understand this behaviour.

Interfacial heat transfer is the dominant phenomenon in the flame-in-channel problem. There is, therefore, a need to test the fully-developed assumption used to generate models for this process. Such a test would come from the validation of model predictions with experiments.

A popular empirical correlation for Nu, used with some success for models of flames in porous media [20, 21, 25, 56, 61–64], is that of Wakao and Kaguei [65]:

$$\text{Nu} = 2 + 1.1\text{Pr}^{1/3}\text{Re}^{0.6}. \quad (1.9)$$

This correlation also assumes a thermally fully-developed flow. The constants and exponents for Re and Pr are tuned to account for hydrodynamic effects found when a non-reacting gas flows through the tortuous channels inside a porous media. Models linked to the above correlation work extremely well for flames at very low fuel lean equivalence ratios [56]. However, it is not clear how well the interfacial heat transfer correlation performs in such a process. In a porous media, there are several other parameters which are equally unknown. These parameters are: the thermo-physical properties of the solid [63], the packing arrangement, porosity, radiation exchange parameters [61], dispersion [56], and chemical kinetics parameters [21]. These are, effectively, tuning parameters. Therefore, a porous media burner is not an adequate test bed for the validation of interfacial heat transfer models.

An alternative test of the fully developed assumption would be to perform experiments on flames in straight channels. Such a geometry does not suffer from the multitude of unknown parameters in porous media models. Furthermore, the flow is laminar and does not exhibit the chaotic trajectories found in the tortuous passages in a porous medium.

An approximation often used for the channel case is to assume a constant Nusselt number which is based on solutions to the Graetz problem [60] for non-reacting flow, for which there are analytical treatments for a straight tube with simple heat transfer [2, 46, 57]. One-dimensional models which use this formulation satisfactorily predict general trends with respect to stabilization and flame behavior; however, there is poor quantitative agreement with experiments [2, 46]. Problems with this modeling approach are also evident in the results of other researchers. Nusselt number profiles resulting from numerical flame simulations from Norton and Vlachos [41] exhibited strongly non-monotonic behavior, especially in the flame zone. These observations are confirmed in a series of articles by Veeraragavan et al. [66, 67] in which a 2-D analytical model, in the limit of the flame sheet approximation, is derived for heat transfer from flames in parallel channels. Interfacial heat transfer profiles which result from this model also show highly peaked, fluctuating Nusselt numbers.

1.5 Heterogeneous chemistry

A competing phenomenon in such a system is surface reactions. This can either enhance or inhibit combustion. In general, reactions on a surface are not much different from gas phase reactions. However, the free energies of intermediates are lower on the surface than in the gas resulting in reaction rates that are often higher, in some conditions.

The reactivity of a substance absorbed on a surface can be greatly increased in the presence of a catalyst. This has been used to support combustion in channel monoliths coated with noble metals. Of these metals, Rhodium (Rh) exhibits the best single metal catalytic performance. Platinum (Pt) is also a good catalyst for hydrogen and methane, but exhibits reduced capability when used for higher order hydrocarbons [68].

On the contrary, a bare wall can impede homogeneous reactions by removing radicals (H, OH and O) which are important for the elementary chain reactions that sustain strongly-burning flames. For surface reactions to occur, a gaseous species must be absorbed by the surface. This absorption process is the rate-limiting process in the heterogeneous kinetic reaction. Radical removal by heterogeneous reactions is widely believed to follow a Langmuir-Hinshelwood mechanism, in Table 1.5, where molecules absorbed on a surface undergo bi-molecular reactions. Like homogeneous reactions, heterogeneous reactions are kinetically controlled and are exponential with temperature. But, heterogeneous reactions at a surface cannot occur at a rate that is greater than the rate at which reactants are transported, absorbed and desorbed from the surface. This is termed the mass transfer limit.

The results of Kim et al. [3] for quenching distances with reactive and “inert” stainless

Table 1.1 Langmuir-Hinshelwood surface reaction mechanisms. * indicates a vacant surface sites, while ()* denotes an absorbed radical.

Radicals	Reaction mechanisms
H	$\text{H} + * \rightarrow \text{H}^*$ $2\text{H}^* \rightarrow \text{H}_2 + 2^*$
O	$\text{O} + * \rightarrow \text{O}^*$ $2\text{O}^* \rightarrow \text{O}_2 + 2^*$
OH	$\text{OH} + * \rightarrow \text{OH}^*$ $2\text{OH}^* \rightarrow \text{H}_2\text{O} + \text{O}^* + *$ $2\text{O}^* \rightarrow \text{O}_2 + 2^*$

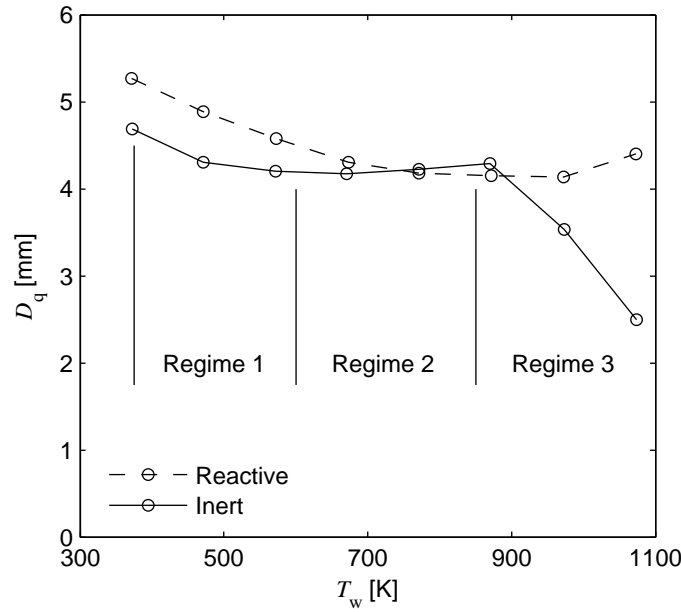


Figure 1.3 Quenching distances, D_q , of reactive and inert stainless steel plates with wall temperature, T_w . Figure adapted from [3].

steel plates are shown in Figure 1.3. The inert plates were annealed to create an oxidized passivity layer on the wall surface to impede radical absorption. Three regimes are apparent in the figure. In the first regime, quenching distance decreases with wall temperature. This is a thermal effect due to reduced heat losses, when the temperature difference between the reaction zone and the wall decreases. In the second regime, quenching distance increases with wall temperature. This reverse behaviour is caused by heterogeneous reactions at the surface, where, as wall temperatures increase, heterogeneous kinetics are enhanced, removing more radicals at the wall surface. For the reactive surface, radical quenching at the wall slows down the rate of chain branching and ultimately extinguishes the flame. But, for the inert wall there is a third regime where, once again, a steep decrease in quenching distance occurs with wall temperature. In this third regime, high wall temperatures cause enhanced rates of production of the radicals OH, H, and O in the gas phase, which compensates for the radical removal by heterogeneous reactions at the wall.

Kim et al. [3] also present data for other wall materials. Figure 1.4 shows data for quartz. Like the inert stainless plates, the influence of heterogeneous reactions are suppressed by homogeneous reactions at high wall temperatures. However, unlike stainless steel, quartz

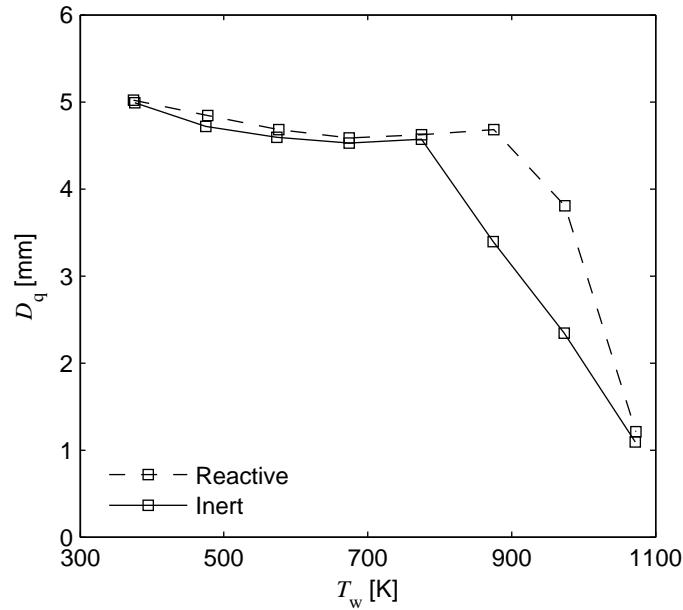


Figure 1.4 Quenching distances, D_q , of reactive and inert quartz plates with wall temperature, T_w . Figure adapted from [3].

does not show much difference between reactive and inert plates over the temperature range. Quartz, therefore, exhibits an inherently lower reactivity than metallic materials.

The focus of the present investigation is on the effects of interfacial heat transfer. It is, therefore, advantageous to isolate the phenomenon by suppressing the competing effects of heterogeneous chemical reactions. This is done in two ways. First, quartz is chosen as the wall material used in experiments. This material is found to be, comparatively, inert when used as a channel. Secondly, the channel is heated so that the wall temperature is high enough such that the rate at which radicals are removed, at the walls, is overwhelmed by the production of radicals by homogeneous reactions.

1.6 Flame curvature

Flames in channels are subjected to incoming non-uniform fully-developed parabolic flow profiles which cause an increase in the flame front cross-sectional area and higher burning rates. This presents problems for a volumetric formulation (Equations 1.1 to 1.3) where the flame structure is assumed to be one-dimensional.

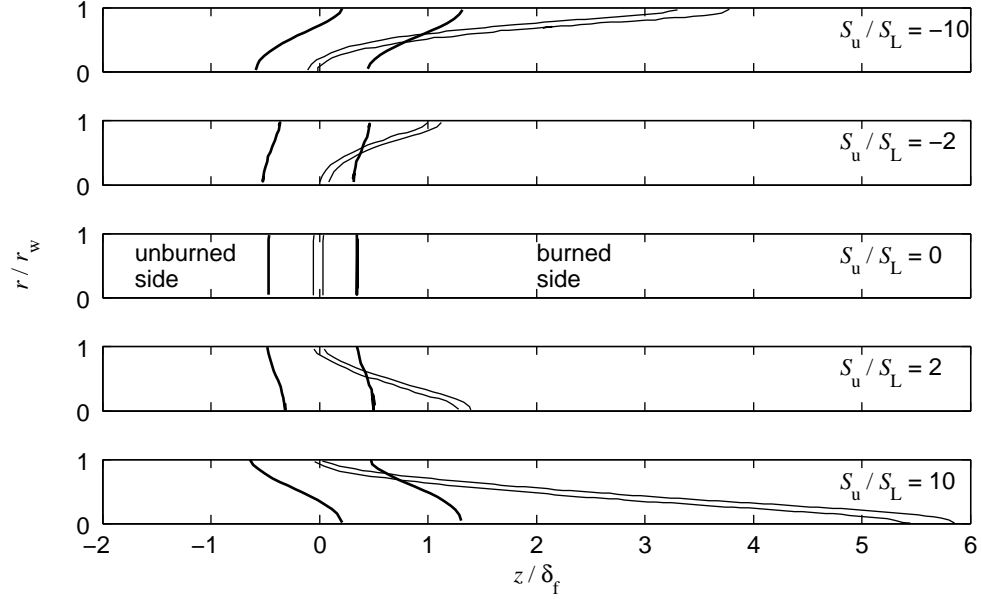


Figure 1.5 Structure of adiabatic flames for selected values of S_u/S_L . $\varepsilon = 0.1$ (thin line) and 1.0 (thick line). The flames are represented by isotherms $\theta = 0.4$ and 0.8. Here, r is a channel half-width. Figure adapted from [4].

A study to understand the effects of flame curvature was undertaken by Daou and Matalon [4]. They found that the degree to which hydrodynamics affects burning rate depends on a parameter, ε , which is the ratio of the flame thickness, which is the spatial extent of the chemical reaction, and the channel geometry:

$$\varepsilon = \frac{\delta_f}{r_w}, \quad (1.10)$$

where the channel half-width is chosen here to be the radius of a tubular channel, r_w . The flame thickness, which is the ratio of thermal diffusivity and laminar flame speed: $\delta_f = \alpha/S_L$, is $O(10^{-4})$ m for most hydrocarbon flames. A related parameter, which also captures the hydrodynamic effect, is the Peclet number:

$$\text{Pe} = \frac{U r_w}{\alpha} = \frac{U}{S_L} \frac{r_w}{\delta_f} = \frac{U}{S_L \varepsilon}. \quad (1.11)$$

The case of a small Peclet number, $U/S_L \rightarrow 0$ with $\varepsilon = O(1)$, would be expected to yield planar flames [69]. This corresponds to freely-propagating flames in large channels, like in apparatus used to measure the limits of flammability [70], or to flames in a weak flow in a

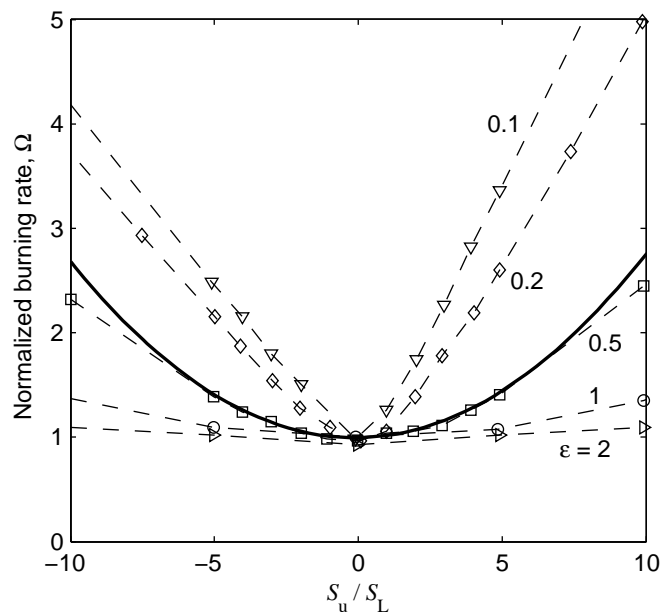


Figure 1.6 Normalized burning rate, Ω , versus inlet flow speed, S_u/S_L , for adiabatic flames with differing ε . The dashed lines are based on a two-dimensional, thermo-diffusive formulation. The solid line is based on leading terms in an asymptotic formulation for $U/S_L \rightarrow 0$ and $\varepsilon = O(1)$. Figure adapted from [4].

small channel.

Daou and Matalon [4] derived analytical expressions and conducted numerical calculations for the burning rate of adiabatic flames propagating in channels subjected to parabolic inlet flow profiles. Figure 1.5 shows the resulting structure of the adiabatic flames, characterized by two contours of constant temperature, for inlet flow velocities of differing intensity. Inlet flow rates concurrent and counter-current to the propagation direction of the flames are shown. Two flames are shown: for $\varepsilon = 0.1$ and 1.0 . The case, $\varepsilon = 0.1$ corresponds to a relatively thin flame, or a wide channel. This flame is planar for zero inlet flow velocity, but there is substantial curvature when the flow velocity is imposed. The case $\varepsilon = 1.0$ corresponds to a thin channel, or a thicker flame, where the channel dimension is of the same order as the flame thickness. As such, the distance between the isotherms is now farther apart. The apparent curvature is very much reduced due to the greater thickness of the flame.

Figure 1.6 shows a summary of the Daou and Matalon [4] calculations for the burning

rate of adiabatic flames as a function of inlet flow velocity. The burning rate, Ω , has been normalized by the burning rate of a planar, adiabatic flame. For moderate ε , burning rates are found to depend quadratically on inlet flow speed. For moderate flow speeds, the effect of the hydrodynamics is, therefore, negligible.

The phenomenon has also been studied with density variation [69] and heat loss boundary conditions [14, 71]. Flames in small channels are, again, found to be weakly stretched when subjected to moderate flow rates, with structures that are more or less flat and perpendicular to the incoming reactant stream.

This section has demonstrated that the global combustion rate of a flame in a channel subjected to a varying flow profile is a function of the flame thickness and inlet flow rate. The present study shall look at flames in small channels. This case approaches the limit where the reaction zone thickness is of the same order as the tube radius:

$$\varepsilon \rightarrow O(1). \quad (1.12)$$

It is, therefore, assumed that, in the limit of Condition 1.12, the effect of the velocity profile on flame curvature, and the resulting burning rate, is negligible and that the simpler one-dimensional (1-D) volumetric formulation, with detailed transport and chemical kinetics, is able to model the structure of these “flat” flames.

1.7 Methodology

The focus of this work is to investigate the physics which govern flame / wall heat transfer for flames in small heated channels. The dissertation shall use the approach of simplified models and experiments to isolate and understand the effects of this phenomenon.

First, stable combustion in a non-participating channel is investigated to isolate the heat transfer phenomenon to determine its role on heat loss. In Chapter 2, an alternative formulation for a volumetric model is proposed where the detailed 1-D structure of a flame in a channel is determined by coupling a 1-D flame for axial diffusion and chemistry to an axisymmetric interfacial heat transfer sub-model for flame / wall energy transfer. The interfacial heat transfer sub-model takes into account heat release from combustion reactions by tracking the consumption of chemical enthalpy, to predict heat loss from the reaction zone to the tube wall.

In Chapter 3, model predictions are analysed to understand the role of chemical energy release on heat loss, and its resulting role in flame stabilization. It is shown that the lack of quantitative agreement in present volumetric mode predictions is caused by not accounting for the effects of heat release on interfacial heat transfer, demonstrating the critical importance of heat release on the interfacial heat transfer phenomenon.

Results are then compared to experiments, in Chapter 4, to validate model predictions with experimentally-observed flame stabilization positions at variable inlet flow rates. It is shown that quantitative agreement with model predictions is possible by overcoming the problems of previous experimental apparatus with an improved apparatus and methodology, within the bounds of measurement uncertainty.

The model is also compared to detailed, multi-dimensional simulations, in Chapter 5, which predict the “true” structure of the flame. Some interesting effects due to radial non-equidiffusion on chemical reaction rates is also shown.

Finally, in Chapter 6, the focus turns to the full case of flame propagation in a participating channel, with heat recirculation. For the filtration wave, the volumetric model is re-derived to include the effect of flow redirection, due to gas expansion, which is important for this case. The importance of heat release on flame / wall heat transfer, and the resulting flame propagation, is once again demonstrated.

Chapter 2

Stationary flame in a steady wall temperature profile

The investigation starts with the simple, but fundamentally important, case of a stationary flame in a small channel. For now, the flame shall be de-coupled from heat recirculation by a constant temperature wall to focus on phenomena in the gas phase. The wall temperature is also made to increase, monotonically, with axial position, so that the combustion wave stabilizes at a unique location in the channel. This case is, therefore, similar to a burner-stabilized flame, but it is interfacial heat transfer between the gas and channel wall, and not heat loss to an inlet boundary, which principally governs flame dynamics and stabilization.

This chapter lays out the basic formulation and governing equations for this problem. These were first derived by Maruta et al. [72] for the axially varying wall temperature profile. The formulation has since proven its worth by predicting the wide range of dynamical behaviours observed in experiments for this case. These include stationary combustion regimes of conventional and weak flames [46, 48], which form depending on mass flow rate, separated by regimes of instability [47, 73, 74] at moderate flow rates. The latter regimes can also lead to splitting flames [75, 76]. Furthermore, at low mass flow rates, the “weak” flames that form are predicted to have a different structure with multiple peaks of heat release [48, 58, 77, 78].

2.1 Problem formulation

A reactive mixture is considered flowing through a domain restricted by a tubular duct of inner wall radius, r_w . The coordinate system chosen is 2-D and axisymmetric within which the gas temperature, t , and velocity, u , vary radially, r , and axially, z . After a suitable hydrodynamic entrance length, the gas flows into the domain with an initial, uniform temperature profile, $t(r, 0) = t_u$, and fully-developed parabolic velocity profile, $u(r, 0) = 2S_u \left(1 - \frac{r^2}{r_w^2}\right)$, where S_u is the average inlet flow velocity.

There is an imposed, smooth temperature profile along the wall of the tube, $T_w(z)$, which is uniform along the tube perimeter, but increases monotonically with downstream distance. This temperature profile would be controlled by external heating of some kind in an experiment (see Chapter 4.3). When the gas enters this region it is heated by interfacial heat transfer from the wall. Downstream from the entrance a stable, symmetric flame will stabilize in the tube. As the mixture approaches it, the chemistry becomes activated to feed the flame when the rate at which energy is gained by heat release and heat transfer overcomes the rate at which energy is lost to the wall.

For this class of problem, where there is radial variation of properties and composition, it is convenient to have a definition for bulk, volumetrically averaged, parameters. A discussion of how these parameters are defined is given later, in Section 2.1.1. In the limit of Equation 1.12, it is assumed that bulk parameters can be used to approximate the physics of these “flat” flames [47]. The model is further simplified by assuming that the density, ρ , specific heat capacity, c_p , and thermal conductivity, λ , do not vary significantly in the radial direction and are a function of the bulk temperature and chemical composition only. Therefore, the flow is assumed to be primarily one-dimensional, with composition, and thermodynamic and transport properties, varying only in the axial direction.

Before proceeding further, it is worthwhile to consider several important assumptions that are used to formulate the model. These are: 1) that the flame is weakly stretched and is flat such that the hydrodynamics does not affect burning rate. For now, the two-dimensional effects which lead to flame curvature shall be ignored. However the impact of this assumption will be checked with detailed, multidimensional simulations in a following chapter, 2) the flame is strongly burning and has sufficiently high bulk temperatures, and the walls are heated such that homogenous reactions produce species at a rate that is much higher than what can be removed by absorption at the wall. The formulation shall, there-

fore, neglect surface reactions and will concentrate solely on the effects of heat release from gas chemistry, 3) finally, for the case of a participating wall, heat transfer by conduction dominates in the channel. It is also assumed that the gas is optically thin and that the channel wall temperature is steady. These conditions render radiation an ineffective mode for heat transfer which is not considered.

2.1.1 Bulk parameters

The following model shall use bulk parameters in its formulation. A bulk parameter, X , follows the general form:

$$X \int \Psi \, dA = \int \Psi x \, dA. \quad (2.1)$$

X is equal to the true rate at which Ψ advects the parameter x integrated over the cross section of the tube. Bulk temperature is defined such that the total rate of thermal energy (or enthalpy) which advects into the flow volume is constant, with $\Psi = \rho c_p u$ and $c_p \neq c_p(r)$:

$$T(z) \equiv \frac{1}{\dot{m}} \int_0^{r_w} \rho u t 2\pi r \, dr, \quad (2.2)$$

where \dot{m} is the mass flow rate of the gas mixture. Equation 2.2 defines the bulk, or “mixed-cup”, temperature of the fluid at each axial location. Average velocity, U , is similarly defined, but from flow rate, with $\Psi = 1$. It is determined from mass continuity (see Equation 2.4). Composition is described by the bulk mass fractions of each species, Y_k , using $\Psi = \rho u$. The subscript k represents each of the chemical species used in the model.

The properties ρ , c_p and λ are also bulk values. They are assumed to be functions of the bulk temperature and chemical composition only:

$$\begin{aligned} \rho(r, z) &\simeq \rho(Y_k, T), \\ c_p(r, z) &\simeq c_p(Y_k, T), \\ \lambda(r, z) &\simeq \lambda(Y_k, T), \end{aligned} \quad (2.3)$$

and, thus, do not depend on the radial location.

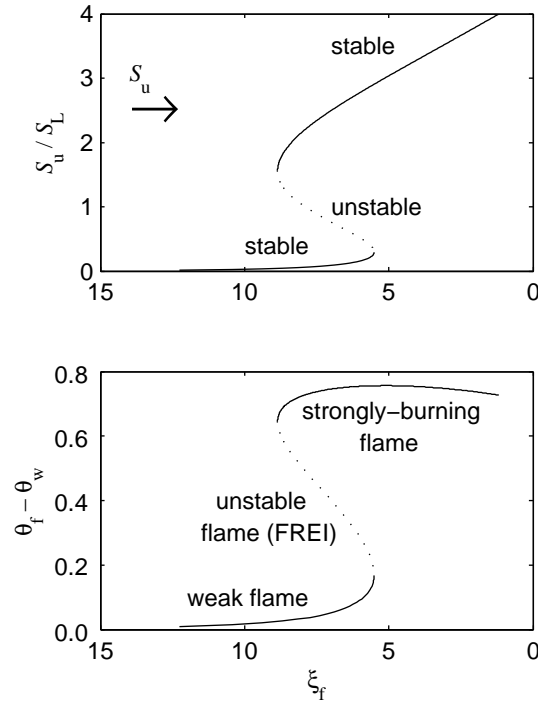


Figure 2.1 Global solution behaviour from an asymptotic model for a flame stabilized in a channel with a axial wall temperature gradient. Normalized inlet velocity, S_u/S_L , and flame / wall temperature difference, $\theta_f - \theta_w$, as a function of dimensionless stabilization position, ξ_f . $S_L = 0.18$ m/s, $T_u = 300$ K, $T_{af} = 1800$ K, $Nu = 4$, $Le = 0.9$, $\beta \rightarrow \infty$.

2.2 Solution from an asymptotic model

It is useful to begin the discussion with results from a simple analytical model. Maruta et al. [46] has derived such a model, for stabilized combustion in a small channel, which uses the asymptotic method to solve for the structure of the combustion wave and its stabilization position in the wall temperature profile. The model consists of 1-D volumetric equations for the gas phase, but assumes an infinitely thin reaction sheet, $\beta \rightarrow \infty$, constant properties, and simplified chemistry consisting of only one reactant specie. Further details relating to the formulation and solution procedure are outlined in Appendix A.1.

Figure 2.1 shows typical S-shaped curves for flame burning velocity and temperature produced by solving the simplified analytical equations. Burning velocity is equal to the inlet flow velocity for these stationary flames. For a given dimensionless flame stabilization location, ξ_f , there are several points on the branches of these curves where a flame may,

potentially, be realized. The upper branch, at high inlet mass flow rates, are associated with strong, conventional flames. Preheating from the wall leads to higher burning rates that have inlet velocities which are greater than two times the laminar flame speed. These flames also exhibit large temperature differences between the gas and the tube wall, and are strongly affected by heat loss [46]. On the intermediate branch are flames which are observed to exhibit oscillatory behaviour of periodic extinction and re-ignition in the channel [47]. This branch is an unstable mode which has been termed a repetitive extinction and re-ignition instability (FREI) due to its nature. The calculations also reveal a low-velocity mode of combustion that is characterized by low inlet mass flow rates and flame temperatures. These have been termed “weak” flames [48].

A complete characterization of stability for this system would require stability analysis. One has indeed been done for this case [72]; however, the following argument may suffice. Stable combustion in this geometry depends on a balance of the rate of heat gain and loss in the system. If it is supposed that the effects of conduction and interspecies diffusion are negligible in the preheat zone, the energy needed to preheat the reactants would have to be balanced by heat gain through the higher temperature and by chemical reactions. When the flame is perturbed by higher flow velocities, it requires more energy to heat reactants due to the increased mass flow entering the system. Reaction rate is a function of temperature only, therefore the flame cannot immediately adjust to the added mass flow by generating higher heat release due to chemical reactions. It must move to a higher temperature location in the tube where energy needed can be balanced by increased heat transfer from the tube wall and higher reaction rates at the increased local temperature. Consequently, flames which respond to positive perturbations in mass flow rate by moving to higher wall temperatures, as in the top and bottom branches in Figure 2.1, would be stable. However, flames which move to lower wall temperatures locations would not have enough energy to consume a higher mass flow. The middle FREI branch is, therefore, unstable.

2.3 Numerical model

2.3.1 1-D, volumetric flame

In Section 2.2, the asymptotic model of Maruta et al. [46] is summarized for a burner-stabilized flame in a small channel. The model uses constant properties, simplified chemistry and the flame sheet assumption to determine the global behaviour of such flames over a wide range of operating conditions. However, from such models, it is not clear what the effect of combustion chemistry would be on the system. An asymptotic model would miss many of the details in the reaction layer due to the use of the flame sheet assumption. The constant property assumption would also not hold inside the reaction zone, where there is significant variability in temperature and composition.

The above considerations motivate the use of an extended 1-D, volumetrically-averaged numerical model with a chemical mechanism containing multiple species to solve the detailed chemical structure of the flame. The equations for such a model have been used by others for this case [2, 46]; therefore, only the essential features are described here. The model for the flame reduces to calculation of the steady-state solution of a system of coupled differential equations describing the conservation of mass (Equation 2.4), energy (Equation 2.5), mass transfer of any number of k chemical species (Equation 2.6), and the equation of state assuming an ideal gas (Equation 2.7):

$$(\rho U)_z = \rho_u S_u, \quad (2.4)$$

$$\rho c_p U \frac{dT}{dz} = \frac{d}{dz} \left(\lambda \frac{dT}{dz} \right) - \sum_k c_{p,k} j_{k,z} \frac{dT}{dz} - \sum_k \dot{\omega}_k h_k W_k - Q_w(z), \quad (2.5)$$

$$\rho U \frac{dY_k}{dz} = -\frac{dj_{k,z}}{dz} + \dot{\omega}_k W_k, \quad (2.6)$$

$$\rho = \frac{p \bar{W}}{RT}, \quad (2.7)$$

where terms in these equations are calculated from bulk parameters (capital letters). The above equations are formulated to handle any number of chemical species and can, therefore, accommodate detailed kinetics mechanisms. Arrhenius-type kinetics is used to calculate

species production rates, $\dot{\omega}_k$, calculated from forward and reverse rates of production defined by parameters the mechanism [79]. These species also diffuse in the domain. The variable $j_{k,z}$ is the diffusive mass flux of the species in the axial direction, and is given by

$$j_{k,z} = \rho Y_k V_{k,z}, \quad (2.8)$$

where $V_{k,z}$ is the diffusion velocity in the axial direction [79]. All transport properties are calculated using a mixture-averaged formulation.

For a later discussion, it is useful to note the terms in Equation 2.5 which pertain to the axial distribution of heat released by combustion. These bulk terms describe the heat of reaction, conduction and interspecies diffusion:

$$Q_{\text{rxn}}(z) = \sum_k \dot{\omega}_k h_k W_k \quad (2.9)$$

$$Q_{\text{th}}(z) = Q_{\text{cond}}(z) + Q_{\text{inter}}(z) = -\frac{d}{dz} \left(\lambda \frac{dT}{dz} \right) + \sum_k c_{p,k} j_{k,z} \frac{dT}{dz}. \quad (2.10)$$

The effect of conduction and interspecies diffusion is to axially spread out sensible heat, produced by the heat of reaction term. Conduction and interspecies diffusion are, therefore, thermal terms in the sense that they depend on the local gas temperature gradient. Outside the reaction zone where there are no chemical reactions, the conduction term is not zero due to an axial wall temperature gradient.

Equations 2.4– 2.7 are similar to those that govern conventional 1-D flames, except for an additional $Q_w(z)$ term in Equation 2.5, which accounts for the interfacial heat transfer between the wall and the gas. The boundary conditions are also similar to those employed for a burner-stabilized case:

$$z = z_u : \quad U = S_u, \quad T = T_u, \quad Y_k = Y_{k,u},$$

$$z = z_b : \quad \frac{dU}{dz} = 0, \quad \frac{dT}{dz} = 0, \quad \frac{dY_k}{dz} = 0, \quad (2.11)$$

$$z_u \leq z \leq z_d : \quad T_w = T_w(z), \quad (2.12)$$

but with the addition of a steady wall temperature profile along the axial coordinate. Equations 2.4– 2.7 are a system of non-linear equations that are solved with a hybrid

steady-state and pseudo-transient algorithm which uses a dampened Newton method and time marching, provided that an appropriate model for Q_w is specified. The algorithm is established [79, 80] and is readily available in premixed laminar flame codes.

2.3.2 Interfacial heat transfer sub-model

In the 1-D volumetric formulation, it is common practice to use Newton’s law of cooling as a model for heat transfer from the flame to the channel walls (see, for example [2, 46]). This approach assumes that the magnitude of interfacial heat transfer is proportional to the gas/wall temperature difference, the bulk gas thermal conductivity and a local Nusselt number:

$$Q_w(z) = \frac{\lambda \text{Nu}}{r_w^2} (T - T_w), \quad (2.13)$$

where Q_w is specified by a Nusselt number, Nu. There are two simple analytical treatments for a thermal, channel boundary layer which describe heat transfer in non-reacting gas flowing through a tube. These solutions are often referred to as the “constant surface heat flux” and “constant surface temperature” cases and, for long residence times, asymptote to constant Nu values of 4.36 and 3.66, respectively. An often-used approximation in reactive simulations is that Nu lies between these values at $\text{Nu} \simeq 4.0$. However, there is no clear reason to treat the flow as asymptotically fully-developed in the reaction zone due to the small axial thickness, and small residence times, over which chemical enthalpy is converted to sensible heat. An alternative model is needed for the thermal boundary layer which can account for the effect of chemical reactions on the heat loss to the wall inside the reaction zone.

The thermal energy equation in axisymmetric coordinates reduces to a balance between convection, radial diffusion and heat released by chemical reactions using standard boundary layer assumptions:

$$\rho c_p u \frac{\partial t}{\partial z} + \rho c_p v \frac{\partial t}{\partial r} = \frac{1}{r} \frac{\partial}{\partial r} \left(r \lambda \frac{\partial t}{\partial r} \right) - \sum_k c_{p,k} j_{k,r} \frac{\partial t}{\partial r} - q_s(r, z). \quad (2.14)$$

q_s is a source term which captures the effects of non-linear heat release by chemical reactions. From the assumptions in Section 2.3.1, terms that depend on radial non-uniformity of

properties and composition are removed. An additional simplification which shall be used, in the limit of Equation 1.12, is that the radial velocity, v , is small compared to the axial flow. In the solution, the velocity profile $u(r, z)$ is, therefore, imposed to be parabolic with the peak velocity specified to satisfy continuity (Equation 2.4) at the local axial gas density. Three terms are retained which describe the balance of axial convection and radial diffusion of energy, and the source term for heat generation by chemical reactions:

$$\rho c_p u \frac{\partial t}{\partial z} = \frac{\lambda}{r} \frac{\partial}{\partial r} \left(r \frac{\partial t}{\partial r} \right) - q_s, \quad (2.15)$$

where the boundary conditions are

$$t(r, 0) = T_u, \quad (2.16)$$

$$\left. \frac{\partial t}{\partial r} \right|_0 = 0, \quad (2.17)$$

$$t(r_w, z) = T_w(z). \quad (2.18)$$

q_s is supplied by the flame model where its magnitude is the sum of the heat of reaction, conduction and the interspecies diffusion terms:

$$q_s(r, z) = Q_{th}(z) + f(r, z)Q_{rxn}(z). \quad (2.19)$$

Defining the source term in this way ensures that energy is balanced between the flame model and the interfacial heat transfer sub-model by maintaining equivalent axial energy equations. The variable f , which will be discussed shortly, is a convolution to give $Q_{rxn}(z)$ radial dependence. The thermal component in the source term, however, does not have a convolution function. Thus, energy due to axial conduction and interspecies diffusion is assumed to be distributed uniformly across the channel at the axial bulk temperature.

Equation 2.15 is parabolic and can be solved quite rapidly with knowledge of the axial species, and the Q_{rxn} and Q_{th} profiles from the 1-D flame. The parabolic boundary layer equations, like those for the elliptic 1-D, volumetric model, are solved by first approximating these equations with finite differences. An example of this procedure is provided here for the thermal boundary layer equation. For a mesh that uses an arbitrary number of axial, n , and radial, j , nodes, the conservative difference equation is

$$(\rho c_p)^{n+1} u_j^{n+1} \frac{t_j^n - t_j^{n+1}}{\Delta z^{n+1}} = \frac{2}{r_j(\Delta r_{j+1} + \Delta r_j)} \left[(\lambda^{n+1} r_{j+1/2}) \frac{t_{j+1}^{n+1} - t_j^{n+1}}{\Delta r_{j+1}} - (\lambda^{n+1} r_{j-1/2}) \frac{t_j^{n+1} - t_{j-1}^{n+1}}{\Delta r_j} \right] + f(r_j, z_j) Q_s^{n+1}, \quad (2.20)$$

where $\Delta z^{n+1} = z^{n+1} - z^n$ and $\Delta r_j = r_j - r_{j-1}$. In the above equation, the convective term uses an up-winding scheme, while the diffusion term uses central differences. Isolating for the temperature of each node, t_j^{n+1} , yields

$$\begin{aligned} & t_j^{n+1} \left[1 + \frac{\kappa_j^{n+1}}{r_j(\Delta r_{j+1} + \Delta r_j)} \left(\frac{r_{j+1/2}}{\Delta r_{j+1}} + \frac{r_{j-1/2}}{\Delta r_j} \right) \right] \\ &= t_{j+1}^{n+1} \left[\frac{r_{j+1/2} \kappa_j^{n+1}}{r_j(\Delta r_{j+1} + \Delta r_j) \Delta r_{j+1}} \right] + t_{j-1}^{n+1} \left[\frac{r_{j-1/2} \kappa_j^{n+1}}{r_j(\Delta r_{j+1} + \Delta r_j) \Delta r_j} \right] \\ & \quad + t_j^n + \frac{\kappa_j^{n+1}}{2\lambda^{n+1}} f(r_j, z_j) Q_s^{n+1}, \end{aligned} \quad (2.21)$$

where

$$\kappa_j^{n+1} = \frac{2\Delta z^{n+1} \lambda^{n+1}}{(\rho c_p)^{n+1} u_j^{n+1}}, \quad (2.22)$$

Solving for temperature yields a tridiagonal system of equations where t , f , ρ , c_p , λ and U are initially unknown. But, the system is solved quite efficiently by first guessing the temperature and convection profiles, calculating properties based on the temperature and composition, and then by iteratively resolving the system with the Thomas Algorithm until convergence is attained.

The radial temperature profiles, $t(r, z)$, obtained in the solution are then used to generate a profile for the interfacial heat transfer term, $Q_w(z)$. The heat flux between the wall and the fluid is given by:

$$Q_w(z) = -\frac{2\lambda}{r_w} \frac{\partial t}{\partial r} \Big|_w, \quad (2.23)$$

which is proportional to the gas temperature gradient at the wall. Results from this nu-

merical calculation are preferred as it gives Q_w directly from the interfacial heat transfer sub-model temperature profiles. It is possible, however, to use the energy balance to reformat this solution into a local Nusselt number:

$$\text{Nu}_z = -\frac{2r_w}{(T - T_w)} \frac{\partial t}{\partial r} \Big|_w. \quad (2.24)$$

$Q_w(z)$ from the interfacial heat transfer solution is used in the volumetric model to close the loop resulting in a 1-D, volumetric solution for a flame stabilized in the wall temperature profile.

2.3.3 Source convolution profile

The radial dependence of the heat release is specified by a convolution, $f(r, z)$. This profile could be assumed to be uniform, $f(r, z) = 1.0$, but such a specification would ignore the fact that energy stored in the reactants is advected, non-uniformly, into the reaction zone by the laminar flow profile. Here, an alternative model is derived for f which conserves the total chemical enthalpy of the reactants and links the distribution of chemical enthalpy to heat release in the combustible mixture.

First, a way is needed to track chemical enthalpy. In the volumetric flame model, this is done by tracking individual species, but in the interfacial heat transfer model, these species are not treated explicitly. Instead, a progress variable, $\zeta(r, z)$, is introduced that acts as an indicator of the local fraction of the available chemical energy in these species:

$$\zeta = \frac{\Delta h_f^o - \Delta h_{f,d}^o}{\Delta h_{f,u}^o - \Delta h_{f,d}^o}, \quad (2.25)$$

where Δh_f^o is the local enthalpy of formation of the mixture, and ζ lies between 1 and 0 at the upstream and downstream locations, respectively. If ζ were in the volumetric model, its bulk value, Z , would be expected to behave similar to a chemical species:

$$\rho U \frac{dZ}{dz} = \frac{d}{dz} \rho \mathcal{D}_\zeta \frac{dZ}{dz} + \dot{Z}_{\text{rxn}} = \dot{Z}_{\text{inter}} + \dot{Z}_{\text{rxn}}. \quad (2.26)$$

where Z flows by convection, and can also be consumed by chemical reactions, \dot{Z}_{rxn} . Therefore, Equation 2.26 describes a thermal-diffusive process where chemical energy enters a reaction zone by advection and diffusion, and is then converted into sensible heat, due to

chemical reactions.

To illustrate these processes, Figure 2.2 shows normalized temperature and reactant species profiles of a lean methane / air, adiabatic flame, and the resulting profile for the progress variable for chemical enthalpy. The reaction zone of the flame is marked by heat release, Q_{rxn} . On the unburned side, upstream of the flame, energy is stored in methane and oxygen as chemical energy, but this energy is ultimately converted into heat in the reaction zone, raising the temperature of the flame in the downstream region. Upstream of the flame, Z closely follows the reactant species profiles and the drops in concentration due to reactant diffusivity, which is a phenomenon captured by \dot{Z}_{inter} . Z is, therefore, assumed to behave similar to the concentrations of these reactant species. However, inside the reaction zone and in the downstream region, diffusion is not the dominant phenomenon dictating the value of Z , where Z continues to drop due to consumption of chemical enthalpy by chemical reactions, \dot{Z}_{rxn} . Furthermore, it should be noted that, for this adiabatic flame, the Z and T profiles are almost mirror images of one another due to adiabatic boundary conditions, almost equal axial diffusivities, and direct conversion of chemical energy into heat. But in non-adiabatic flames, thermal energy would be lost to the wall during conversion, resulting in different shapes for the Z and T profiles.

In the interfacial heat transfer model, the profile $\zeta(r, z)$ is determined by solving a partial differential equation coupled to Equation 2.15, again, with standard boundary layer assumptions. The progress variable is assumed to advect and diffuse similar to a chemical species, therefore

$$u \frac{\partial \zeta}{\partial z} = \frac{\lambda}{\rho c_p} \frac{\text{Le}}{r} \frac{\partial}{\partial r} \left(r \frac{\partial \zeta}{\partial r} \right) - \dot{\zeta}_s, \quad (2.27)$$

where the boundary conditions express the fact that the walls are impermeable to mass transfer:

$$\zeta(r, 0) = 1.0, \quad (2.28)$$

$$\left. \frac{\partial \zeta}{\partial r} \right|_0 = \left. \frac{\partial \zeta}{\partial r} \right|_w = 0. \quad (2.29)$$

The rate at which ζ is allowed to diffuse in the radial direction is controlled by an effective Lewis number for chemical enthalpy, Le , which is defined here as the ratio of the diffusivity of ζ to thermal diffusivity. The value of this effective Lewis number is $\text{Le} = 1.09$ for a

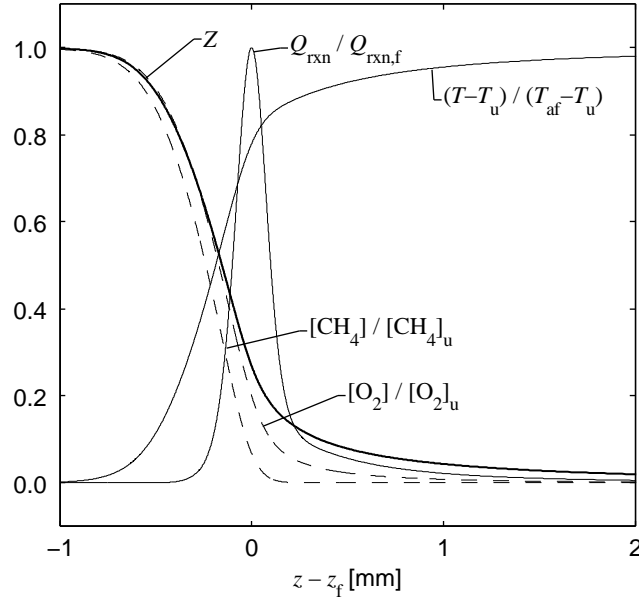


Figure 2.2 Structure of a 1-D, lean, adiabatic methane / air flame, $\phi = 0.7$. Profiles for temperature, T , heat release, Q_{rxn} , CH_4 and O_2 species, and a progress variable for bulk chemical enthalpy, Z .

stoichiometric methane / air mixture, based on diffusion length-scales.

In Equation 2.27, there is a source term, $\dot{\zeta}_s$, which describes the consumption of chemical enthalpy due to inter-species diffusion and chemical reactions:

$$\dot{\zeta}_s(r, z) = \dot{Z}_{\text{inter}}(z) + f(r, z)\dot{Z}_{\text{rxn}}(z) \quad (2.30)$$

where the convolution, f , is, again, applied to consumption by reaction. In this source term, \dot{Z}_{rxn} is defined such that there is equivalence between its rate of consumption and the rate at which energy is injected into the boundary layer due to heat release:

$$\rho\dot{\zeta}_{\text{rxn}}(r, z) = \rho f\dot{Z}_{\text{rxn}} \equiv \frac{fQ_{\text{rxn}}}{\left(\frac{\Delta E}{m}\right)_{\zeta}}, \quad (2.31)$$

where $\left(\frac{\Delta E}{m}\right)_{\zeta}$ describes the energy released per unit of ζ and is given by an energy balance over the entire domain:

$$\dot{m} \left[\left(\frac{\Delta E}{m} \right)_{\zeta} - 0 \right] = \int_{z_u}^{z_b} \int_0^{r_w} fQ_{\text{rxn}} 2\pi r \, dr \, dz. \quad (2.32)$$

In Equation 2.30, \dot{Z}_{inter} is a term for the “consumption” of chemical enthalpy by interspecies diffusion, which is recovered from the volumetric flame with Equations 2.25 and 2.26.

It is assumed that the availability of the reactant species that ζ models limits the rate of chemical reactions in a similar way to the concentration of the deficient species, following the law of Mass Action. The radial convolution, f , for the heat of reaction is, thus, made proportional to the local value of ζ in the numerator:

$$f(r, z) = \frac{\zeta(r, z)/Z(z)}{2 \int_0^{r_w} \frac{r}{r_w} \frac{\zeta}{Z} d\left(\frac{r}{r_w}\right)}. \quad (2.33)$$

The shape of ζ is retained in the definition of f , but the values are normalized to ensure conservation of the bulk heat release in the axial direction, or $\int f dA/A = 1$. This integrand is area averaged in order to account for the total energy in the tube cross-section. The profile for heat release, fQ_{rxn} , that results from this convolution depends on the local availability of the reactants through $f(r, z)$ and on reaction rate at the bulk temperature through $Q_{\text{rxn}}(z)$. These are the leading effects; however, this formulation neglects radial variability in the reaction rate caused by the local gas temperature which could also have an effect on this profile.

There are limiting cases for the convolution that depend on the Lewis number. The first is for $\text{Le} = 0$. At this limit, the rate of diffusion of ζ is much less than that of heat and ζ is not able to diffuse radially to fill in areas consumed by the flame. Here the radial dependence of heat release is controlled by the parabolic velocity profile that advects a larger amount of reactants near the centerline than at the walls. Conversely, the other limit is for $\text{Le} \rightarrow \infty$, where the diffusion of ζ is at a much faster rate than that of heat. Diffusion is, therefore, able to rapidly fill-in zones deficient in ζ . In this limit, the radial dependence of the heat release term vanishes, yielding $f(r, z) \rightarrow 1.0$.

During the solution procedure, care is taken to ensure that the mesh spacing in both models is adequate to resolve changes in temperature, species and velocity due to wall/gas heat transfer and chemical reactions. To do this, both models use an adaptive re-gridding procedure to adjust for flame movement in the axial direction. A fixed, non-uniform radial grid is also used in the interfacial heat transfer sub-model calculations. More information on the numerical procedure can be found in 2.4.

2.4 Assembly of the model

Information from the flame and the interfacial heat transfer sub-model are coupled in order to obtain the solution for the 1-D profile. To start the calculation, an initial guess for Q_s is supplied by specifying the species profiles. This profile is used in the interfacial heat transfer sub-model to calculate an interfacial heat transfer profile. The interfacial heat transfer profile is then passed to the flame model so that an updated solution can be calculated for the flame. For the next iteration, the process repeats itself first with an updated heat source profile being once again passed to the interfacial heat transfer sub-model. The calculation continues iteratively until convergence in the flame profile is obtained. This leads to a converged solution, but care is needed in specifying solution tolerances since the accuracy of the final converged flame profile depends on the combined error of each solution built up over the iterations.

The interfacial heat transfer calculation requires a heat source profile. From a numerical point of view this can create problems if the profile is not smooth and physically realistic. This is especially of concern at the beginning of the computation where there is typically not enough information to have a sufficiently accurate initial guess for all of the species profiles. The solution to this is to have a procedure to smooth out and iteratively improve the guess for the heat source profile. This is accomplished by initially bypassing the interfacial heat transfer calculation by substituting the interfacial heat transfer term completely with one that uses Newton's law of cooling and a constant Nusselt number, as done in most 1-D modeling approaches. With a better guess for the species profiles the interfacial heat transfer solution is then marched using the continuation approach to one that uses the boundary layer. During this procedure the interfacial heat transfer profile at any marching step i becomes

$$Q_w|^i = (1 - \eta)Q_w|_{\text{Nu}}^i + \eta Q_w|_{\text{BL}}^i, \quad (2.34)$$

where the subscripts Nu and BL refer to interfacial heat transfer from a constant Nusselt number approach and the boundary layer calculation, respectively. The parameter η is a marching variable that varies from 0 to 1 as the problem is solved. This provides a mechanism by which the influence of the boundary layer on the solution can be switched on slowly to improve the numerical stability of the calculation.

There are additional considerations to solve this problem. During the solution proce-

ture, the bulk temperature profiles which result from the flame and interfacial heat transfer sub-model are not necessarily the same, even though they share the same heat source profile. This is because the 1-D model is using a hybrid Q_w profile from Equation 2.34 while the interfacial heat transfer sub-model gives $Q_w|_{BL}$ due to the heat release profile. The result is that the interfacial heat transfer sub-model will locally under- and/or over-predict flame / wall heat exchange from one iteration to another. The error in interfacial heat transfer is assumed to be small. Therefore, a correction term, $Q'_w|^i$, is added to Equation 2.5 correct Q_w for the difference between the 1-D flame and interfacial heat transfer sub-model bulk temperature profiles:

$$Q'_w|^i = \sigma_{Q_w}(T_{1D} - T_{BL}), \quad (2.35)$$

where σ_{Q_w} is a factor for the sensitivity of the interfacial heat transfer sub-model to small perturbations in the bulk temperature $[W/m^2/K]$. This sensitivity factor is determined by perturbing the interfacial heat transfer sub-model temperature profiles, $t(z, r)$, either directly, with a fixed percentage of local temperature, or by constructing a convolution such that the perturbed temperature profile is self-similar. Equation 2.35 is an exact expression for small differences in bulk temperature, however, it was found that numerical stability could be greatly improved, for some cases, if an alternative definition for $Q'_w|^i$ is used. Q'_w is, alternatively, defined as

$$Q'_w|^i \approx Q_w|_{BL,c}^i \frac{\lambda(T - T_w)|_{1D}^i}{\lambda(T - T_w)|_{BL,c}^i} - Q_w|_{BL,c}^i \frac{\lambda(T - T_w)|_{BL,h}^i}{\lambda(T - T_w)|_{BL,c}^i}, \quad (2.36)$$

where the subscripts c (cold) and h (hot) denote interfacial heat transfer parameters calculated with and without the heat release source term, respectively. Regardless of the method, Q'_w tends to zero as the bulk temperature profiles converge.

2.5 Solution profiles

Figure 2.3 shows the bulk flame structure for a solution which uses an interfacial heat transfer model with chemical energy release. Three characteristic zones are apparent in the figure. In the unburned zone, upstream of the flame, the maximum gas/wall temperature difference is small due to the long wall temperature profile. This is attached to a preheat

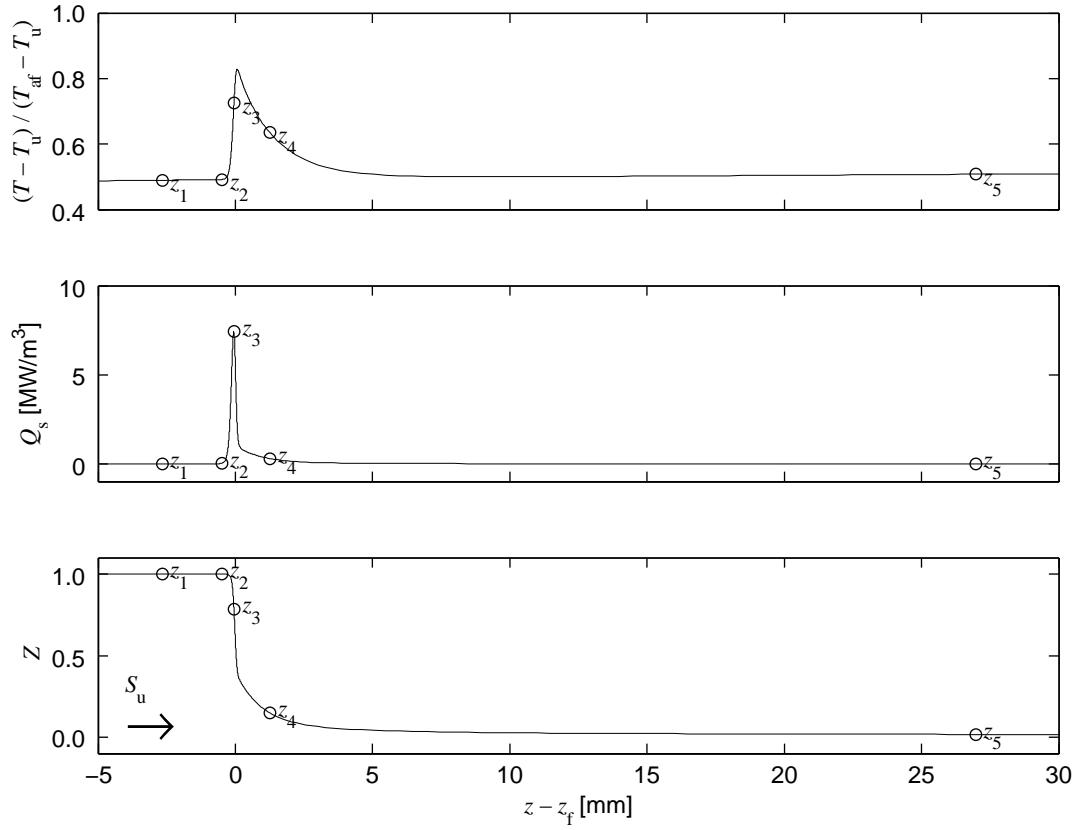


Figure 2.3 Normalized bulk gas temperature, T , heat source, Q_s , and Z profiles. $\phi = 1.0$, $S_u = 0.85$ m/s, $T_u = 300$ K, $T_{af} = 2223$ K, $Le = 1.0$.

region just upstream of $z - z_f = 0$ which has a very thin thickness driven by the competition between upstream conduction and convection pushing the flame downstream. Following the unburned zone is the reaction zone where the gas rapidly reaches a peak temperature due to heat release. This zone coincides with the peak in Q_s and a sudden drop in ζ as reactants are consumed and sensible heat is released. This sharp temperature peak is indicative of conventional flame behaviour [46]. There is also substantial heat lost to the wall inside this zone, as evidenced by the fact that the predicted flame temperature is 464 K below the adiabatic flame temperature, T_{af} , of the stoichiometric mixture. This temperature is lower than those predicted by the asymptotic model in Section 2.2 which, due to the flame sheet assumption, does not adequately resolve heat transfer in the reaction zone and, thus, predicts super-adiabatic flame temperatures. Nevertheless, after reaching a maximum temperature value, the gas temperature abruptly drops as additional enthalpy

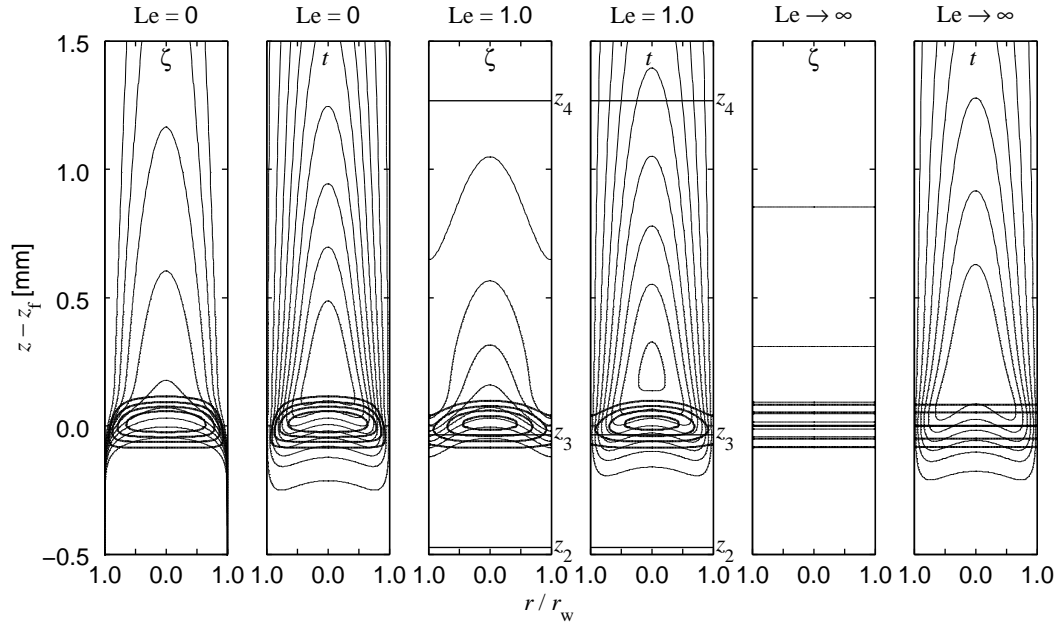


Figure 2.4 Effect of Lewis number, Le , on ζ (left) and normalized gas temperature, $(t - T_u)/(T_{af} - T_u)$ (right) profiles from interfacial heat transfer sub-models with chemical energy release. Heat release contours, Q_{rxn} , are also superimposed as thick lines. Temperature contours are $0.5T_{af} \leq t \leq 0.85T_{af}$ in intervals of $0.05T_{af}$. ζ contours are $0.9 \geq \zeta \geq 0.3$, decreasing in intervals of 0.1. Heat release contours are $fQ_{rxn}/Q_{rxn,peak} = 0.5, 0.75, 1.0$ and 1.25. $\phi = 1.0$, $S_u = 0.85$ m/s, $T_u = 300$ K, $T_{af} = 2223$ K, $Le = 1.0$.

is lost due to intense interfacial heat exchange with the cooler wall. Once the gas cools, the products are again heated by the increasing wall temperature downstream of the flame.

Figure 2.4 shows the 2-D structure from the interfacial heat transfer sub-model as a series of temperature, t , and ζ contours. Contours for the heat of reaction are superimposed on both plots. For the $Le = 1.0$ case, the contours of ζ and Q_{rxn} indicate that most of the chemical activity in the flame is in a small region centered around the reaction zone. This area governs flame behaviour and position. The figure also shows the gas temperature and heat release profile in the vicinity of this region. As heat is released, ζ is initially consumed at higher relative rates near the walls because ζ is advected into the reaction zone at a higher rate near the centerline due to the velocity profile and the no-slip condition at the wall. A rise in the gas temperature is coincident with the consumption of reactants due to heat release. When the source term dissipates, the gas temperature continues to rise near

the centerline due to slower ζ consumption in the CO oxidation region of the flame while the gas temperature rapidly cools at the walls due to intense interfacial heat exchange.

These profiles change with Lewis number. For the lower $Le = 0$ limit, ζ does not diffuse in the radial direction, thus ζ consumed at the walls cannot be replenished. Heat release concentrates at the centerline where the flux of ζ is the highest producing shallower temperature gradients at the wall. $Le = 0$, therefore, represents the lowest heat loss possible within the reaction zone for this model. Conversely, when $Le \rightarrow \infty$, ζ is much more diffusive than heat. Its consumption at the wall is rapidly replenished by ζ from the centerline. The resulting ζ profile is radially uniform owing to high diffusivity that would smooth out any gradients, thus producing uniform heat release across the channel. The $Le \rightarrow \infty$ solution has the maximum amount of energy released near the wall, resulting in the highest possible heat loss for this model.

Chapter 3

The effect of chemical energy release

In Chapter 2, a numerical formulation is derived for a flame stabilized in a small channel. Unlike other volumetric formulations, the model does not rely on Newton's Law of Cooling to generate an interfacial heat transfer profile. Instead, a developing thermal boundary layer is used which responds to heat release due to chemical reactions and heat exchange between the flow and the wall. This chapter discusses the implications of relaxing this assumption in the model.

The problems with previous modeling approaches are evident in the results of other researchers. Local Nusselt number profiles from the numerical flame simulations of Norton and Vlachos [41] exhibit strongly non-monotonic behavior, especially in the flame zone. This observation is confirmed in a series of articles by Veeraragavan et al. [66, 67], in which a 2-D analytical model, in the limit of the infinitely thin, flame-sheet approximation, is derived for heat transfer from flames in parallel channels.

This chapter shows that these observations result from the unique effects of strong nonlinear heat release, and its influence on heat loss from flames in small channels. The discussion shall begin by looking at what would occur if this effect were neglected by calculation of interfacial heat transfer without the effects of chemistry. This approach is similar to standard volumetric models. Heat release will, then, be added to demonstrate the effect that this important phenomenon has on dictating the structure of flames in confined channels.

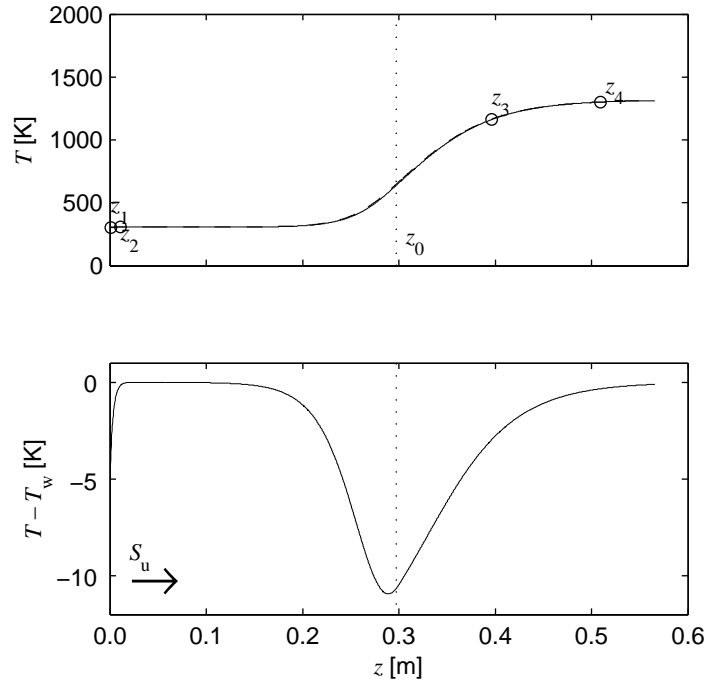


Figure 3.1 Simulated gas (—) and wall temperature profiles (—) for a non-reacting flow (air). The gas/wall temperature difference, $T - T_w$, is plotted below for reference. $\phi = 0.0$, $S_u = 1.00$ m/s, $T_u = 300$ K.

3.1 Solution with frozen chemistry

The simplest interfacial heat transfer solution that occurs for this problem is for a boundary layer without chemical reactions. For this case, the gas temperature responds only to heat transfer at the wall/gas interface. Figure 3.1 shows bulk gas and wall temperature profiles for air flowing through the tube. These profiles are almost indistinguishable, therefore the gas/wall temperature difference is also plotted for reference. At the inlet, the gas temperature is slightly below the wall temperature, but it quickly equilibrates in the flat entrance region of the tube. The gas and wall temperatures then deviate as T lags behind T_w at the steepest gradient in the wall temperature profile. The temperature differences are no greater than 11 K throughout this zone. Finally, the gas and wall temperatures once again equilibrate as the gas flows out of the tube.

Radial temperature profiles normalized by the bulk temperature at the axial positions z_1 – z_4 , specified in Figure 3.1, are shown in Figure 3.2. All profiles have wall temperatures that are higher than the bulk temperature, $t(z, r_w) > 1.0$. At the inlet, there is initially

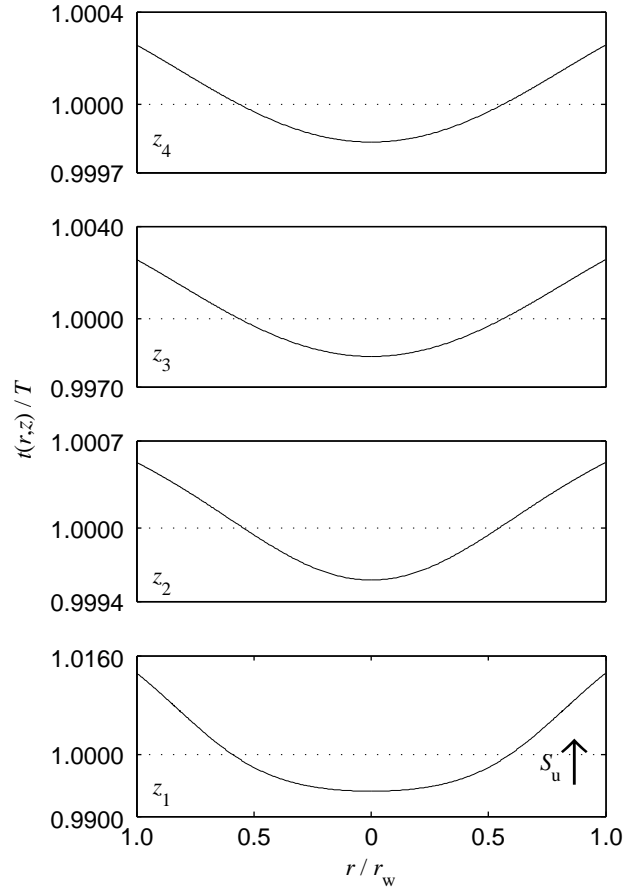


Figure 3.2 Radial gas temperature, $t(r, z)$, profiles for a non-reacting flow (air). These profiles are normalized by the bulk gas temperature, $T(z)$. $z_1 = 0.001$ m, $z_2 = 0.011$ m, $z_3 = 0.396$ m, $z_4 = 0.509$ m. $\phi = 0$, $S_u = 1.00$ m/s, $T_u = 300$ K.

a small, 6 K, difference between the uniform gas and wall temperatures. When the flow reaches z_1 , there has not yet been time for this thermal energy to diffuse to the center of the channel, but the boundary layer adjusts to the initial temperature difference at z_2 where the profile appears more thermally-developed. A longer distance is needed to achieve self-similar profiles as the gas propagates down the tube. As the wall temperature slowly rises, similar profiles are eventually obtained in the downstream region of the tube in the region of z_3 and z_4 where the normalized temperature profiles show no perceivable difference.

For an inert stream flowing through the tube, the wall temperature will always be higher than the bulk gas temperature. There is one direction for heat transfer, therefore

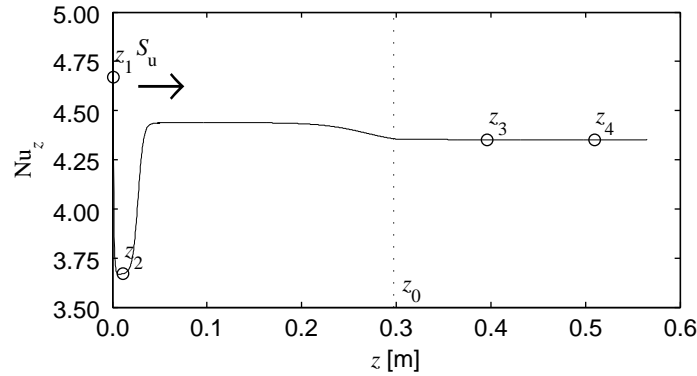


Figure 3.3 Simulated Nusselt number profile, Nu_z , for a non-reacting flow (air). The Nusselt number settles to a, more or less, constant value of $Nu_z = 4.34$ downstream of z_0 . $\phi = 0$, $S_u = 1.00$ m/s, $T_u = 300$ K.

the Nusselt number will always be positive for this case. Nu also strongly depends on the magnitude of the wall temperature gradient. Because of this dependence, the Nusselt number is not constant, but a local Nusselt number profile, Nu_z , can be ascertained using Equation 2.13. Figure 3.3 shows the local Nusselt number profile for the non-reactive case. At the inlet, the small step change in wall temperature produces large wall temperature gradients. Nu_z is highest here, but then tends towards $Nu_z = 3.66$ in the constant temperature inlet region of the tube, as expected. The value again varies as the wall temperature increases. The Nusselt number tends to a value of approximately 4.5 in the region of the initial temperature rise, but then settles to a value of 4.34 after passing z_0 . This value is more or less constant and is close to the value of $Nu \approx 4.0$ often used in tubular flame studies to model the constant-wall-temperature case.

The focus of this chapter is to understand the effect of chemical energy release on flame / wall energy transfer. Therefore, comparisons will be made to simulated 1-D flame profiles which result from use of an interfacial heat transfer sub-model with and without the effects of heat release from chemical reactions. In Equations 2.15 and 2.27, the effects of chemical energy release are accounted for by the heat release profile, fQ_{rxn} , composition, Y_k , and the progress variable, ζ . An interfacial heat transfer solution without the effects of chemical energy release would result when there are no chemical reactions. This solution is produced from the boundary layer equations by fixing the composition in the whole domain to what is found at the inlet and by removing the heat release term, which leads to the following

substitutions:

$$Y_k(z) \equiv Y_k(0), \quad (3.1)$$

$$q_s(r, z) \equiv 0, \quad (3.2)$$

$$\zeta(r, z) \equiv 1. \quad (3.3)$$

A Q_w profile generated from the boundary layer equations without chemical energy release will be termed an interfacial heat transfer solution with frozen chemistry; in that the solution is generated by freezing chemical reactions. These solutions have similar trends in temperature and Nusselt number presented in Figures 3.2 and 3.3 for the non-reactive, air case. These Nu_z profiles are then fed into Equation 2.13 to compute Q_w profiles for the 1-D flames. It is interesting to note that, for this wall temperature profile, the Nu_z profile obtained with frozen chemistry have values that are close to the assumption of $Nu \approx 4.0$ used in standard volumetric models. Therefore, this commonly used approximation essentially corresponds to interfacial heat transfer for non-reactive flow and neglects the effects of chemical energy release in the vicinity of the flame.

3.2 Solution with combustion

The characteristics of the solution change considerably when the non-linear effects of heat release are included in the interfacial heat transfer sub-model. Figure 3.4 shows computed bulk temperature profiles for two stoichiometric flames with the same inlet flow velocity and temperature. The approximate positions of the flames can be noted by the peaks in bulk gas temperature. The upstream flame uses a sub-model with frozen chemistry while the downstream flame uses an interfacial heat transfer sub-model with heat release. There is a clear difference in the peak temperature and position of these flames despite the fact that the only difference between the models lies in the formulation of the interfacial heat transfer sub-model.

Radial temperature profiles at the axial locations z_1 – z_5 , marked with open circles in Figure 2.3 and horizontal lines in Figure 2.4, are plotted in Figure 3.5. Upstream of the flame at location z_1 , the gas is heated solely by the wall. At this location, the energy transfer from the wall to the gas is governed by a positive temperature gradient and a wall temperature which is higher than the bulk temperature of the profile. The profile, however,

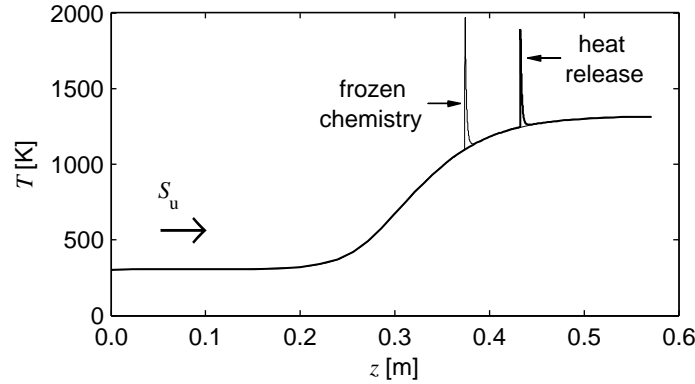


Figure 3.4 Simulated gas bulk temperature, T , profiles from models which use an interfacial heat transfer sub-model with frozen chemistry (thin line) and with heat release, $Le = 1.0$ (thick line). $\phi = 1.0$, $S_u = 0.85$ m/s, $T_u = 300$ K, $T_{af} = 2223$ K. Detailed chemistry is provided by the GRI-Mech 3.0 kinetics mechanism [5].

begins to appreciably change due to chemical energy release. At location z_2 , heat accumulating near the walls switches the sign of the wall temperature gradient which changes the direction of energy transfer. Interestingly, the gas loses heat to the wall even though the wall temperature is still above the bulk temperature of the profile. At the location of peak energy release (z_3), the bulk temperature is higher than the wall temperature. There is, therefore, a competition between the increase in temperature by chemical reactions and wall heat loss. The steep gradient of the temperature profile near the wall at z_3 is caused by the release of chemical energy and leads to higher heat loss in the reaction zone than for the solution that relies on an interfacial heat transfer formulation with frozen chemistry (see Figure 3.2 for comparison). In the cool-off region at location z_4 , the temperature profile has changed from being concave to convex as energy is transferred from the gas to the wall and the gradient has reduced to a nearly fully-developed value. Chemical energy release is not significant at this location. Finally, at location z_5 the gas has cooled while the wall temperature has continued to increase such that the gas temperature profile is once again below the temperature at the wall.

Comparison of the Q_w terms derived from the interfacial heat transfer solutions, in Figure 3.6, gives the reason for the apparent discrepancy in flame position. In this figure, a negative value indicates heat loss from the gas to the wall. The heat release rate in the reaction zone of the boundary layer profile with heat release is much larger than with frozen

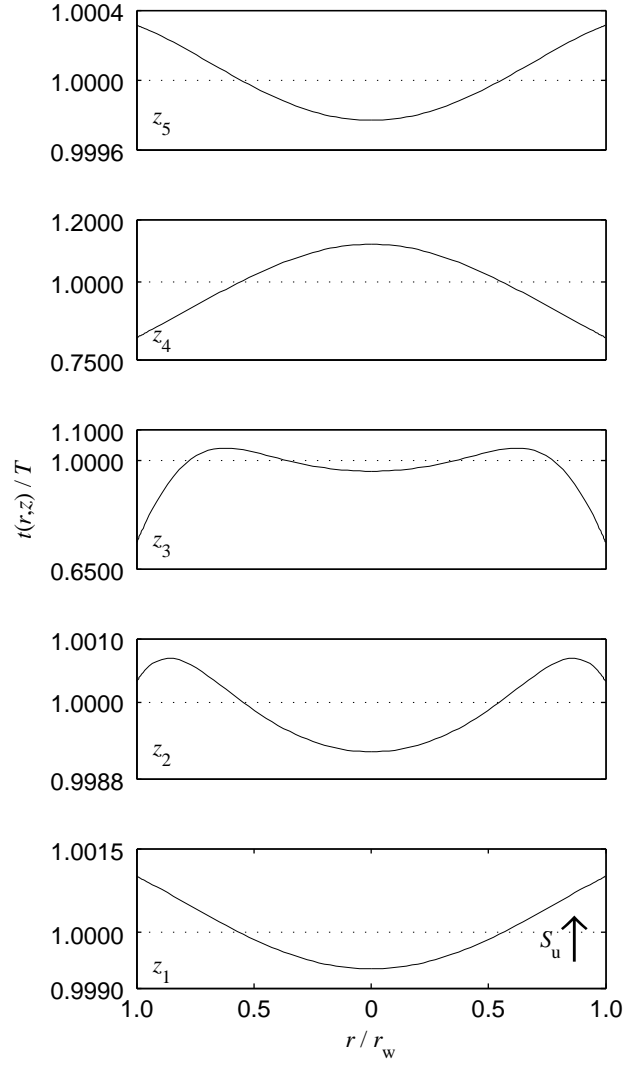


Figure 3.5 Radial gas temperature, $t(r, z)$, profiles from the interfacial heat transfer sub-model with heat release, $Le = 1.0$. These profiles are normalized by the gas temperature, $T(z)$. $z_1 - z_f = -2.7$ mm, $z_2 - z_f = -0.5$ mm, $z_3 - z_f = 0.0$ mm, $z_4 - z_f = 1.2$ mm, $z_5 - z_f = 28.4$ mm. $\phi = 1.0$, $S_u = 0.85$ m/s, $T_u = 300$ K.

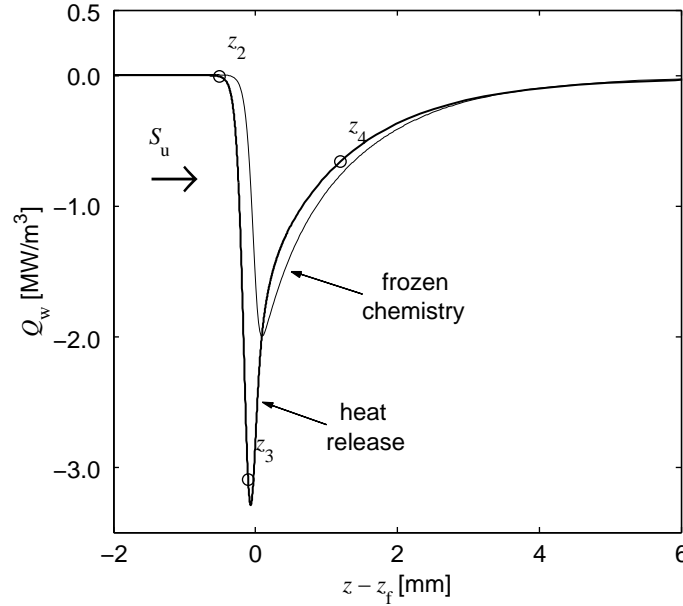


Figure 3.6 Comparison of Q_w profiles obtained from interfacial heat transfer sub-models which neglect (thin line) and include heat release, $Le = 1.0$, (thick line) to calculate interfacial gas/wall energy heat transfer. $\phi = 1.0$, $S_u = 0.85$ m/s, $T_u = 300$ K.

chemistry (see z_3). The chemical composition and flow rate are the same for both flames, therefore the flame must stabilize at a location of higher wall temperature to increase the heat release rate and make up for increased energy lost within the reaction zone due to interfacial heat transfer.

It is also possible to extract values for the bulk temperature and wall temperature gradient from the interfacial heat transfer solution, to compute a profile for the local Nusselt number, using Equation 2.23. Values for Nu_z centered around the flame are plotted in Figure 3.7. In the unburned and cool-off zones (z_1 , z_4 and z_5), the Nusselt number asymptotes to a relatively constant value of 4.35, which is equal to the value for the non-reacting flow case in Figure 3.3. The assumption of $Nu_z \simeq 4$, widely used in other studies [2, 46, 47], is valid in these zones. However, this value is evidently not valid within the reaction zone. Nusselt number peaks to high values in this zone due to the non-linear effects of heat release by chemical reactions that steepen the temperature gradient near the wall (see locations z_2 and z_3). Following the flame, the gas temperature cools while the wall temperatures rise, leading to a second change in the direction of heat transfer at $z - z_f \approx 16$ mm. The

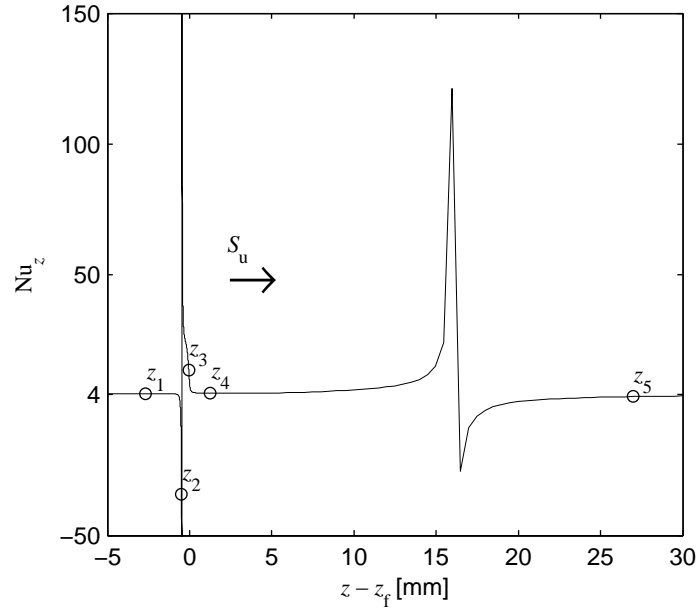


Figure 3.7 Local Nusselt number, Nu_z , profile from the interfacial heat transfer sub-model with heat release, $Le = 1.0$. $\phi = 1.0$, $S_u = 0.85$ m/s, $T_u = 300$ K.

magnitude of the heat transfer at this location is small; however, due to the fact that the temperature difference approaches zero as the two profiles cross each other, the Nu again spikes to large positive and negative values. The highly-peaked and discontinuous Nu values observed at the location where the gas and wall temperature profiles cross each other is not observed in the Q_w profile, which is close to zero at the location where the bulk temperature of the gas equals the wall temperature.

Newton's law of cooling is often used for the interfacial heat transfer term when formulating 1-D flames. Core to this law is the stipulation that heat transfer is driven by a difference between the bulk gas and wall temperatures, $(T - T_w)$. This presents problems when heat release is accounted for in the analysis. When the chemistry activates, the exponential rise in chemical reactivity that accompanies temperature causes a flip in the temperature gradient in the vicinity of the wall from heat gain to heat loss (see z_2 in Figure 3.5). This shift in the direction of heat transfer is not accompanied by a change in the bulk temperature difference. The correct direction for heat transfer can be captured by making the Nusselt number negative, however the ambiguity that this presents reduces the value of Newton's law of cooling as a model for interfacial heat transfer. At location z_3 , the steep temperature gradient near the wall that results from the chemical energy

release leads to a high local heat loss that can only be captured by a correspondingly high Nu value. Therefore, as first pointed out by Norton and Vlachos [41] and subsequently by Veeraragavan and Cadou [66], Newton's law of cooling does not adequately describe the physics of heat transfer within the reaction zone of a flame.

3.3 The weak flame

Focus shall now fall on the stable, mild combustion regime which exists at very low inlet flow velocities. It is known from the analytical model that combustion in this regime takes the form of weak flames which have very low heat release and have flame temperatures that are not much higher than the wall temperature (see Figure 2.1). As opposed to strongly burning flames, which are affected by heat loss, weak flames rely on scavenging heat from the wall to sustain chemical reactions. The existence of such flames have been experimentally verified by other researchers [48, 58, 77]. Here, weak flames are simulated to determine the relative importance of heat release on the thermal coupling between the gas and the wall.

We shall forgo using methane and, instead, look at the more interesting case of a n-heptane/air mixture. n-Heptane is one of the primary reference fuels and is well known to exhibit multi-stage ignition behaviour. The interaction of this kinetic behaviour and molecular diffusion produces more complex behaviour in this system. The mechanism employed is that of Seiser et al. [81], which is a reduced mechanism for n - C_7H_{16} combustion and has 159 species and 770 reversible reactions. This mechanism is found to reproduce ignition delay times in homogeneous reactors and concentration histories of key species in plug flow and jet-stirred reactors. However, the coupling between low temperature chemistry and molecular transport is less understood.

Figure 3.8 shows the structure of the weak flame which results from the numerical calculations. As was the case for strongly burning flames, results have been shown for volumetric models which use an interfacial heat transfer sub-model with frozen chemistry and with heat release. As expected, the gas temperature does not stray far from the wall temperature. This low temperature difference results from very low heat release at these flow velocities, which are much smaller than the flame speed of this mixture ($S_L \approx 0.46$ m/s at 300 K).

Heat release, and the corresponding consumption of chemical enthalpy, occurs in three

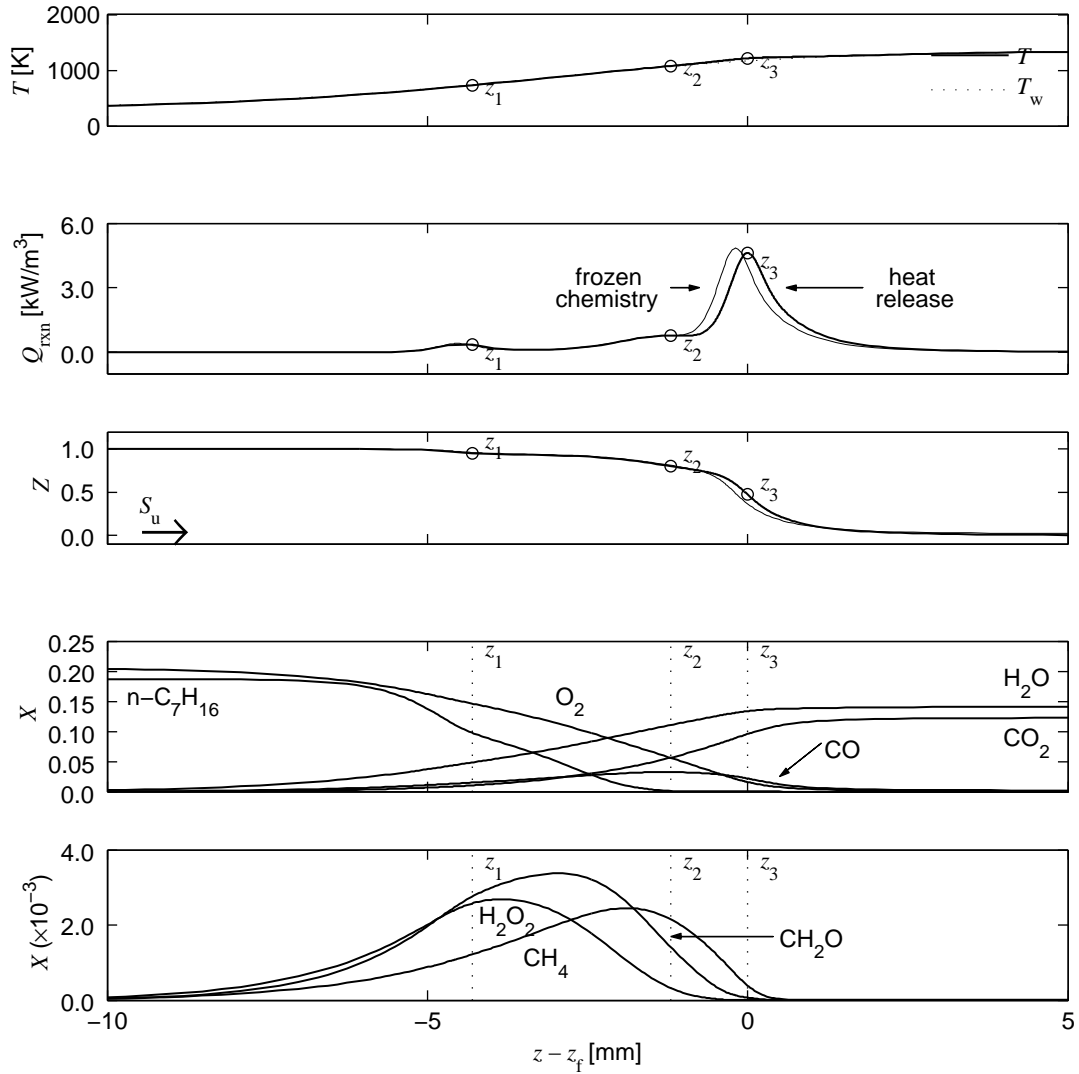


Figure 3.8 Simulated bulk temperature, T , heat release, Q_{rxn} , Z and a selection of species profiles for weak, stoichiometric $n - \text{C}_7\text{H}_{16}$ /air combustion. $\phi = 1.0$, $S_u = 2.0$ cm/s, $T_u = 300$ K. An interfacial heat transfer sub-model is used with heat release, $Le = 1.0$ (thick lines), or frozen chemistry (thin lines) to model interfacial heat transfer. The positions z_1 , z_2 and z_3 show the locations of peak heat release for the cool, blue and hot flames, respectively.

stages marked in the figure as z_1 , z_2 and z_3 . At z_1 , chemical reactions are activated at approximately 700 K to produce the first drop in chemical enthalpy. At this peak the consumption of $n - \text{C}_7\text{H}_{16}$ and O_2 coincide with the formation of H_2O_2 and CH_2O . This is a typical chemical process in cool flames [82]. H_2O_2 and CH_2O are consumed at higher

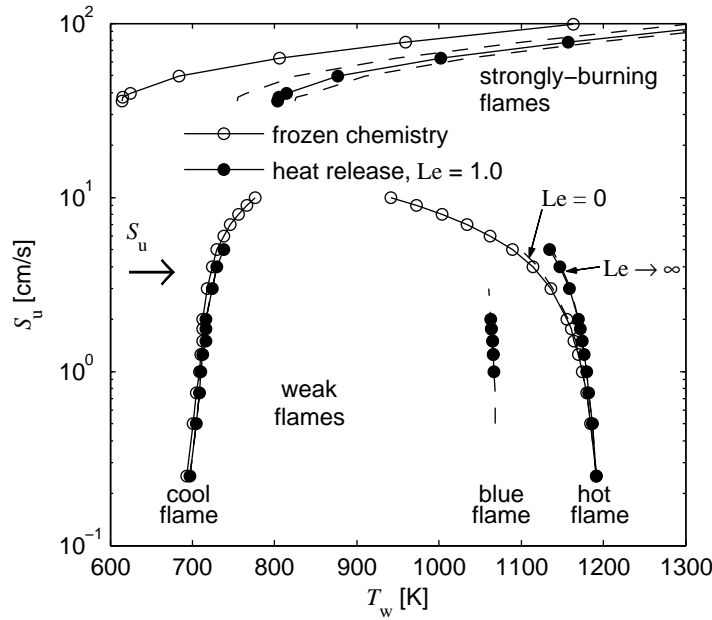


Figure 3.9 Locations of peak heat release for weak, stoichiometric $n - C_7H_{16}$ /air combustion at low inlet flow velocities, S_u . An interfacial heat transfer sub-model is used with frozen chemistry (open circles) or with heat release, $Le = 1.0$ (closed circles) to model interfacial heat transfer. Dashed lines to the left and right of the model with heat release show the limits $Le = 0.0$ and $Le \rightarrow \infty$, respectively.

wall temperatures, $T \approx 1050$ K, close to the second peak in heat release at z_2 . This process is often called blue flames, due to chemiluminescence of CH_2O . At z_2 , $n - C_7H_{16}$ has been fully consumed, but more than half of the chemical enthalpy remains in the mixture. This energy is locked up in hydrocarbon intermediate species. The species profile for CH_4 is shown here, but some hydrocarbons are present in higher concentrations. The remaining chemical enthalpy is liberated at z_3 , $T \approx 1200$ K, in a comparatively large release of heat. In this zone, all remaining unburned species are completely oxidized to CO_2 and H_2O . Thus consumption of $n - C_7H_{16}$ and air is found to occur in a three-stage process, in cool, blue and hot flames, respectively, over a broad reaction zone which is approximately five times the conventional flame thickness for this mixture. The chemical processes found in these results are also consistent with multi-staged ignition phenomenon found in the literature.

Simulated flame stabilization data for the range of flow velocities which produce strongly burning and weak flames is shown in Figure 3.9. The locations in this figure correspond

to peaks in heat release. Again, data is shown for the volumetric model which uses frozen chemistry and heat release for interfacial heat transfer. In the high velocity region, only a single peak for heat release is obtained for strongly burning flames. There is also a large discrepancy between the models owing to the effects of heat release on flame / wall energy transfer. Multi-staged ignition behaviour appears at low inlet velocities, where multiple heat release peaks corresponding to cool, blue and hot flames are observed. In contrast to strongly burning flames, there is little difference between the stabilization positions of the models. Therefore, the position of weak flames are less sensitive to heat loss in the reaction zone due to the small magnitude of heat released at these very low burning rates. However, the discrepancy between the models grows with mass flow rate as more reactants are consumed, increasing the heat released by the flame.

Chapter 4

Experimental investigation

In Chapter 2, a model was developed to describe stabilized combustion in small, heated channels with dimensions on the order of the flame thickness. The strong effects of heat release on interfacial heat transfer and the resulting structure of these flames was then discussed in Chapter 3 using model predictions. Conclusions derived from these chapters are interesting, but are incomplete without experimental verification.

Numerous studies have tried such comparisons before in a heated channel configuration (see, for example [38, 46, 48]). These studies report generally good agreement in qualitative trends, but poor quantitative agreement between model predictions and experimental measurements. It is shown in Chapter 3 that much of this failure lies in the model formulation; however, there are additional factors relating to the execution of experiments which cause large uncertainties in flame stabilization position.

4.1 The apparatus

Figure 4.1 shows a simplified schematic of the apparatus used in present experiments. The apparatus consists of a flow system to meter the combustible mixture, a furnace to provide external heating, and a flow tube as the channel wall. A detailed schematic of the furnace assembly is also provided in Figure 4.2.

Experiments are performed using a quartz tube to have optical access to the flame and to minimize heterogeneous wall reactions. The downstream (top) portion of the tube is circumferentially heated by a pair of temperature-controlled 900 Watt radiant heaters,

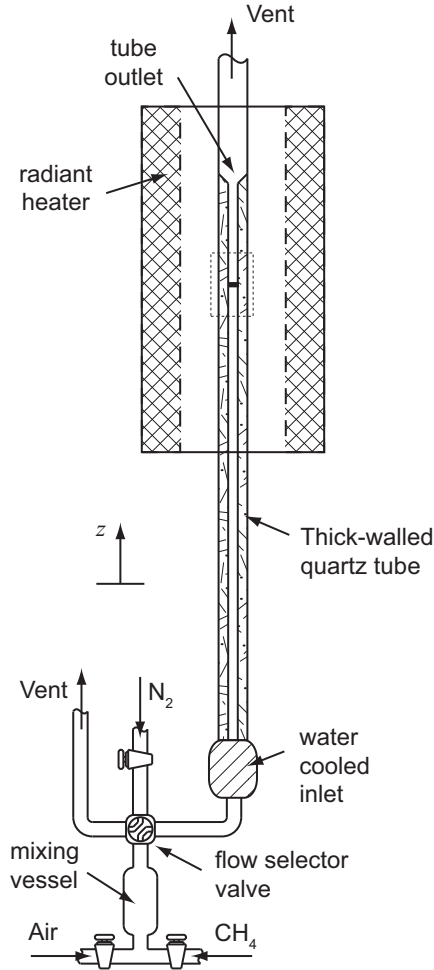


Figure 4.1 Schematic of apparatus. A detailed view of the furnace assembly is in Figure 4.2.

designed to produce an axially varying, but circumferentially uniform, steady temperature profile along the tube wall. This furnace geometry was chosen due so that the assembly could be modeled by simple heat transfer models (see Appendix B) so that a smooth temperature profile could be designed for the tube wall.

Stabilized flames are produced when metered methane / air mixtures at variable total flow rates are supplied at the inlet (bottom) of the tube. A stoichiometric composition is used to reduce the effect of errors in the flame model due to uncertainties in the kinetic rates found in chemistry models under lean and rich conditions [83]. Additional results for the effects of mixture composition are presented in Appendix C and [84]. The inlet boundary

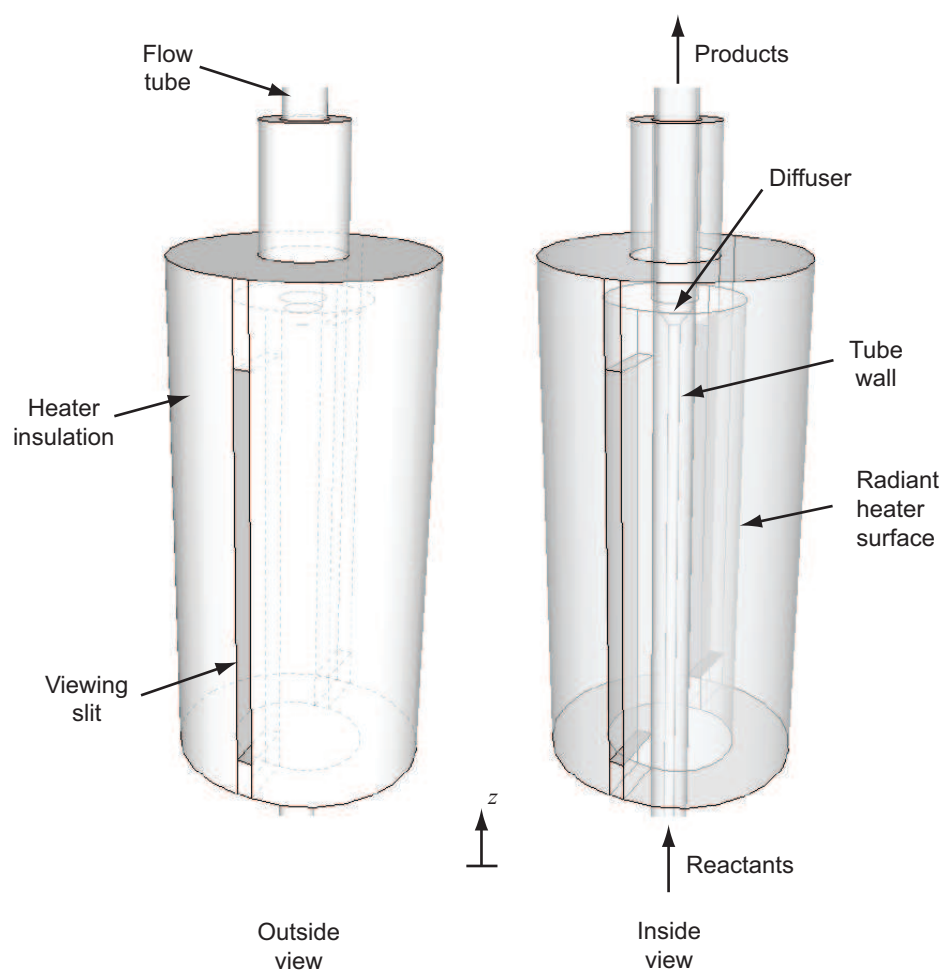


Figure 4.2 Schematic of furnace assembly. The schematic is not to scale.

condition of mixture composition and inlet total flow rate are controlled by two Brooks mass flow controllers. The uncertainty in the equivalence ratio and flow velocity is not greater than $\pm 0.7\%$ and $\pm 1.2\%$, respectively. Outlet boundary conditions are at a chamfer which creates a diffuser at the exit. The chamfer geometry also allows for communication (via radiation) between the end walls to minimize tube end energy losses and generates a flat outlet wall temperature gradient while also helping to suppress the effects of flow separation. The outlet tube is thin walled to minimize the leakage of heat vertically along the z axis.

There is a thin, 2 mm wide slit in the circumferential heaters along the z axis to provide visual access to the tube inside the heated zone. The inner circumference of the heater is approximately one hundred times this slit width, therefore, keeping the energy loss out of the slit to a minimum. CH emission is used as the marker for flame position. The CH emission profile is obtained from photographs using a cooled 14 bit CCD (Cooke PCO-2000) and 90 mm macro lens with a 5 nm band-pass filter (Andover) centered around 435 nm.

There are three factors which deserve additional attention when designing an experiment for the heated channel configuration. In previous studies, it was common practice to heat channels non-uniformly, using forced convection, and to place apparatuses in a horizontal orientation. This produced non-symmetric flames, buoyancy effects, and complex boundary conditions. These undesirable effects can be eliminated by using a vertically oriented channel and radiant heating to produce a circumferentially uniform wall temperature gradient. Another factor is the length of the wall temperature profile used in previous experiments. Previous apparatuses used wall temperature profiles which were spatially compressed, with lengths on the same order as the flame thickness. These profile lengths are convenient to produce, but are difficult to measure with high certainty. The small length also produces non-adequate temperature sensitivity in the apparatus which leads to minute differences in stabilization position between different operating conditions. In the present apparatus, a long wall temperature profile is used to obtain a much higher sensitivity and, therefore, much lower uncertainties in stabilization position than were possible with previous experiments. The final factor relates to operating parameters used in the experiments. In previous studies, experiments were often performed under conditions outside of the applicable range of 1-D volumetric model assumptions. This is obviously an unfair test of a model, which should only be validated within the assumptions used in its formulation.

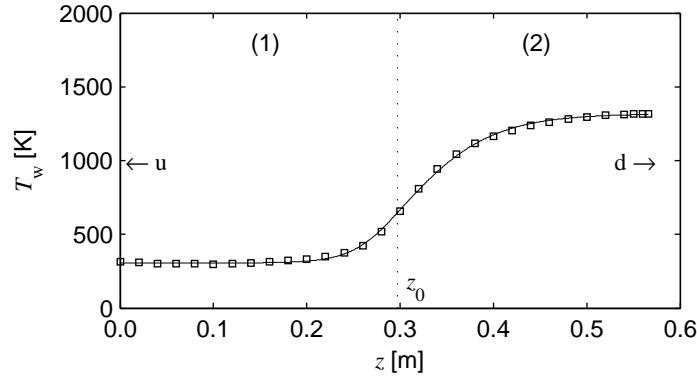


Figure 4.3 Measured wall temperature profile, $T_w(z)$. Measured data points are the open squares in this figure. The length of the profile and the maximum wall temperature is $z_b = 0.5714$ m and $T_{w,b} = 1312$ K, respectively. The measurements are fit via linear regression by two sigmoidal profiles (—) which are connected at z_0 for input into the computational model. The inside tube diameter is 1 mm.

4.2 Wall temperature profile

The wall temperature profile in Figure 4.3 was measured in advance of the experiments along the inner surface of the tube wall with a K-type thermocouple of 0.5 mm nominal thickness. The flat inlet temperature region is achieved by water cooling to create a region which is long enough to achieve a hydrodynamically fully developed flow at the inlet. At the outlet, the highest downstream wall temperature is $T_{w,d} = 1312$ K, which is sufficient to induce auto ignition, but is lower than the adiabatic flame temperature of the mixture. The measurements are fit with two connected sigmoidal profiles which meet at z_0 for input into the computational model:

$$T_w(z) = \begin{cases} T_{w,u} + (T_{0,1} - T_{w,u})/[1 + \exp(-(z - z_0)/\omega_1)] & \text{if } z \leq z_0 \\ T_{0,2} + (T_{w,d} - T_{0,2})/[1 + \exp(-(z - z_0)/\omega_2)] & \text{if } z > z_0 \end{cases}, \quad (4.1)$$

where $T_{w,u} = 306$ K, $T_{w,d} = 1312$ K, $z_0 = 0.297$ m, $\omega_1 = 0.0246$ m, and $\omega_2 = 0.0485$ m. The constants $T_{0,1}$ and $T_{0,2}$ are determined by matching the temperature and gradient at z_0 . It should be noted that the length of the temperature ramp used here is quite long (greater than 0.3 m), when compared to similar apparatus Maruta et al. [46]. The increased length has the important benefit of boosting the sensitivity of the apparatus in the respect that small changes in heat release from the flame cause large changes in flame position.

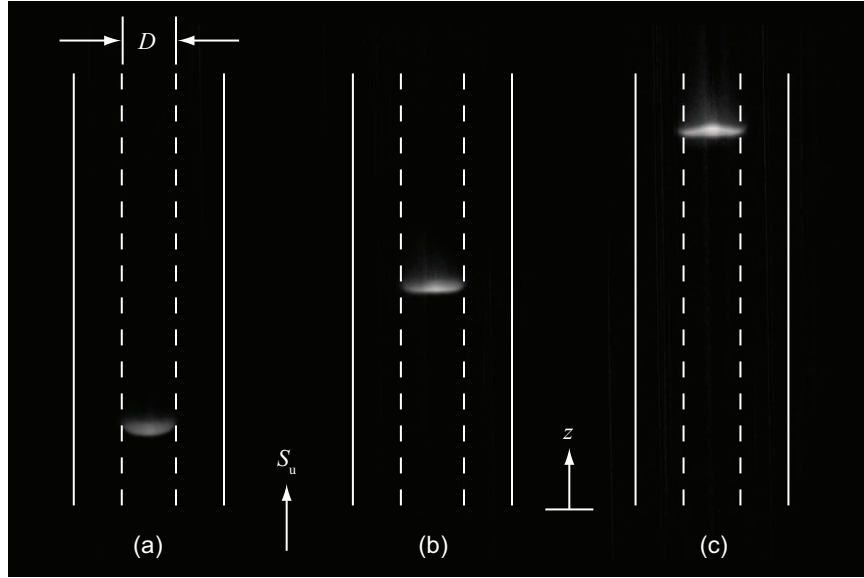


Figure 4.4 CH emission from stoichiometric flames in the heated channel ($D = 2$ mm). The solid and dashed lines show the approximate positions of the inner and outer walls of the tube, respectively. Flames move further downstream with increasing flow velocity, however the actual change in position between these cases is on the order of 1 cm, which is larger than what is depicted in this figure. (a) $S_u = 0.7$ m/s, (b) $S_u = 1.0$ m/s, (c) $S_u = 1.4$ m/s.

4.3 Flame stabilization and curvature

Figure 4.4 shows CH emission profiles for the stoichiometric flames, stabilized in the channel at different flow velocities, in a $D = 2$ mm channel. For the lowest flow velocities used, the flame ignites and then stabilizes, as it has done in (a), at an upstream position in the lower temperature region of the tube. When the flame is perturbed by an increase in the flow velocity, it adjusts by moving downstream to a new location, shown in (b), in the higher temperature region of the tube. This behaviour can be repeated by applying even greater flow velocities, in (c), until blow off inevitably occurs at the upper limit of the gradient in the wall temperature profile.

In Figure 4.4(c), curvature is detected in the flame front at the highest inlet flow velocities. The curvature is small, but it was found to rapidly grow with increasing tube diameter, similar to the parabolic dependence of burning rate in Figure 1.6 (also, see Appendix C). In order to satisfy Equation 1.12, it is, therefore, necessary to use a tube of small bore. A 1 mm internal diameter is used as a compromise between this condition and the quenching

distance for the achievable wall temperature. The higher heat loss of smaller tubes would have to be offset by higher wall temperatures, which are not practical with the present apparatus. Nevertheless, the 1 mm diameter channel is found to suppress curvature. Flames are observed to be flat over the range of conditions used in the experiments, which satisfies a key assumption in the volumetric model formulation.

4.4 Uncertainties due to local wall heating

Such experiments are inherently affected by heat conduction through the solid walls. This phenomenon can affect the tube wall temperature profile and the burning rate. In the reaction zone, the gas temperature is higher than in the wall. Therefore, the influence of wall heat conduction cannot be completely eliminated from the experiments. The total rate of heat release from the flames in this study is approximately 1 – 2 Watts, which is three orders of magnitude smaller than the output of the heaters. This magnitude is small, but it is inevitable that heat will be soaked up by the wall to raise its temperature. An important feature of the apparatus was to design the wall to delay and minimize this temperature rise. The large volumetric heat capacity and relatively small solid thermal conductivity of quartz results in a thermal diffusivity which is two orders of magnitude smaller than the gas mixture. The walls are also made thicker, with an outer-to-inner diameter ratio of 11, to add thermal mass to the tube, which reduces the rate of rise in the wall temperature.

Flame position measurements are also done as separate trials at different inlet flow velocities. Upstream of the tube inlet a flow selector valve controls two constant streams. Nitrogen is initially used to condition the tube from chemical and wall temperature effects from previous trials. Then the trial begins by switching the inlet stream to the methane and air mixture. Some time is needed for the initial slug of methane and air to traverse the length of the tube and to increase its temperature, but the ignition that results at the tube outlet produces a combustion wave in the mixture.

Figure 4.5 shows a plot of flame position against time for a typical trial as it settles in the wall temperature gradient. The settling process is split into three regimes that depend on the physics of flame propagation. In the first regime, the flame initially comes into view as it flashes back into the wall temperature profile. Flashback is rapid at first, but the flame progressively slows as it feels lower temperatures in the wall. In this regime, the flame moves at a speed which is too fast to have an appreciable effect on the local wall temperature. The

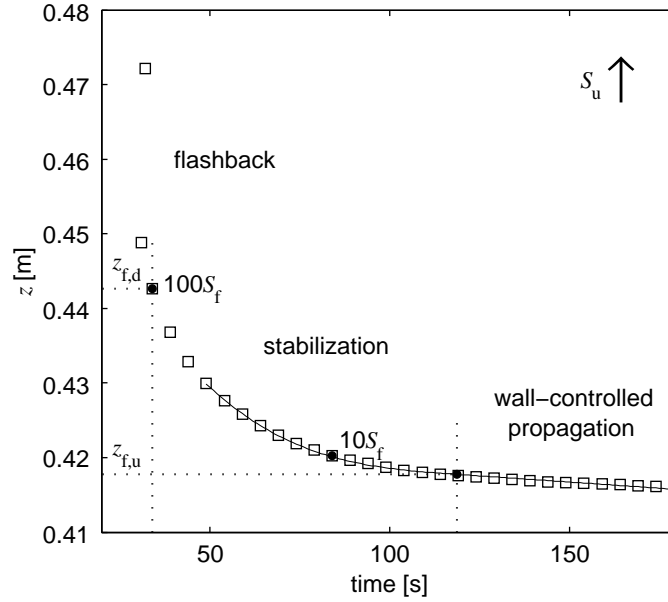


Figure 4.5 $\phi = 1.0$, $S_u = 0.80$ m/s, $T_u = 300$ K. Position of peak CH location versus time for one experimental trial. The experimental track (squares) captures flashback, stabilization between $z_{f,u}$ and $z_{f,d}$, and the subsequent wall-controlled flame propagation due to local wall heating. $z_{f,u}$ is at the intersection of a fitted polynomial and straight line (—). The velocity thresholds for $z_{f,d}$ are $10S_f$ and $100S_f$. For this trial, the final countercurrent propagation speed after stabilization is $S_f = 1.4 \times 10^{-5}$ m/s, or less than 0.002% of the inlet flow velocity.

second regime is stabilization, which is bracketed by the locations $z_{f,d}$ and $z_{f,u}$ in the figure. At the downstream flame location $z_{f,d}$, transition from flashback to stabilization is deemed to occur when the countercurrent propagation speed of the flame falls below a threshold value governed by the heating rate in the wall, as discussed below. After $z_{f,d}$, the flame continues to slow as heat is lost to the wall until it reaches the upstream flame location, $z_{f,u}$. In the final regime upstream of $z_{f,u}$, the flame settles to a constant minimum velocity, S_f , that is indicative of a countercurrent (to flow direction) wall-controlled propagation governed by heat recirculation [49]. However, this final propagation speed is small and is less than 5.0×10^{-5} m/s for all trials in the experiment.

An assumption in most models of temperature-stabilized flames is that the wall temperature does not change significantly during the stabilization regime [38, 46, 73]. This experimental investigation will also use this assumption in Section 2.3 as a wall boundary

condition to compute the structure of these flames. The numerical solution for flame structure has a unique stabilization position, z_f , in the steady wall temperature gradient, but there is a problem when the solutions are compared to experiment. As discussed above, it is expected that the wall temperature would incrementally increase over the time scale of propagation from $z_{f,d}$ to $z_{f,u}$, leading to higher local wall temperatures surrounding the flame. In order to compare the model to experiment, $z_{f,d}$ and $z_{f,u}$ can be used as two limiting flame positions that are directly compared to the modeled stabilization position. Downstream from $z_{f,d}$, local wall temperatures would not change over the brief time that this area is in contact with the flame. This can be contrasted by locations upstream of $z_{f,u}$ where, in the vicinity of the flame, the highest modified local wall temperatures would be produced. Consequently, an accurate model which assumes a steady wall temperature would predict a stabilization position, z_f , that would lie between the bounds $z_{f,d}$ and $z_{f,u}$. The degree of separation of these bounds would, therefore, represent the overall uncertainty in experimental flame stabilization position.

This concept can be illustrated by looking at a hypothetical case of a wall that would not absorb heat. For this case, a flame lit at the downstream end would flashback rapidly through the zone of no temperature gradient. Then the wall temperature would start to drop as the flame propagated further upstream into the wall temperature profile. The flame would lose more heat slowing its propagation until it finally came to rest at a unique stabilization position. A plot of position against time for this case would look similar to Figure 4.5, except that the experimental track would go horizontal at the end ($S_f = 0$) and there would be no wall-controlled region. There would therefore be no uncertainty in the experimental stabilization position and thus, $z_{f,d}$ would collapse to $z_{f,u}$. This experimental track would be modified if the wall were allowed to participate in the stabilization process. The effect of a slight increase in local wall temperature due to wall heating would be a small final propagation speed and negligible uncertainty in flame stabilization position. However, as the wall participates more in the process, the flame would stabilize further upstream due to the thermal inertia of the wall. The final countercurrent propagation speed would also increase proportional to the rate of local wall heating. This would produce progressively greater differences in the upper and lower bounds of the stabilization regime and greater uncertainty in experimental flame position.

Identification of the second and third stages of propagation allows for criteria to be developed for the parameters S_f , $z_{f,u}$ and $z_{f,d}$. The upstream location, $z_{f,u}$, is defined as

being at the intersection of the stabilization and wall-controlled propagation regimes and is determined by a regression analysis of the data to fit a polynomial matched to a straight line to model these propagation stages. S_f is the slope of the straight line and is a measure of the final propagation speed of the flame. Therefore, $z_{f,u}$ and S_f are fitting parameters in this analysis and are determined by a best fit to the experimental data via error minimization. $z_{f,d}$ is the upper bound of the stabilization regime. This location is at the transition from flashback to stabilization which occurs when the countercurrent propagation speed falls below a threshold speed of propagation. As discussed above, the transition from flashback to the stabilization region results in an uncertainty in the flame position that should scale with the final propagation speed, S_f . The threshold speed is set to be a multiple of this speed. To demonstrate the sensitivity of $z_{f,d}$ to this threshold, values of $10S_f$ and $100S_f$ have been used. It is shown in Section 4.5 that a higher threshold speed would be too fast for the flame to have a significant effect on the local temperature of the wall.

The present experiments have been designed to maximize changes in flame location that accompany changes in heat release by using a shallow wall temperature gradient. Typically, studies of such flames have employed much steeper gradients. This would lead to a smaller difference between $z_{f,u}$ and $z_{f,d}$ at the cost of lower sensitivity of the flame position to changes in heat release, and heat transfer to the wall. The extremely slow countercurrent flame propagation speed, S_f , in Figure 4.5 results from the efforts made in designing this experiment to minimize the effects of wall heating, as discussed above, but such effects can never be completely eliminated from any experimental realization of a flame in a small channel.

4.5 Model validation

A summary of flame position data obtained experimentally versus inlet velocity is shown in Figure 4.6. The experimental data in this figure is displayed as a range of flame locations connected by horizontal lines at each inlet flow velocity. These lines bounded by the upstream, $z_{f,u}$, and downstream, $z_{f,d}$, locations of the stabilization regime show the experimental uncertainty in flame stabilization position. Two locations are given for the downstream bound, $z_{f,d}$, as thin and thick vertical lines at $10S_f$ and $100S_f$, respectively.

Stoichiometric flames in the range $0.75 \text{ m/s} \leq S_u \leq 1.00 \text{ m/s}$ are strongly burning, stable, symmetric flames. In Figure 4.6, the flame moves a total distance of 77 average flame

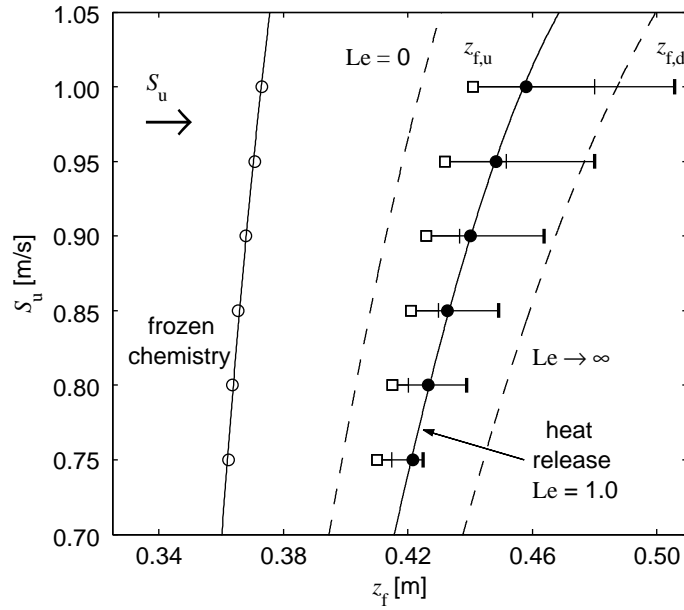


Figure 4.6 Inlet flow velocity, S_u , verses simulated (—) and experimentally determined stabilization position, z_f . Experimental data is shown as a range of locations by horizontal lines between the upstream, $z_{f,u}$ (squares), and downstream bounds, $z_{f,d}$ (vertical lines), of the stabilization regime. The thin and thick vertical lines are for $z_{f,d}$ determined at $10S_f$ and $100S_f$, respectively. The model uses an interfacial heat transfer sub-model with frozen chemistry (open circles) or with heat release, $Le = 1.0$ (closed circles), and the GRI-Mech 3.0 kinetics mechanism. Dashed lines to the left and right of the model with heat release show the limits $Le = 0$ and $Le \rightarrow \infty$, respectively.

thicknesses downstream to higher wall temperatures with increasing inlet flow velocity.¹ For flame stabilization to occur, the energy needed to preheat the large flux of reactants must be balanced by heat gained from wall heat transfer and chemical reactions. When the flame is perturbed by higher flow velocities it requires more energy to heat the reactants due to the increased mass flow entering the system. Reaction rate is a function of temperature, therefore the flame cannot immediately adjust to the added mass flow by generating higher heat release due to chemical reactions. It must therefore move to a higher wall temperature where the energy needed can be balanced by increased heat transfer from the tube wall and higher reaction rates at the increased local temperature.

¹Flame thickness is calculated from the simulated flame profiles using twice the full-width at half maximum of Q_s , fitted with a gaussian profile, and is $\sim 96\%$ of the energy in Q_s .

Figure 4.6 also shows the stabilization positions for numerical solutions. These simulations are performed with the CANTERA software package [85] and with thermo-chemical data from the GRI-Mech 3.0 kinetics mechanism (GRI 3.0) [5]. GRI 3.0 is a detailed kinetics mechanism which was developed and optimized for natural-gas combustion, including NO formation. The mechanism contains 53 species and 325 reactions. Flames simulated with an interfacial heat transfer sub-model with frozen chemistry predict positions which are consistently upstream of those obtained experimentally. There is considerable disagreement between the experiments and model, with predicted stabilization positions located an average of 138 flame thicknesses upstream from $z_{f,u}$. The position of these solutions are also upstream from the $Le = 0$ limit, which represents the lowest possible heat loss for a flame when chemical energy release in the interfacial heat transfer sub-model is considered. Therefore, the upstream deviations in flame stabilization position are a direct result of an under prediction of heat loss inside the reaction zone. In contrast to the solution with frozen chemistry, inclusion of the heat source term in the interfacial heat transfer sub-model, with a $Le = 1.0$, predicts stabilization positions which are, on average, 34 flame thicknesses downstream from the lower bound in the experimental data. The agreement between model and experiment is very much improved, with the simulated stabilization positions lying between the range defined by the upper and lower bounds of experimental flame location.

Both models show considerable spread when deviations in flame position are normalized by the flame thickness. There is also a seemingly large variability in the experimental stabilization range, between 34 and 143 flame thicknesses for this range of inlet flow velocities, which makes it difficult to make further assessments between the interfacial heat transfer formulations and the experiments. This is due to the fact that the magnitude of the wall temperature gradient varies significantly between the two predicted stabilization positions.

Simulated flame stabilization position can also be sensitive to some of the hundreds of empirical rate constants found inside a detailed kinetics mechanism. GRI 3.0 is widely used, but it is not the only mechanism available for methane combustion. Other mechanisms have slightly different elementary kinetic rates which result in different simulated flame behaviors. As such, solutions from a selection of mechanisms, including GRI 3.0, are compared here to determine the extent of variability in the simulated flame position due to differing elementary reactions and rate constants. The smallest mechanism used in this comparison is GRI-Mech 1.2 [86] (GRI 1.2). It is a compilation of 32 species and

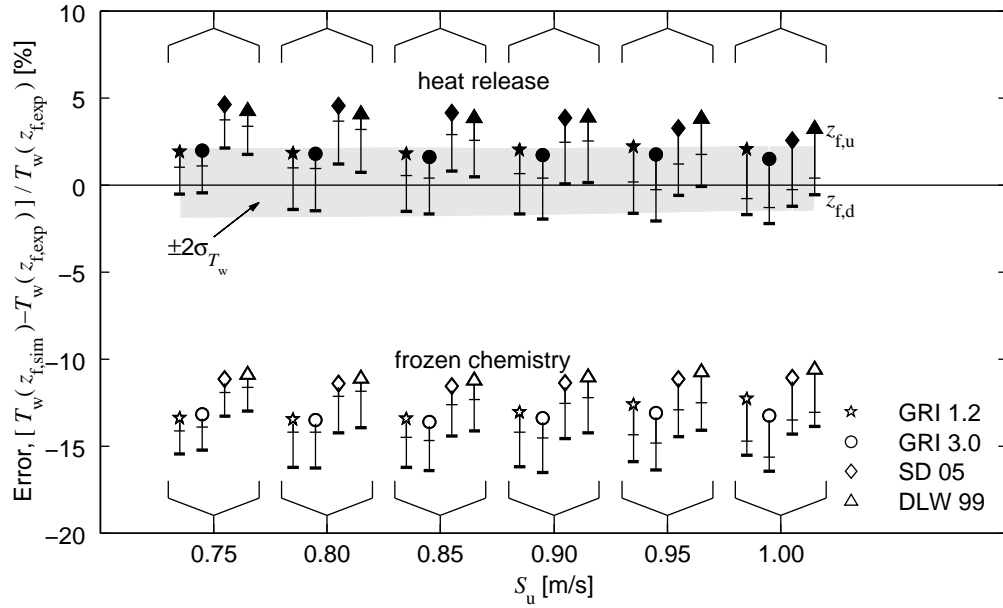


Figure 4.7 Error in the predicted wall temperature, T_w , at the simulated flame position, $z_{f,sim}$, compared the experimental flame, z_f , for a variety of detailed kinetics mechanisms. Legend as in Figure 5.2. The shaded error band represents the $\pm 2\sigma$ total uncertainty in the model with heat release due to experimental operating parameters and measured boundary conditions using GRI-Mech 3.0 as the reference.

177 elementary reactions for C_1 chemistry. GRI 1.2 is an optimized model which is fit to a wide variety of experimental data: namely ignition delay, flame speeds and species concentrations. An alternative mechanism is the San Diego Mechanism [87] (SD 05) which contains 46 species and 235 reactions. It is built on a philosophy of limiting the number of species and elementary reactions to the minimum needed to model high temperature chemical reactions. Finally, a mechanism by Davis et al. [88] (DLW 99) is also used which describes the combustion of C_1 to C_3 hydrocarbons. DLW 99 has 71 species and 469 reactions. The tendencies of some of these mechanisms to converge are more robust than others, therefore it can sometimes be difficult to obtain solutions. However, this problem is alleviated by using the continuation strategy of Benezech [89] which provides a smooth transition from one kinetics mechanism to another while stepping towards the solution.

In the work of Minaev et al. [47], it is shown that the flame temperature and local wall temperature are the eigenvalues of the problem that leads to a unique stabilization position

in the monotonically increasing wall temperature profile. Therefore, Figure 4.7 shows the relative error in wall temperature between the predicted and experimentally-observed flame stabilization positions. A gray-filled error band is also included in the figure to account for uncertainty in the model predictions which arise from uncertainties in the model boundary conditions, such as the flow rate, mixture composition and wall temperature profile, which are obtained from experimental measurements. These uncertainties are propagated through the model to determine the uncertainty in the predicted wall stabilization temperature by using the logarithmic sensitivity of each boundary condition, as described in Appendix E.

Data is plotted for the four kinetics mechanisms GRI 1.2, GRI 3.0, SD 05 and DLW 99. In this comparison, the error in wall temperature at the upstream and downstream bounds of the experimental stabilization regime, $z_{f,u}$ and $z_{f,d}$, are connected by the vertical lines. The downstream bound uses the velocity thresholds $10S_f$ and $100S_f$, and are displayed as the thin and thick horizontal lines, respectively. For the threshold of $10S_f$, the downstream bound expands in a non-linear manner into higher wall temperatures with increased flow velocity. This threshold is sensitive to the increased heat release of flames at the higher mass flows which produce an increased flux of heat to the wall. Contrary to the $10S_f$ threshold, $100S_f$ shows a range which plateaus and is more or less constant at higher inlet velocities. This suggests a much lower sensitivity to heat release and, thus, a more appropriate threshold for the downstream bound.

For all kinetics mechanisms, interfacial heat transfer solutions with frozen chemistry result in an average relative error of approximately 11–15%, or 131–199 K, upstream from the experimental data. These solutions lie well outside the uncertainty band for the model predictions. Accounting for heat release, however, reduces the relative error in wall temperatures so that model predictions cluster in a range of positions 1.2% upstream and 4.5% downstream from the experimental data. Some kinetics models are in closer agreement with the experiments than others. GRI 1.2 and GRI 3.0 lie within the uncertainty band, SD 05 is found to lie within this range only at high inlet velocities, and DLW 99 tends to be slightly downstream from the experiments. The variability in predicted flame stabilization position from different chemistry models is smaller than the discrepancies with frozen chemistry and, overall, the reactive interfacial heat transfer formulation overlaps the experimental data. These results demonstrate the importance of incorporating heat release into the interfacial heat transfer model.

4.6 Conclusions

In Chapter 2, a new formulation is presented which extends the standard 1-D, volumetric model for a flame stabilized inside a small tube with a steady wall temperature profile. In this new model, an interfacial heat transfer sub-model is considered which uses a 2-D, axisymmetric, axially developing thermal boundary layer with heat release derived from the reacting 1-D bulk flow. The new formulation replaces common assumptions for Nusselt number with a new sub-model which accounts for the effects of chemical energy release on local temperatures.

In Chapter 3, the influence of combustion chemistry on heat loss is demonstrated by solving the model with and without the effects of the heat source. Flames that result from these interfacial heat transfer profiles show marked differences in peak temperature and position. These differences coincide with the magnitude of heat loss predicted by the models. It is also found that magnitude of heat loss is sensitive to heat release, which produces steep temperature gradients at the wall in the reaction zone, and that stabilized flames must adjust to the enhanced heat loss by moving to locations of higher wall temperature. The study, therefore, demonstrates that the spatial details of heat release are important for strongly burning flames and that accurate predictions of heat loss must account for effects of chemical energy release. These findings are reported in Watson and Bergthorson [90].

In this chapter, the volumetric model is validated with a specially designed apparatus. It is found that 1-D volumetric simulations which neglect the effects of chemical energy release underestimate heat loss resulting in predicted stabilization positions that are consistently upstream of experimental flames. Contrastingly, the new formulation offers improved estimates for the interfacial heat transfer profile and predicts flame positions at wall temperatures that are close to those obtained experimentally. The two possible limits of the new model for reactant diffusivity of $Le = 0$ and $Le \rightarrow \infty$ also span the data, and the experiments lie between these limits, as expected for a stoichiometric methane-air flame. Therefore, the results show that heat loss by interfacial heat transfer is a dominant phenomenon which defines the position of these flames and that significantly-improved agreement can be achieved using the simplified model developed in this dissertation.

Chapter 5

Detailed simulations

The volumetric model, in Chapter 2, makes use of several approximations to generate an interfacial heat transfer profile. These approximations should, again, be explicitly stated. The first approximation is use of a single, effective Lewis number to model the rate of radial diffusion of chemical enthalpy. While it is possible to define an exact value for Lewis number, based on the definition of the progress variable, such a number would ignore the multi-component nature of the reacting flow. Energy is contained in several chemical species that diffuse at different rates, thus, there is no way to know the best value of Le in advance of the modeling effort.

The second approximation relates to temperature and reaction rate, and the convolution designed to redistribute bulk energy in the interfacial heat transfer sub-model. In the interfacial heat transfer sub-model, the radial distribution of the heat source is assumed to be proportional to the distribution of chemical enthalpy inside the channel. This dependence is similar to concentration in the Law of Mass Action, where ζ would be analogous to the deficient species, but there is no explicit dependence on the local gas temperature. This approximation would generate inaccuracies in the heat release profile near the wall where there are lower temperatures.

The final approximation relates to momentum. In the interfacial heat transfer sub-model, radial velocity is assumed to be negligible compared to the axial flow in the channel. Bypassing the momentum equation with this assumption results in a model that does not have the capacity to account for radial mass flow due to heat release and the resulting flow dilatation.

In previous chapters, it is shown that the addition of an interfacial heat transfer sub-model, in place of Newton's Law of Cooling, improves numerical predictions when solutions are compared to experimental realizations. However, the above approximations limit the accuracy of such formulations. Therefore, there is a need to understand the degree to which these approximations affect numerical predictions by comparing solutions of the volumetric model to detailed simulations.

5.1 The detailed numerical model

A detailed model for this problem is based on the Navier-Stokes equations for low-Mach number reacting flows. The multi-dimensional, steady-state governing equations for mass, momentum, energy, and species for an ideal gas are shown below:

Continuity:

$$\nabla \cdot (\rho \vec{u}) = 0, \quad (5.1)$$

Momentum:

$$\rho \vec{u} \cdot \nabla \vec{u} = -\nabla p + \nabla \cdot (\mu \mathbf{S}), \quad (5.2)$$

Energy:

$$\rho \vec{u} \cdot \nabla h = \nabla \cdot \left(\frac{\lambda}{c_p} \nabla h \right), \quad (5.3)$$

$$h = \sum_{k=1}^N Y_k h_k \quad h_k = h_k^\circ + \int_{t_0}^t c_{p,k} dt,$$

Species:

$$\rho \vec{u} \cdot \nabla Y_k = \nabla \cdot \mathbf{j}_k + \dot{\omega}_k \quad (k = 1, \dots, K-1), \quad (5.4)$$

where \mathbf{S} is the viscous stress tensor and $\dot{\omega}_k$ is the net production rate of species k . The energy equation is written in terms of total enthalpy, therefore chemical reactions are included in the h term as it comprises the enthalpies of formation. The inter-species diffusion term is not included in the energy equation to reduce computational expense, as its effect is assumed to be negligible.

The detailed model for this problem accounts for all hydrodynamic, chemical and transport phenomena which produce the two-dimensional structure of these flames. The detailed

model has few assumptions and is, therefore, expected to give the most accurate representation of these flames for the assumed boundary conditions.

5.1.1 Discretization and solution procedure

For the detailed simulations, two-dimensional fields for velocity, pressure, temperature and species are solved in the radial and axial directions. This is done utilizing a finite-volume discretization scheme in OPENFOAM . In this scheme, the continuity and momentum equations are formulated in order to use the SIMPLE-R (Semi-Implicit Method for Pressure Linked Equations) algorithm [91] that iteratively marches towards the steady-state solution.

To obtain accurate two-dimensional results, precautions are taken to ensure sufficient grid refinement. A grid refinement procedure is performed that progressively refines the grid in the flame region to a minimum of $10\text{ }\mu\text{m}$ in the streamwise direction. In the radial direction, non-uniform node spacing is employed; cell size is minimized close to the wall to a minimum of $5\text{ }\mu\text{m}$. When doubling the number of cells in both directions, a change below 1% in wall temperature at stabilization is obtained, which demonstrates sufficient grid independence of the solution. Intermediate species profiles are found to be satisfactorily resolved at the refinement level used. Roughly 20,000 cells are typical for the calculations reported here. Sufficient computational power is provided by cluster resources that allow for use of parallel processing capabilities. Each simulation made use of 32 processors for around 500 hours in order to reach the refined converged solution.

In comparison, the volumetric model uses an interfacial heat transfer sub-model which uses 60 fixed radial mesh points concentrated near the channel walls. Roughly 2000 axial mesh points in the sub-model are typical for the calculations reported here. The finest axial meshing occurs in the fast chemistry region at the beginning of the reaction zone to resolve the high temperature gradients and heat release that occur in this region. Nevertheless, the solution of the volumetric model results in computational times which are several orders of magnitude lower than the detailed model.

5.1.2 Transport and chemistry

All transport coefficients and reaction rates are calculated using CANtera [85]. In the above models, the diffusion flux of each species k is given by the mass flux tensor

$$j_k = \rho D_{km} \nabla Y_k, \quad (5.5)$$

where D_{km} are the diffusion coefficients between species k and the remaining mixture. The diffusion coefficients, thermal conductivity, λ , and viscosity, μ , are mixture-averaged values that depend on the local mixture composition and temperature.

This study shall use mixture-averaged transport coefficients, which are simpler than, more strict, multi-component formulations. This leads to significant computational savings, especially in the detailed model. The drawback to using the approximate mixture-averaged formulation is that one is unable to conserve exact mass conservation when solving the species equations. A correction procedure must, therefore, be applied to the models to handle this short-coming. The correction procedure is implemented in different ways in the volumetric and detailed models. In the volumetric model, the correction method applied is that recommended by Coffee and Heimerl [92] where the diffusion coefficient is corrected by a “correction diffusion velocity” in order to satisfy mass continuity. In the detailed model an alternative approach is used where one species is assumed to be present in excess. Rather than solving the species equation for the excess species, its mass fraction is computed simply by subtracting the sum of the remaining species mass fractions from one.

The differences in discretization scheme require that reaction rates also be handled differently in both models. The volumetric model uses a finite-difference scheme, therefore reaction rates are determined at discrete points in the flow directly from the temperature and composition at each point and the rates of progress of the elementary reactions determined by mass-action kinetics. Conversely, the detailed model is discretized into cells of constant volume. The reaction rate should, therefore, be the bulk average rate inside the cells. To accomplish this, the detailed model uses an operator-split method [93] which calculates an average reaction rate based on integration of the ordinary differential equations that define the kinetic system in time over a residence time defined by the flow velocity and volume of each cell.

5.1.3 Reduced kinetics mechanisms

Regardless of the varying degrees of complexity of the models described above, all are formulated to handle multiple species kinetics mechanisms. There are numerous chemical mechanisms available in the literature for hydrocarbon combustion. The most comprehensive are detailed kinetic mechanisms which contain large numbers of species and elementary reactions to capture the important oxidation pathways. An example of which is the GRI-Mechanism [5] which contains 53 species and 323 elementary reactions. These mechanisms are complete; however, the computational cost associated with their solution is presently too high to be of practical use in a detailed, multi-dimensional model. For this reason, simplified reaction mechanisms like that of Westbrook and Dryer [94], which contains 5 species and 1 global reaction, are often used to model this problem [14, 95]. However, such models neglect key reaction pathways by use of a single, global chemical reaction.

In this study, a compromise is made between the comprehensiveness of a detailed mechanism and the relative efficiency of a simplified global reaction. The mechanism chosen is a reduced mechanism for high temperature methane chemistry. This mechanism was developed by Kazakov and Frenklach [96] using the reduction techniques set out in [97]. The mechanism was generated by truncation of the GRI mechanism with the objective of developing the smallest set of elementary reactions which would closely reproduce the main characteristics of high temperature combustion. The mechanism which results contains 19 species and 84 elementary reactions.

The structure of a stoichiometric, adiabatic, planar flame at standard inlet conditions was evaluated to ensure that the reduced mechanism accurately captured the characteristics of a more complete detailed chemical mechanism. A comparison of the solution obtained from the reduced model and one obtained from the latest version of the GRI mechanism [5] shows good agreement in temperature and in the major species profiles in Figure 3.4. Accurate representation of the radicals H, OH and O shown in Figure 3.4 are also important for the present problem. These radicals are the major chain carriers and are largely responsible for setting the burning velocity of the mixture. Of these radicals, the Hydrogen atom is of particular importance. The chain-branching reaction



is dominant in determining chain branching rates in hydrocarbon combustion [1]. H atoms

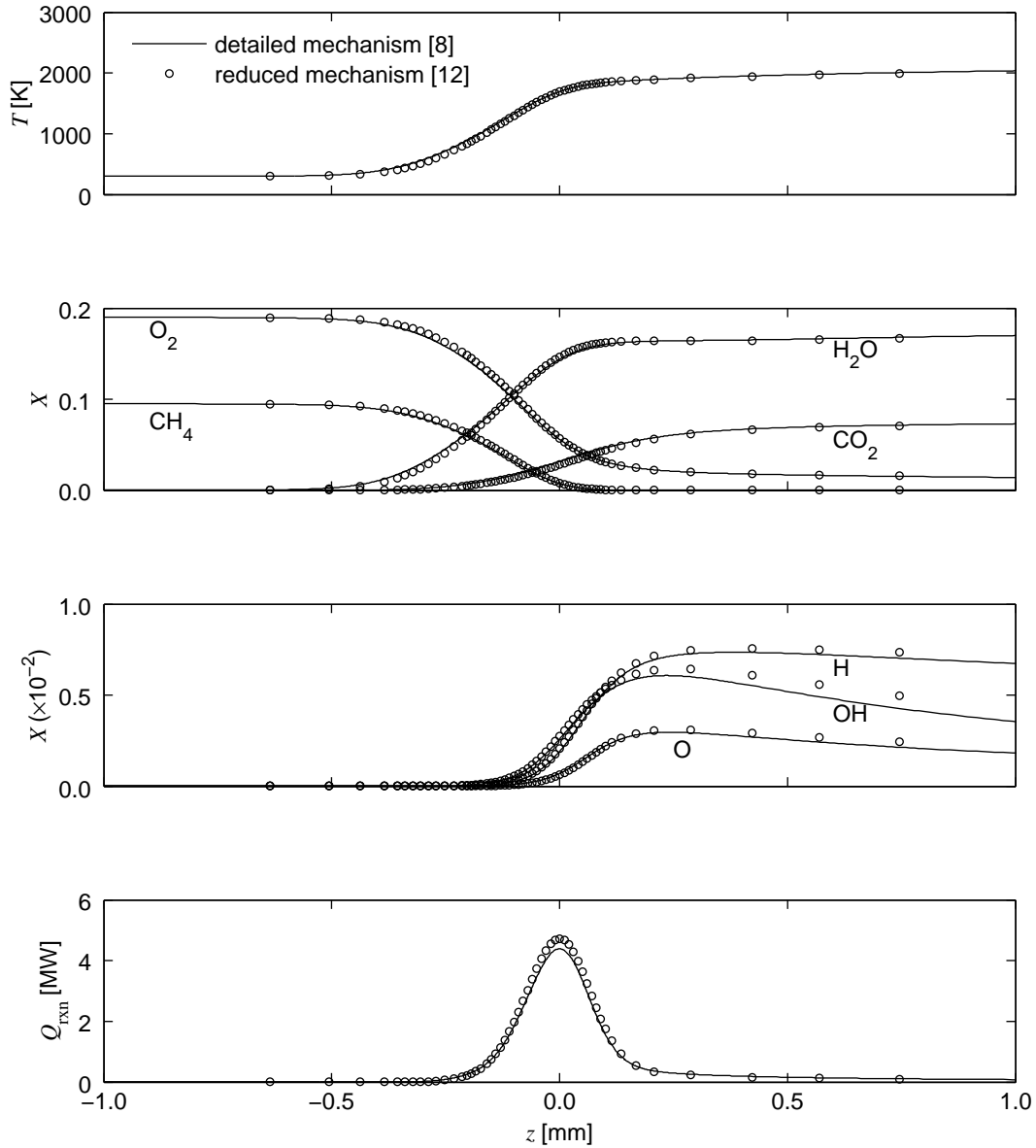


Figure 5.1 Computed structure of a stoichiometric, adiabatic, planar flame at standard inlet conditions, $T_u^\circ = 298$ K, $p^\circ = 1$ atm: temperature, major species, radicals and heat release.

are also the most active diffusive species. This high diffusion rate is also responsible for many important phenomena connected with laminar flames. In Figure 3.4, the reduced model predicts higher concentrations of H inside the reaction zone. This higher concentration tends to give the reduced model a higher peak heat release and, therefore, higher

Table 5.1 Comparison of the simulated global parameters of a stoichiometric adiabatic, planar flame calculated from different kinetics models: Laminar burning velocity, adiabatic flame temperature and thermal thickness. The simplified mechanism uses a global reaction where the forward rate is expressed as $k = AT^n \exp(-E_A/RT)[CH_4]^a[O_2]^b$, where $A = 2.29 \times 10^{13} \text{ (kmol cm}^{-3}\text{)}^{-0.5} \text{ s}^{-1}$, $n = 0$, $a = 0.2$ and $b = 1.3$.

	S_L° [m/s]	T_{af} [K]	δ_T [mm]
Detailed Mechanism - GRI-Mech 3.0 [5]	0.368	2230	0.437
Reduced Mechanism - Kazakov and Frenklach [96]	0.390	2229	0.413
Simplified Mechanism - Westbrook and Dryer [94]	0.387	2324	0.314

burning rates than a detailed mechanism.

Table 5.1 shows a comparison of the global parameters of the adiabatic flame which are predicted by the different classes of mechanisms. The thermal thickness is defined as $\delta_T = (T_{ad} - T_u)/(dT/dx)|_{\max}$. The reduced mechanism shows excellent agreement in predicted adiabatic flame temperature with the detailed mechanism. There is, however, a small 2 cm/s (6%) over-prediction in laminar flame speed and a 0.02 mm (6%) under-prediction in thermal thickness, but these predictions are considerably better than the simplified one-step model which is tuned to have a comparable burning velocity, but leads to much thinner flames than detailed models.

5.2 Summary of data for stabilization position

A summary of flame position data obtained from the simulations versus inlet velocity is shown in Figure 5.2. The stoichiometric flames used in this study are established in the range $0.75 \text{ m/s} \leq S_u \leq 1.00 \text{ m/s}$, and are strongly burning, stable, symmetric flames that have a unique stabilization position within the wall temperature profile. In Figure 5.2, the flame position moves downstream to higher wall temperatures with increasing inlet flow velocity. This increase in wall temperature enhances the burning rate in order to match the larger incoming flow rate.

For the investigated conditions, wall temperatures at the stabilization position are predicted to be on the order of 1280 K by the detailed model. Flames simulated with the volumetric model and the standard Nusselt number assumption predict positions which are consistently upstream of these predictions, with an average deviation of 231 K (18%).

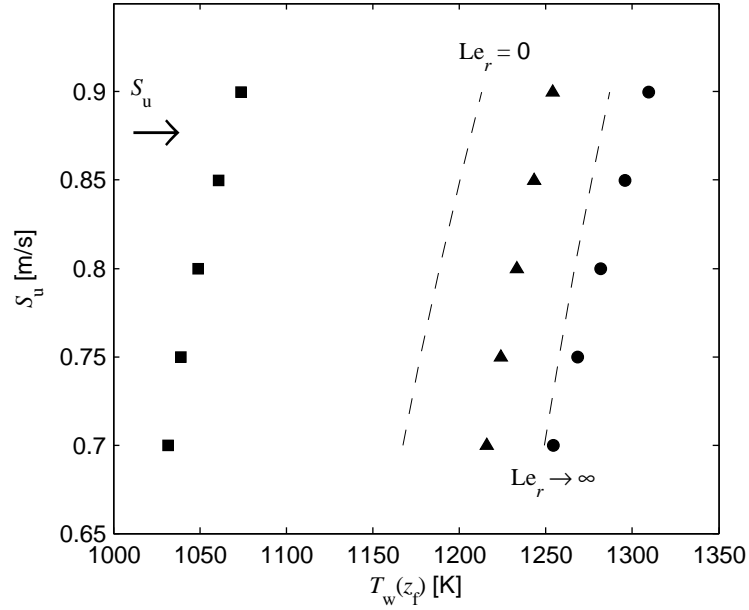


Figure 5.2 Inlet flow velocity, S_u , versus simulated wall temperature at the flame stabilization position, $T(z_f)$, in a $D = 1$ mm tube. Models are the 1-D volumetric model which uses $Nu = 4.0$ (squares) and a solution for interfacial heat transfer which incorporates heat release, $Le = 1.0$ (triangles), and the detailed model (circles).

Volumetric model predictions, with the standard Nusselt number assumption, are also upstream from the $Le = 0.0$ limit of the extended volumetric simulation. This Le limit represents the lowest possible heat loss for a flame when the effects of non-uniform chemical energy release on the flame are considered in an interfacial heat transfer sub-model.

In contrast to the volumetric solution with the standard Nusselt number assumption, inclusion of the heat source term into the interfacial heat transfer sub-model, with $Le = 1.0$, predicts flames which have deviations that are no greater than 55 K (4.2%) in wall temperature throughout the velocity range. These results demonstrate the important role of heat release and heat transfer on flames in small channels.

Figure 5.3 shows the wall temperature profile and typical bulk gas temperature profiles obtained from the computations for a stoichiometric mixture. Bulk temperature is a weighted average of the cross-sectional flow temperature based on mass convection and heat capacity at each radial location [90]. Temperature peaks of three strongly burning flames which stabilize at different locations in the wall temperature profile are apparent in

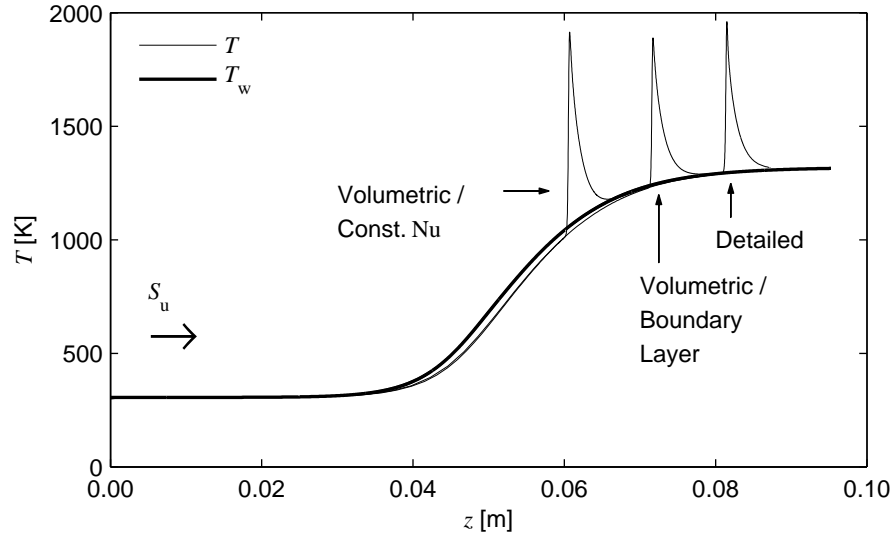


Figure 5.3 Computationally derived flame temperature structure from the volumetric model, with the standard $Nu = 4.0$ assumption, the volumetric model with an interfacial heat transfer sub-model, with heat release, and the detailed model. $\phi = 1.0$, $S_u = 0.85$ m/s.

the figure. The stabilization positions correspond to the locations where the incoming flow rate matches the temperature-dependent burning rate predicted by each model.

5.3 Comparison of the models

An extended volumetric model which uses an interfacial heat transfer sub-model to compute a profile for flame / wall energy transfer offers improved predictions for flame position, which are closer to the detailed simulations. However, deviations in flame position are apparent in the solutions. These deviations are caused by the approximations made within the extended volumetric model. These are investigated by direct comparison of volumetric and detailed solution profiles.

5.3.1 Solution contours

The center plots in Figure 5.4 show a comparison of the axisymmetric structure of the flame from a volumetric model with an interfacial heat transfer sub-model with heat release, verses

the detailed simulation. Solutions are shown as a series of ζ and Q_s contours on the center-left which account for chemistry and heat release, respectively. Temperature contours, $t - T_w$, are shown in the center-right plot. Both models predict a flat structure for the reaction zone, as would be expected at the limit of small Peclet numbers for the burner-stabilized case. Comparison of the ζ profiles with Q_s indicate that most of the chemical activity is in a small region centered around the reaction zone. As heat is released, chemical enthalpy is initially consumed at higher rates near the walls. A rise in gas temperature is coincident with the consumption of reactants and the accompanying heat release. When the source term dissipates, the gas temperature continues to rise near the centerline due to slower ζ consumption in the CO oxidation region of the flame, while the gas temperature cools at the walls due to intense interfacial heat exchange.

It is also useful to gauge how the interfacial heat transfer sub-model profiles, ζ and Q_s , change at the extremes of Lewis number, Le . These have been shown on either side of the comparative plots. In the interfacial heat transfer sub-model, when $Le = 0$ chemical enthalpy does not diffuse in the radial direction; thus, ζ consumed at the walls would not be replenished by diffusion. Chemical enthalpy concentrates at the centerline where the flux of reactants is highest, restricting heat release to the centreline of the channel. Conversely, when $Le \rightarrow \infty$ chemical enthalpy is much more diffusive than heat. Its consumption at the wall would rapidly be replenished by ζ from the centerline. The resulting ζ profiles are radially uniform owing to high diffusivity, that smooths out any gradients, thus producing uniform heat release across the channel.

In the central plots in Figure 5.4, radial profiles from the interfacial heat transfer solution, in the volumetric model, show noticeable deviation from the detailed model for ζ , inside the reaction zone. In the reaction zone of the detailed model, ζ contours are locally radially uniform, which is a similar result from a volumetric model where $Le \rightarrow \infty$. The cause of this deviation is attributed to the relative differences in the rates of slowly moving permanent species and highly diffusive radicals inside the reaction zone, which cannot be captured by a single Lewis number. Furthermore, radially non-uniform axial diffusion cannot be resolved by a interfacial heat transfer sub-model coupled to the volumetric flame model, as axial diffusion in a volumetric formulation is assumed to be uniform along the radial direction.

Chemical enthalpy is converted into heat in a distribution defined by heat release contours. There is good agreement in magnitude and spacial extent between the volumetric

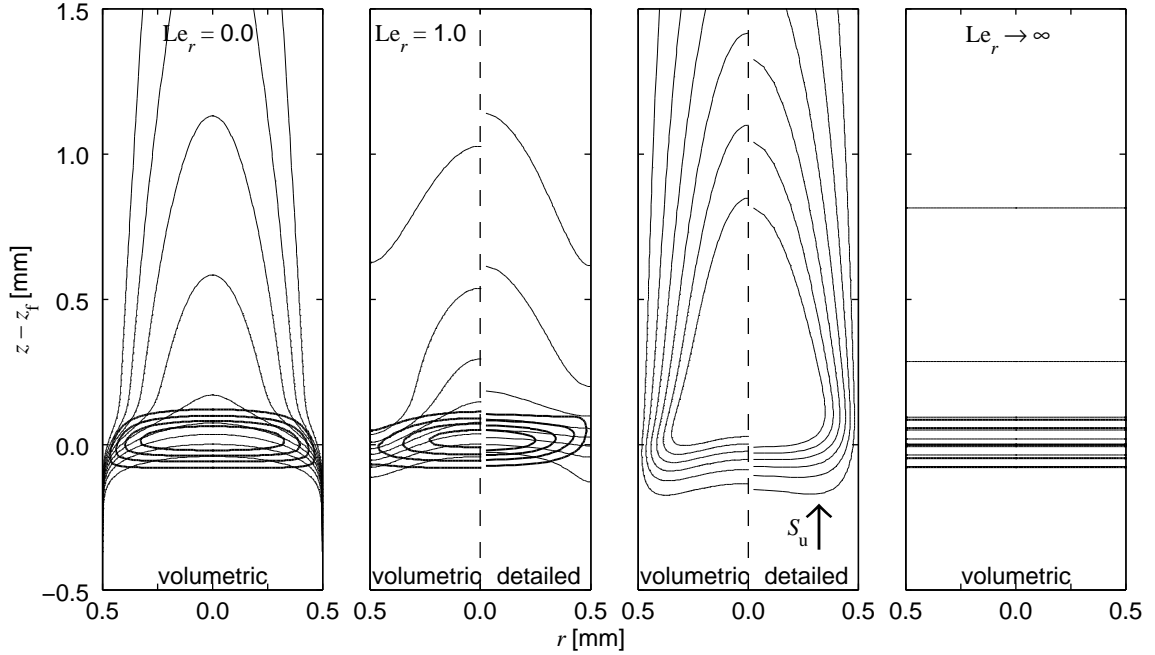


Figure 5.4 The two center plots show a comparison of the contour profiles obtained from a volumetric flame model coupled to an interfacial heat transfer sub-model with heat release ($Le = 1.0$), and the detailed model in a $D = 1$ mm tube: $\phi = 1.0$, $S_u = 0.85$ m/s. The plot shows identical Q_s (thick line) and ζ (thin line) contours in the left plot and the identical gas temperature, $t - T_w$, contours in the right plot. ζ contours are $0.9 \geq \zeta \geq 0.3$, decreasing in intervals of 0.1. Heat release contours are $fQ_{\text{rxn}}/Q_{\text{rxn,peak}} = 0.5, 0.75, 1.0$ and 1.25 . The two plots are flanked by ζ (thin line) and Q_s (thick line) solutions from the volumetric model at the extremes of Lewis number, Le .

and detailed models along the centreline of the channel, for an interfacial heat transfer solution with $Le = 1.0$, but there are local deviations near the walls due to the inability of the interfacial heat transfer formulation to adjust heat release due to local temperature. The temperature contours which result from heat release are, overall, in reasonable agreement in terms of value and spatial extent. The small discrepancies in the temperature predictions of the volumetric model appear to be caused by heating which is too aggressive near the wall in the reaction zone.

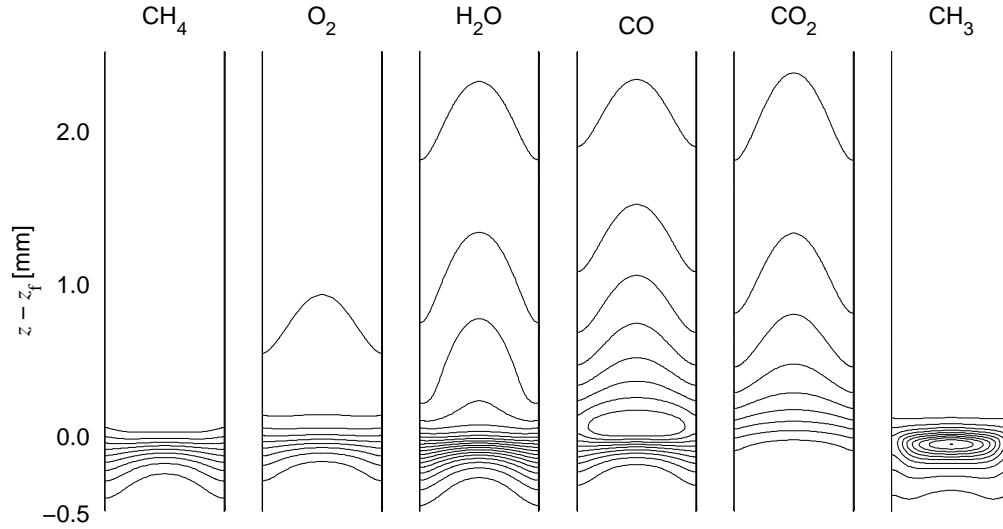


Figure 5.5 2-D, axisymmetric contours of the permanent and intermediate species predicted by the detailed model. $\phi = 1.0$, $S_u = 0.85$ m/s.

5.3.2 Species profiles

The spatial distribution of species and their chemical rates have an important impact on these models. It is essential to ensure that these are accurately predicted in the volumetric model to ensure the correct burning rate. Figure 5.5 shows typical contour plots for a selection of permanent (CH_4 , O_2 , H_2O and CO_2) and intermediate species (CO , CH_3) mole fractions from the detailed model. These profiles have a definite axisymmetric structure which is produced by the non-uniform flow profile and radial diffusivity. The similarity of many of these species to ζ contours in the interfacial heat transfer sub-model is apparent. As was shown by the ζ contours in Figure 5.4, the reactants CH_4 and O_2 which convect into the reaction zone, are initially consumed at the walls. Consumption of these species correspond to production of CH_3 and CO in the primary reaction zone, around $z - z_f = 0$, and the subsequent production of H_2O and CO_2 in the post-flame region.

Volumetric models yield solutions that must be considered as spatially-averaged in the radial direction. Therefore, Figure 5.6 shows a comparison of bulk axial profiles of species centered at the flame from both models. There is excellent agreement for all permanent species which suggests that the volumetric model does a good job predicting overall conversion rates. Figure 5.6 also shows a selection of intermediate species profiles in the immediate vicinity of the flame. These also show good agreement in the trends of these profiles despite

noticeable differences in peak magnitudes of OH, H, and HCO species. Peak in HCO mole fraction as been found to correlate well with the maximum heat release rate in premixed methane-air flames [98]. Hence, the higher HCO peak predicted by the volumetric model is consistent with the higher flame strength deduced from flame position predictions shown in Fig. 5.2.

The concentration of the free radicals O, OH, and H play an important role in decomposition of methane through H abstraction and, thereby, also regulate burning rate. Averaged axial profiles of these species are shown in Figure 5.6, while radial contours from the detailed model are shown in Figure 5.7. In Figure 5.6, there is good agreement in the bulk concentration of O radicals. The concentration of OH is under-predicted by the volumetric model, which is probably due to the difference in temperature at the flame location, as OH production is highly temperature-dependent. Also, the volumetric model over-predicts the concentration of H throughout the flame. This behavior coincides with differences in the radial extent of species contours. In Figure 5.7, regions with increased O and OH mole fraction closely match regions with the highest temperatures; however, in contrast to all other species, H is more uniform across the channel due to its much higher diffusivity. Over-prediction of the concentration of H would produce higher burning rates, which could be one reason why the volumetric model consistently predicts stronger flames. There is also a significant amount of energy stored in these radical species, and the contribution of H to the ζ profile is significant which leads to a more radially-uniform ζ profile in the reaction zone for the detailed model, as shown in Figure 5.4.

5.3.3 Momentum

Flow acceleration is produced inside a flame due to rapid temperature rise and the resultant drop in density. In a small tube, this dilatation is essentially a source of momentum which pushes on the flow in all directions and can cause non-negligible radial velocity components. This phenomenon has been called flow redirection by others [14] and is found to significantly affect burning rate in meso-scale tubes. In this section, the volumetric assumption of a parabolic axial profile and an insignificant radial component in the limit of small Pe is evaluated by comparison with solutions from the detailed simulation.

Figure 5.8 shows deviations in axial and radial mass flux ($\Delta\rho u$ and $\Delta\rho v$) from the assumed axial parabolic profile at axial locations $z - z_f$ in the vicinity of the flame. The

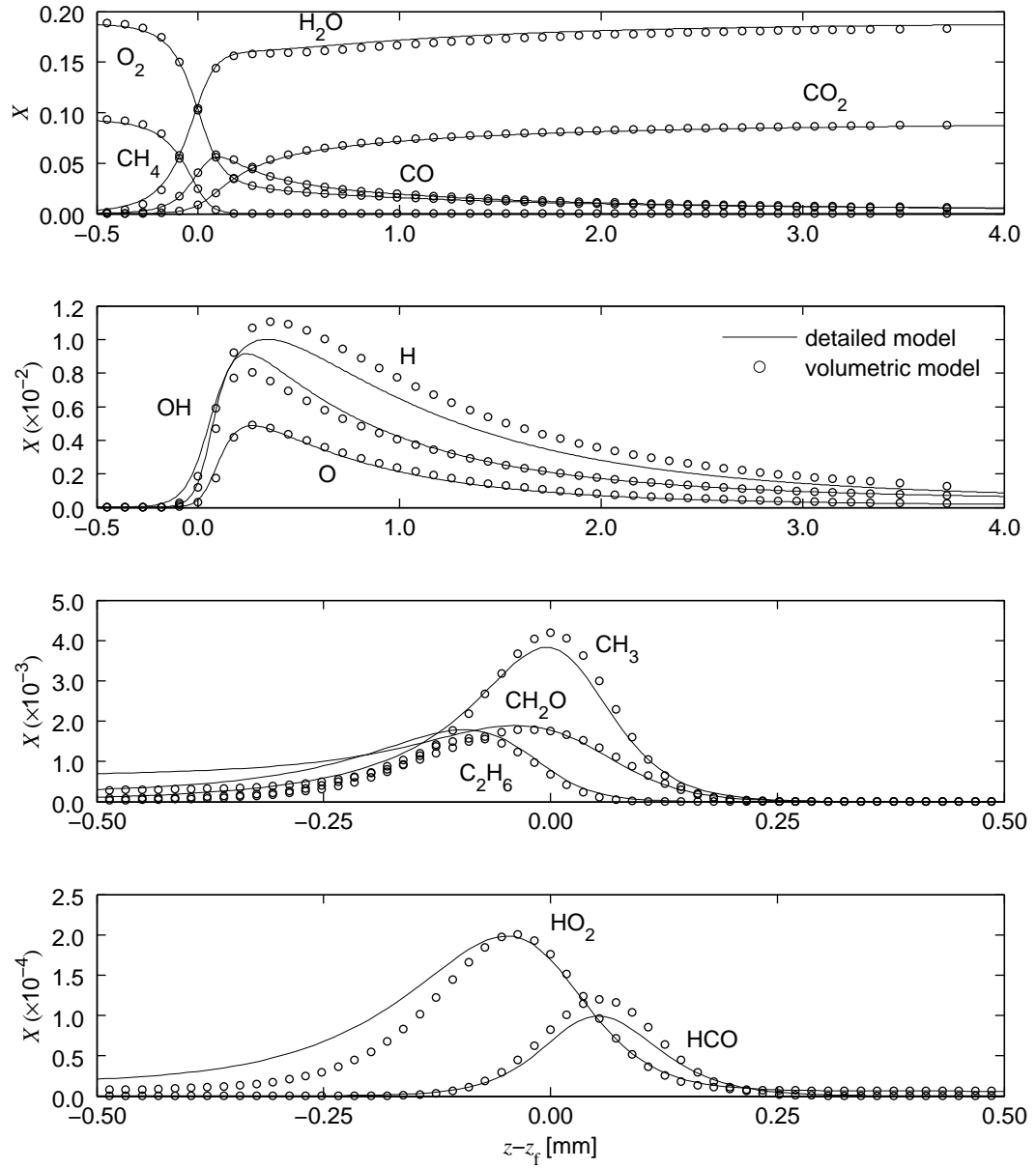


Figure 5.6 Comparison of bulk species profiles: Permanent species, radicals and intermediate species. Operating conditions as in Figure 5.5.

definitions for these deviations are

$$\begin{aligned}\Delta\rho u &= \frac{\rho(t)u - 2\rho(T)U(1 - (r/r_w)^2)}{\rho_u S_u}, \\ \Delta\rho v &= \frac{\rho(t)v - 0}{\rho_u S_u},\end{aligned}\tag{5.7}$$

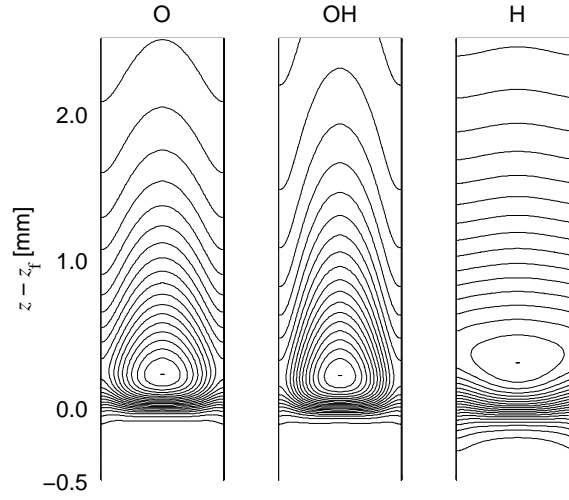


Figure 5.7 2-D, axisymmetric contours of free radicals from the detailed model. Operating conditions as in Figure 5.5.

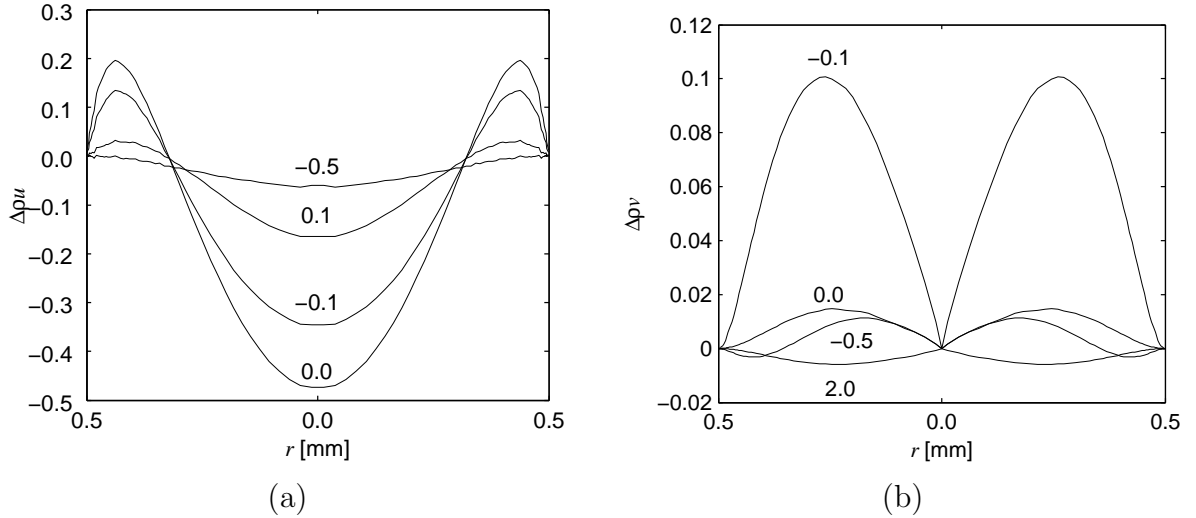


Figure 5.8 Deviations in axial (a) and radial (b) mass flow from an assumed parabolic profile. Profiles are extracted from the detailed model at axial locations $z - z_f = -0.5, -0.1, 0.0, 0.1, 2.0$ mm. $\phi = 1.0$, $S_u = 0.85$ m/s.

where they are normalized by the average axial mass flow ($\rho_u S_u$), which is a conserved quantity in both models. Density in these relations are specified either at the local temperature, $t(z, r)$, or as an average at the bulk temperature, $T(z)$, and composition.

The flow profile does deviate from parabolic in a small zone in the vicinity of the flame

($-0.5 \text{ mm} < z - z_f < 2.0 \text{ mm}$). When this occurs axial mass flow drops at the centreline and is higher at the wall due to transition to a top-hat profile. However, a top-hat profile is not achieved before the flow begins to develop back to the parabolic profile. The axial variation of mass flow is strong enough to produce a radial outflow which is approximately 1/10th of the average mass flux at the flame location. Radial convection of reactants towards the wall broadens heat release in a similar way to the enhanced diffusion of the $\text{Le} \rightarrow \infty$ case as it pushes reactant species away from the center-line where the reaction is concentrated.

5.4 Conclusions

Alternative models for combustion stabilized by a wall temperature profile, in the limit of small channels, have been compared for the full range of inlet flow velocities which produce strongly burning flames. The detailed formulation has few assumptions and is expected to be valid for the assumed boundary conditions, but is computationally costly to implement. Contrastingly, the simpler, volumetric formulation has much lower computational cost, but lower accuracy than the detailed model. These findings are summarized in Gauthier et al. [99]. However, volumetric model predictions have been shown to be significantly improved by incorporating an interfacial heat transfer sub-model so that interfacial heat transfer can be modeled in a consistent manner.

In the volumetric formulation, the interfacial heat transfer sub-model can replace common assumptions for Nusselt number with a model built around the conservation of chemical enthalpy and its conversion to sensible heat. This allows for the generation of a radial temperature distribution that captures the effect of chemical heat release on interfacial heat transfer with the wall. It is found that establishing a spatial profile for temperature based on radially varying chemical heat release is important for these strongly burning flames. However, use of a kinetics mechanism with multiple species and a detailed, multi-dimensional model have revealed additional details of the reaction zone structure that are not captured in the volumetric formulations. H atom diffusivity plays a particularly important role in dictating the spatial energy profile and in setting the burning rate in hydrocarbon flames. Near-wall quenching due to radial temperature variation and flow redirection are also observed to be significant processes. Due to the elliptic nature of the problem, it is not possible to definitively state the relative contribution of each of these

effects on the small deviations observed between the volumetric and detailed models. In addition, the trade-off to add these phenomena is that increasing levels of accuracy come with a steep increase in computational time needed to solve the flame.

The volumetric model with the interfacial heat transfer sub-model results in predictions which are within 55 K (4.2%) of the detailed model at the flame stabilization position. This improved level of accuracy suggests that the volumetric model is acceptable for the design of heat-recirculating burners. This would result in a large savings in computational cost compared to detailed models with acceptable accuracies, provided that the conditions investigated approach a flat flame structure.

Chapter 6

Propagating flame in a participating channel

In this chapter, premixed flames propagating in small heated channels which participate in energy transfer are investigated with a volumetric model to study the combined effects of heat loss and heat recirculation. This is a rich problem which exhibits a wide range of behaviours. The chapter will touch on two classes of this problem. The first are for flame propagation close to a wall that does not participate in energy transfer. This is the classic problem of heat loss and quenching in an isothermal channel [6]. Such channels allow for propagation until extinction occurs at the quenching distance. The second class is for flames propagating in participating channels, to create filtration waves. Such flames exhibit multiple regimes that depend on the propagation speed and on the strength of flame / wall coupling by interfacial heat transfer [2].

Like all volumetric models discussed in previous chapters, the present model is also expected to be valid only when used to predict the burning rates of nearly flat flames. This is found for sufficiently small tube dimensions. However, for nearly quenched propagating flames, thermal quenching and radical recombination could produce a 2-D structure [14]. These effects shall be neglected in the present discussion. For hot channel walls, homogeneous chemical reactions are assumed to overcome the effect of radical removal at the wall, so that the flame becomes resistant to quenching [3].

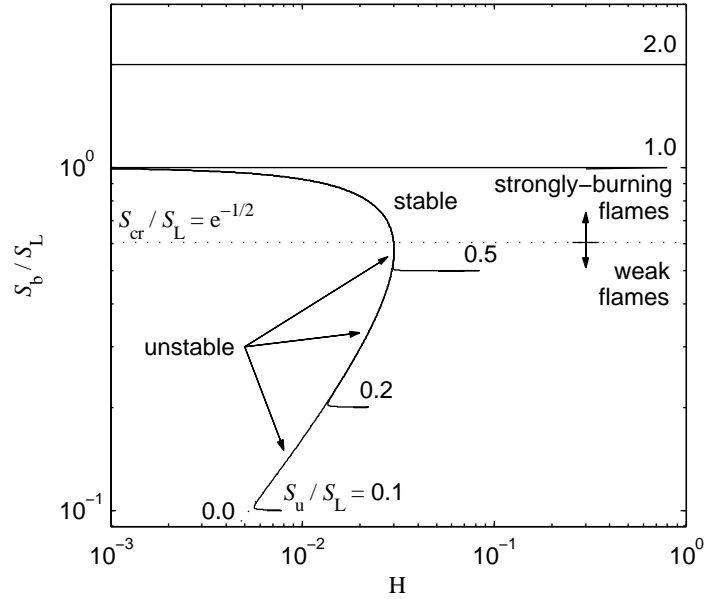


Figure 6.1 Dependence of normalized burning rate, S_b/S_L , on dimensionless interfacial heat transfer coefficient, H , for multiple forced inlet flow speeds, S_u/S_L in a participating channel. $S_L = 0.18$ m/s, $T_u = 300$ K, $T_{af} = 1800$ K, $Nu = 4$, $Le = 0.9$, $\beta \rightarrow \infty$.

6.1 Solution from an asymptotic model

It is, again, best to begin the discussion with results from an asymptotic model. Such models make significant compromises when it comes to the physics (see, for example, Chapter 2), but they are essential tools which permit greater understanding of a system's behaviour and, thus, act as a guide for advanced efforts. Ju and Xu [2] have derived an asymptotic model for flame propagation in a small channel. The model consists of normalized, 1-D governing equations for the gas and solid phase and are solved in the limit of the flame sheet assumption, $\beta \rightarrow \infty$, with constant properties and a simplified chemistry scheme which consists only of the deficient reactant specie. Full details of the derivation are given in Appendix A.2.

Figure 6.1 shows the resulting burning velocity of the propagating flame as a function of the bulk interfacial heat transfer coefficient, H . In the asymptotic model, H is defined as (see Equation A.8):

$$H = \frac{4Nu}{Pe^2}, \quad (6.1)$$

therefore, for this simple model, an increase in H could physically be interpreted as reduction in tube diameter. For the case of no inlet flow velocity, $S_u = 0$, the normalized burning velocity, S_b/S_L , exists on stable and unstable branches which meet at a bifurcation point, at a critical speed S_{cr} . This behaviour is similar to the classical solution of Spalding [6] for a freely propagating flame through an isothermal channel (see Appendix A.2). Therefore, the bifurcation at S_{cr} represents the normal extinction point for fast-propagating, strongly-burning flames. However, when an inlet flow velocity is applied, an additional bifurcation occurs initially at small burning velocities, and the solution forms an additional stable branch which is located at different burning rates. When the new branch is located below the S_{cr} , the solution forms weakly-burning flames with very low burning rates. Flames on this new branch are also slowly-propagating flames, in that their burning velocity is approximately equal to the inlet flow velocity. When the branch lies above S_{cr} , the combustion wave is slowly-propagating, but appear as strongly-burning flames.

It is, therefore, a general property of this system that, for any value of the bulk interfacial heat transfer coefficient, H , at least two stable solutions are possible for the propagating flame. These solutions are: fast-propagating strongly-burning flames, slowly-propagating strongly-burning flames, and, finally, slowly-propagating weakly-burning flames. In addition, it is also possible, for the condition $S_u < S_L$, to have solutions exist at the same instant for fast and slowly-propagating flames for the same imposed inlet flow velocity, S_u , and heat transfer rate, H .

This chapter focuses on the strongly burning flames found for $S_b > S_{cr}$. For such flames, heat release is strong enough to affect interfacial heat transfer and burning rate. It is also known from Chapter 3 that such flames are not well described by a bulk interfacial heat transfer rate. For such a case, it is more instructive to treat inlet flow velocity as the independent variable, rather than a prescribed interfacial heat transfer rate. Figure 6.2 shows the dependence of burning velocity on inlet flow velocity. The asymptotic model obtains two solutions for fast and slowly-propagating flames. The flames are, again, distinguished by flame propagation speed. Fast flames are produced when the inlet velocity is small compared to the flame propagation speed. For small channels, the propagation speed is slower than the laminar flame speed due to intense heat loss to the channel walls. For zero inlet velocity, this regime mirrors the standard quenching behaviour where burning velocity drops exponentially with channel dimension [6], in Figure A.2. Slow flames are formed on the second branch when the inlet velocity is large, which slows the propagation

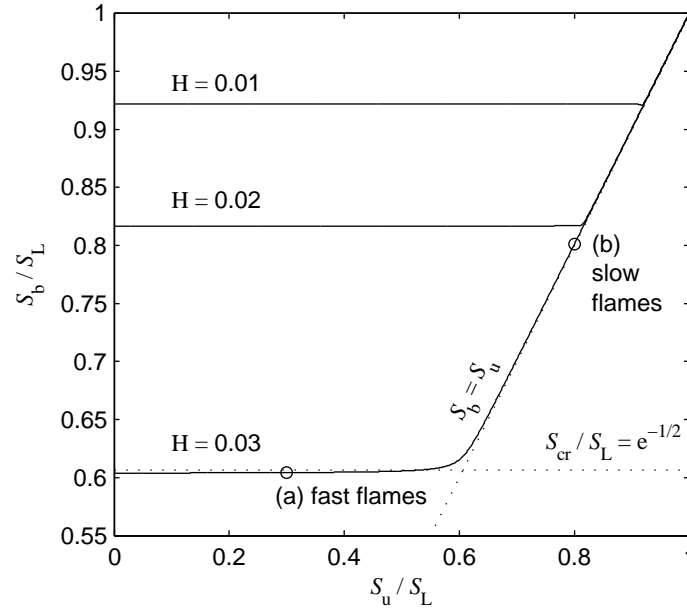


Figure 6.2 Dependence of flame burning rate, S_b/S_L , on inlet flow speed, S_u/S_L for fixed dimensionless interfacial heat transfer coefficients, H for strongly-burning flames. Flame profiles (a) and (b) for fast and slowly-propagating flames are shown in Appendix A.2. $S_L = 0.18$ m/s, $T_u = 300$ K, $T_{af} = 1800$ K, $Nu = 4$, $Le = 0.9$, $\beta \rightarrow \infty$.

speed. For this condition, heat lost via interfacial heat transfer is recirculated through the channel walls to preheat the reactants. The effect has been shown to scale strongly with wall thermal conductivity [67]. This produces a concentration of enthalpy in the reaction zone and higher burning rates [16].

6.2 Volumetric model with detailed chemistry

Burning rate is strongly influenced by chemistry. Therefore, a predictive model should have the ability to utilize detailed chemical reaction mechanisms. Typical combustion processes are modeled by mechanisms which contain many tens of species and hundreds of elementary reactions. While multi-dimensional simulations with detailed chemistry are an obvious choice for accuracy [14, 29, 45], these are, currently, not a practical option due to the enormous computational cost associated with such formulations.

In this chapter, an alternative 1-D volumetrically-averaged formulation is developed

for the coupled equations, to obtain the bulk chemical and temperature profiles for the flame and channel wall. Again, an interfacial heat transfer sub-model is used to generate realistic solutions for flame / wall heat transfer. The sub-model is similar to Chapter 2, but is extended to include momentum effects to capture changes in the convective profile exhibited by fast-propagating flames [14].

6.2.1 1-D, volumetric flame

As in previous chapters, the flame structure is treated in a volumetric sense. Radial variation is, therefore, neglected and is replaced by volumetrically-averaged, bulk parameters (capital letters) at each axial location. This assumption is generally not a problem for small tube diameters as species profiles predicted by multi-dimensional simulations have been shown to be, overall, quite close to those predicted by the volumetric approach (see Chapter 5). The relevant volumetric energy and species equations for the gas and the wall are:

Gas energy:

$$\rho c_p (U - U_f) \frac{dT}{dz} = \frac{d}{dz} \left(\lambda \frac{dT}{dz} \right) - \sum_k c_{p,k} j_{k,z} \frac{dT}{dz} - \sum_k \dot{\omega}_k h_k W_k - Q_w(z), \quad (6.2)$$

Gas species:

$$\rho (U - U_f) \frac{dY_k}{dz} = - \frac{dj_{k,z}}{dz} + \dot{\omega}_k W_k, \quad (6.3)$$

Wall energy:

$$-\rho_w c_w S_f \frac{dT_w}{dz} = \lambda_w \frac{d^2 T_w}{dz^2} - 2\epsilon\sigma(T_\infty^4 - T_w^4) \left(\frac{r_\infty^2}{r_\infty^2 - r_w^2} \right) + Q_w(z) \left(\frac{r_w^2}{r_\infty^2 - r_w^2} \right) \quad (6.4)$$

where the equations are formulated for a flame-fixed reference frame. The boundary conditions are:

$$\begin{aligned} z \rightarrow -\infty : \quad U &= S_u - S_f, \quad T = T_u = T_\infty, \quad Y_k = Y_{k,u}, \\ z \rightarrow \infty : \quad \frac{dU}{dz} &= 0, \quad \frac{dT}{dz} = 0, \quad \frac{dY_k}{dz} = 0. \end{aligned} \quad (6.5)$$

These equations are similar to those used elsewhere [2, 52], and in previous chapters.

Thermal energy is partitioned between two energy equations, for the wall and the gas, which are written to accommodate chemical reactions from any number of k gas species equations. In the wall, the effect of conduction along the flow axis and radiation loss to the environment, proportional to the surface emissivity, ϵ , is also considered. Gas thermodynamic properties, mixture-averaged transport, and reaction kinetics are calculated with CANTERA [85], while the solid properties ρ_w , c_w , and λ_w are held constant.

The problem is to find the propagation speed, S_f , that satisfies the conservation equations and boundary conditions. The equations are solved in a similar way to Chapter 2, with well-established algorithms [79].

6.2.2 Interfacial heat transfer sub-model

To close the problem, a sub-model for Q_w is needed to account for interfacial heat transfer. Here, an interfacial heat transfer sub-model is formulated to directly solve for the thermal and momentum effects that result from heat release, using standard boundary layer approximations [79] (also, see Appendix D). Before solving the channel boundary layer equations, it is convenient to rewrite the equations with a von Mises transformation. With the following expression for the stream function, ψ :

$$\rho u r = \frac{\partial \psi}{\partial r} \quad \text{and} \quad \rho v r = -\frac{\partial \psi}{\partial z}, \quad (6.6)$$

the boundary layer equations are:

Continuity:

$$0 = \frac{\partial r^2}{\partial \psi} - \frac{2}{\rho u}, \quad (6.7)$$

Momentum:

$$\rho u \frac{\partial u}{\partial z} + \frac{\partial p}{\partial z} = \mu \rho u \frac{\partial}{\partial \psi} \left(\rho u r^2 \frac{\partial u}{\partial \psi} \right), \quad 0 = \frac{\partial p}{\partial \psi}, \quad (6.8)$$

Gas energy (sensible heat):

$$\rho u c_p \frac{\partial t}{\partial z} = \lambda \rho u \frac{\partial}{\partial \psi} \left(\rho u r^2 \frac{\partial t}{\partial \psi} \right) - q_s(r, z), \quad (6.9)$$

Species (chemical enthalpy):

$$u \frac{\partial \zeta}{\partial z} = \text{Le} \frac{\lambda}{\rho c_p} \rho u \frac{\partial}{\partial \psi} \left(\rho u r^2 \frac{\partial \zeta}{\partial \psi} \right) - \dot{\zeta}_s(r, z). \quad (6.10)$$

Such equations capture the substantial cross-stream diffusion and convective transport which would be present in this developing flow. The above formulation for the channel boundary layer is similar to Chapter 2, except for the addition of flow redirection [14] using a momentum equation. Similar notation for variables in Chapter 2 are used here, however, an overview of some aspects is warranted.

In Equations 6.9 and 6.10, there are source terms, q_s and $\dot{\zeta}_s$, which prescribe the heat release profile and account for diffusion in the axial direction. q_s is made equal to the heat of reaction, conduction and interspecies diffusion:

$$q_s(r, z) = f(r, z) Q_{\text{rxn}}(z) + Q_{\text{th}}(z), \quad (6.11)$$

to maintain equivalent axial gas energy equations between Equation 6.9 and 6.2, where the variable $f(r, z)$ is a convolution to give bulk heat release radial dependence. Furthermore, the profile for $\dot{\zeta}_s$ is equivalent one to which results from Equations 2.25, 2.26 and 2.30.

In Equation 6.10, a progress variable, $\zeta(r, z)$, is defined such that there is equivalence between its rate of consumption, $\dot{\zeta}$, and the rate at which energy is injected into the interfacial heat transfer sub-model due to heat release (see Section 2.3.3). This variable functions as an indicator of the local fraction of chemical enthalpy stored in the reactants. The radial distribution of the heat source, $f(r, z)$, is assumed to be proportional to the distribution of chemical enthalpy inside the channel following the Law of Mass Action.

Equation 6.10 describes the evolution of the progress variable as a conservation equation for chemical enthalpy, where ζ is allowed to convect, diffuse, and be consumed in the domain. The rate at which ζ is allowed to diffuse is controlled by a Lewis number for chemical enthalpy, Le , which is defined here as the ratio of the diffusivity of ζ to the bulk thermal diffusivity. Energy is contained in several chemical species that diffuse at different rates; therefore, there is no way to know the best value of Le in advance of the modeling effort. It is, therefore, customary to present results over the range $0 \leq \text{Le} \rightarrow \infty$ to bracket all possible solutions for this model.

The boundary conditions for Equations 6.7–6.10 are:

$$\begin{aligned} \psi = 0 : \quad r = 0, \quad \frac{\partial u}{\partial \psi} = 0, \quad \frac{\partial t}{\partial \psi} = 0, \quad \frac{\partial \zeta}{\partial \psi} = 0, \\ \psi = \psi_w : \quad r = r_w, \quad u = S_f, \quad t = T_w, \quad \frac{\partial \zeta}{\partial \psi} = 0, \end{aligned} \quad (6.12)$$

where the extra radial boundary condition is used as an implicit boundary condition for pressure and ψ_w is set to satisfy the total mass flow entering the channel. Profiles for axial velocity, temperature, ζ , and pressure are set in accordance to the conditions in the flame for each iteration as initial conditions, but r cannot be specified independently and is obtained by integrating Equation 6.7.

The resulting equations are stiff, parabolic, differential-algebraic equations (DAEs). More information relating to the formulation of these equations is given in Appendix D. The Implicit Differential-Algebraic solver (IDA) in the SUNDIALS package [100] is used following the procedure in [101, 102]. Temperature profiles obtained from this solution are used to generate a volumetric interfacial heat transfer profile given by:

$$Q_w = -\frac{2\lambda}{r_w} \frac{\partial t}{\partial r} \bigg|_{r_w}, \quad (6.13)$$

which is then used to obtain the 1-D solution for the flame propagating in the channel.

6.3 Representative solution profiles

6.3.1 Bulk profiles

Figures 6.3 and 6.4 show typical profiles for fast- and slowly-propagating flames, respectively. These solutions are for stoichiometric flames with the same ambient temperature and, thus, the same laminar flame speed, S_L . Fast flames have propagation speeds that are larger than the inlet velocity ($S_f > S_u$). These propagation speeds are too fast for the flame to have a local effect on the wall temperature; therefore, the burning rate of these flames is governed principally by heat release from gas chemistry and heat loss to the wall. Initially, gas temperature increases rapidly due to chemical heat release, but temperature decreases in the burned region due to intense interfacial heat transfer.

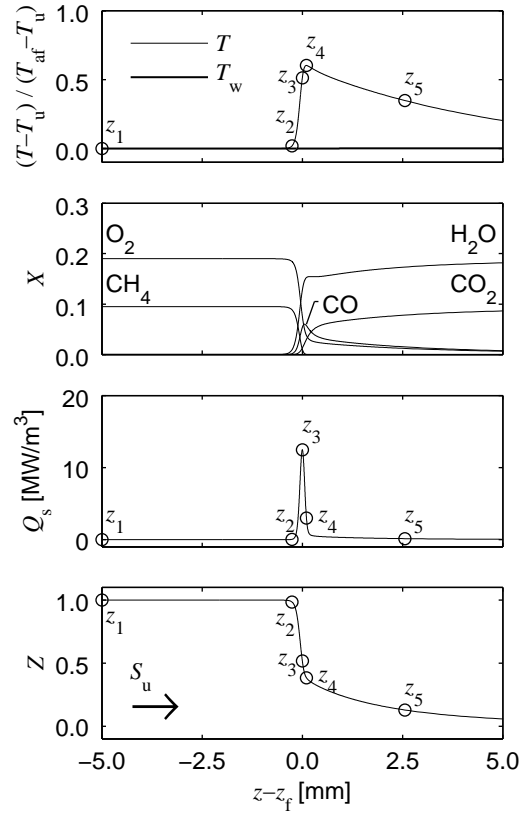


Figure 6.3 Typical profiles for a fast-propagating methane / air flame ($\phi = 1.0$) near a quartz channel wall, $S_u = 1.5$ m/s, $T_\infty = 1100$ K, $r_w = 1.0$ mm, $r_\infty = 1.5$ mm.

A further increase in inlet flow velocity results in slowly-propagating flames. Such flames have propagation speeds that are significantly (several orders of magnitude) slower than fast flames, which leads to a significant temperature increase in the channel wall and higher peak temperatures. In these slow flames, a portion of the heat lost from the burned gases is recirculated upstream of the flame to preheat the reactants, resulting in higher wall temperatures than the gas in the preheat zone. Interfacial heat transfer causes strong thermal coupling between the gas and the wall, which causes higher reactivity and burning rates.

Core to the volumetric model are predictions for bulk species profiles determined from the elliptical Equations 6.2–6.4. The model has the ability to accept detailed kinetics models of various sizes and for a wide variety of gaseous fuels without difficulty, but for

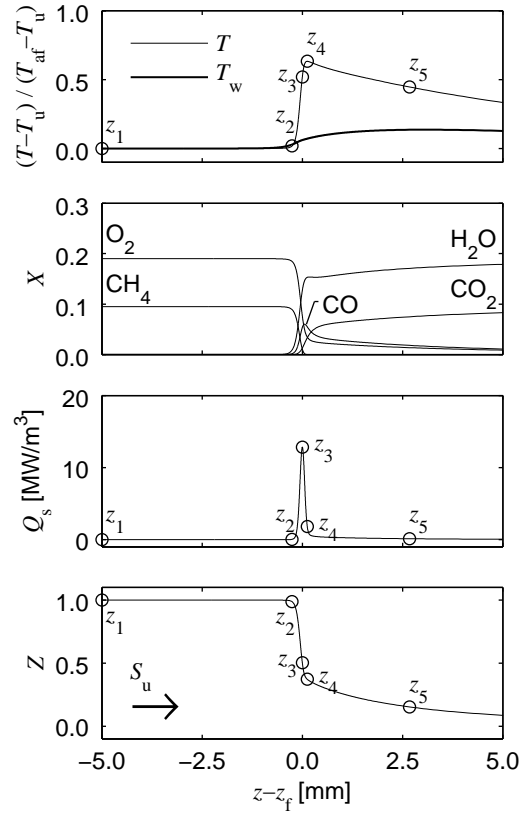


Figure 6.4 Typical profiles for a slowly-propagating flame, $S_u = 3.5$ m/s. Solution parameters as in Figure 6.3.

illustrative purposes, a methane / air flame is used. The mechanism chosen is a reduced mechanism for high temperature methane chemistry, developed by Kazakov and Frenklach [96] using reduction techniques in [97]. The resulting mechanism has 19 species and 84 elementary reactions. Figures 6.3 and 6.4 show typical profiles for the permanent species. Consumption of these reactants coincides with a depletion of chemical enthalpy and an increase in heat release, shown by the bulk q_s and ζ (Z) profiles.

6.3.2 Radial profiles

Gas / wall interfacial heat transfer predictions are the result of a 2-D thermal boundary layer. Typical profiles for the axial velocity component and temperature are shown in Figure 6.5 at locations z_1 – z_5 , marked in Figures 6.3 and 6.4.

Inlet boundary conditions are shown at z_1 . This location is sufficiently far upstream from

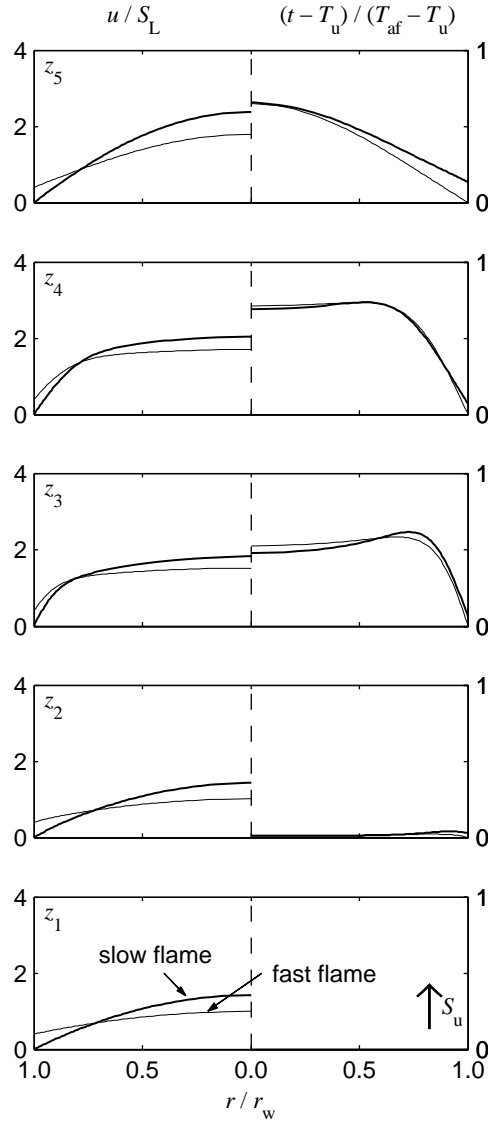


Figure 6.5 Axial velocity, u/S_L , and temperature, $(t - T_\infty)/(T_{af} - T_\infty)$, profiles for a fast (thin line) and slowly-propagating (thick line) flames. Solution parameters as in Figures 6.3 and 6.4.

the flame so that the gas temperature is uniform and equal to the wall temperature. The inlet velocity profile is a sum of two velocity components due to the flame-fixed reference frame used in the calculation. The first component, which is apparent in the fast flame, is a uniform velocity equal to the finite propagation speed of the flame in the channel, S_f . The second component is a parabolic profile from the fully-developed inlet flow, which is

dominant in the slow flame due to the high incoming velocity and slow propagation speed.

Upstream of the flame, at z_2 , heat release and conduction have a small influence on the temperature profile. In the slow flame, the largest influence at this location is from the higher temperature wall which injects additional heat into the gas due to heat recirculation. There is a rapid rise in gas temperature, at z_3 , due to heat release. This location, at the peak of heat release, also corresponds to the maximum temperature gradient at the wall and the highest heat loss along the axis of the channel. Heat release also results in larger gas velocities that are more spatially uniform than the initial fully-developed profile. The gas temperature continues to increase further downstream up to z_4 , at the location of peak bulk gas temperature, but this location presents a lower wall temperature gradient than at z_3 . Finally, in the cool-off region, at z_5 , the temperature and velocity profiles have nearly become fully-developed. Chemical energy release is not significant at this location; therefore, these profiles are governed by diffusion of temperature and momentum in a non-reacting channel boundary layer.

6.4 Global solution results

6.4.1 Isothermal walls

The simplest case is for a freely-propagating flame in a constant temperature, isothermal wall. This case is valid for a flame near a thick wall with high volumetric heat capacity, and is the standard definition for the flame quenching problem [6]. Figure 6.6 shows the dependency of burning velocity, $S_b = S_u - S_f$, on tube diameter for a flame passing through a hot channel. This case has no inlet velocity, therefore burning velocity is equal to flame propagation speed, $S_b = -S_f$.

Figure 6.6 shows a comparison of three models. The first is a detailed multi-dimensional model. A detailed model can be used with reasonable computational cost for this case, with constant-temperature walls. The detailed model used here accounts for all hydrodynamic, chemical, and transport phenomena which produce the two-dimensional structure of these flames. The formulation of the detailed model and its numerical procedure are described in Chapter 5, and elsewhere [14]. This model has few assumptions and is, therefore, expected to give accurate data for this case. The other models are 1-D volumetric models which use different assumptions for interfacial heat transfer. The first uses the standard assumption of

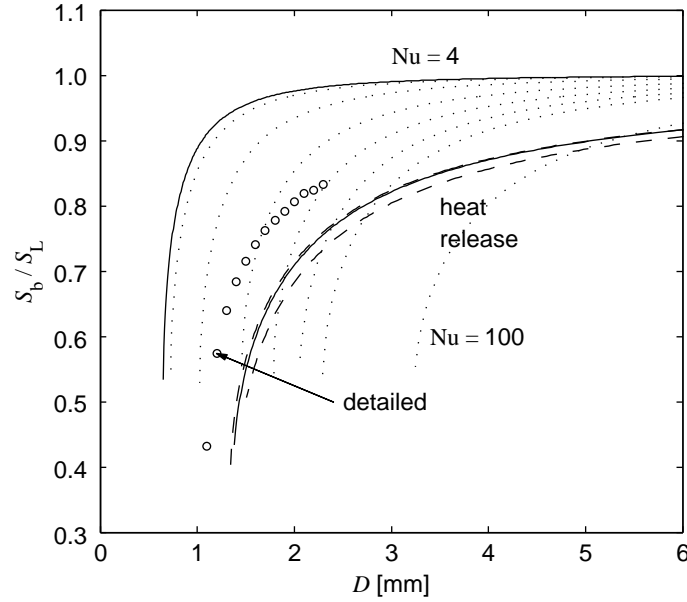


Figure 6.6 Simulated quenching curves for stoichiometric freely-propagating flames in an isothermal channel, $T_w = 1100$ K. Constant Nu curves, from left to right, are Nu = 4, 5, 10, 20, 30, 40, 50, 100.

Newton's Law of Cooling and a constant Nusselt number, Nu. There is, however, difficulty in choosing an appropriate Nusselt number. A common choice (see, for example [2, 46], among others) is to use $Nu \approx 4$, for fully-developed, non-reacting flow profiles, but trends are similar for an extensive range of Nusselt numbers. The second volumetric model uses the updated interfacial heat transfer formulation, built around the effects of chemical heat release and flow momentum, described in this dissertation. Three curves are shown, for $Le = 1.0$ and for the limits $0 \leq Le \rightarrow \infty$ (dashed lines to the left and right of the $Le = 1.0$ line, respectively), which represent the maximum range of uncertainty caused by the relatively uncertain Lewis number in this model.

Burning velocity drops exponentially with decreasing tube diameter until the flame quenches when the rate of heat release from chemical reactions is overcome by heat loss to the wall. This quenching diameter is lower than at standard conditions due to the higher temperature wall. Data points for the detailed model do not follow trends predicted by a single Nusselt number, but lie across these lines shifting from one to another with tube diameter. Contrastingly, the updated volumetric model gives improved predictions over the range of tube diameters.

There is, however, an $\sim 20\%$ discrepancy in the final flame quenching diameter, compared to the detailed model. This discrepancy is likely due to the effect of 2-D near-wall flame-extinction, which is neglected in the interfacial heat transfer sub-model. In the interfacial heat transfer sub-model, heat release is linked to the local value of chemical enthalpy, as in the Law of Mass Action, but also uses the *bulk* gas temperature. Therefore, heat release predictions are higher at the wall, than in the detailed simulations, which is why volumetric predictions have higher heat loss and yield slightly weaker flames.

It should also be noted that predictions for extinction from all models in Figure 6.6 have critical values for burning velocity which lie below the standard value of S_{cr} found in the asymptotic formulation (see Figure 6.1). For cold walls ($T_w = 300$ K), it is confirmed that the extinction limits for all models are found at the recognized value of $S_{cr} = 0.6S_L$. However, as shown in Figure 6.6, the extinction point for all models shift to lower burning velocities in hot walls and, while there is good agreement in the trends between the detailed and updated volumetric models, the standard volumetric model predicts higher burning rates. Therefore, for heated channels, the bifurcation point shifts to lower burning rates. This is an interesting behaviour which requires further investigation in future studies.

6.4.2 Participating walls

The solution changes considerably when the channel wall is made thin enough to participate in axial energy transfer. Figure 6.7 shows solution curves for the burning velocity of flames when subjected to an imposed inlet velocity, S_u . The axes in this figure are not mutually exclusive, in that a large component of the mass burned is from the inlet flow. Data in this figure are for propagating flames and, therefore, there is a line along $S_b = S_u$ to delineate between different propagation solutions. A solution on this line represents a stationary flame in this problem, $S_f = 0$. Alternatively, data to the left of this line represents flames propagating counter to the flow direction, whereas a solution to the right of the line represents concurrent propagation.

In Figure 6.7, as the inlet flow velocity increases, the solution transitions from fast to slowly-propagating flames near the line $S_b = S_u$. A further increase in inlet flow velocity leads to computational solutions where the domain of convergence shrinks till both steady-state and transient solvers fail at the maximum value of S_b/S_L . Therefore, the upper limit of S_b/S_L in Figure 6.7 represents the upper extinction limit for the propagating

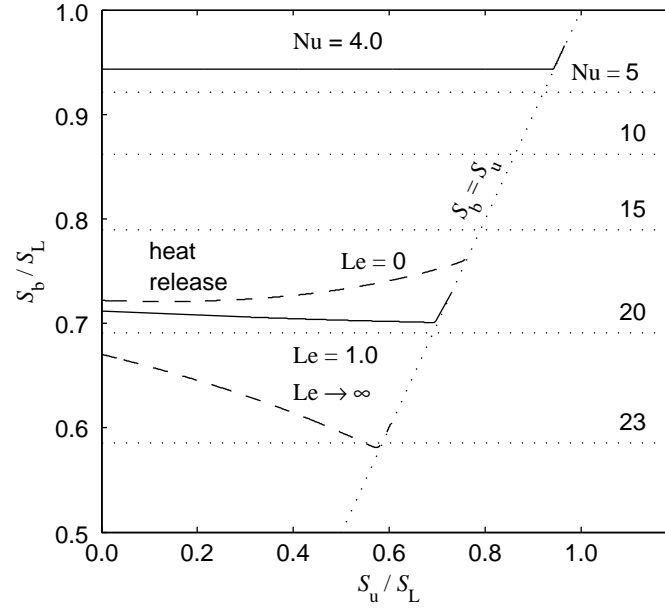


Figure 6.7 Burning velocities for stoichiometric propagating flames opposed by inlet mass flow. Solution parameters as in Figure 6.3.

flame, as documented in Zamashchikov and Minaev [103]. In the tubular geometry, the extinction burning velocity can be greater or less than S_L , depending on diameter, wall properties and heat loss conditions, but is typically sub-adiabatic for methane [49, 50, 104]. Nevertheless, the limit can be extended if wall thermal conductivity is enhanced, as discussed in Section 6.4.3, or further increased by insulation of the tube wall to prevent heat loss.

Figure 6.7 also compares solutions from the two volumetric models. Unfortunately, flame / wall coupling increases computational effort significantly making the detailed model impractical at present. Again, the common choice of $Nu \approx 4$ is used, but other values are given for reference in the figure. For $Nu = 4$ and zero inlet velocity, burning velocity is 94% of the laminar flame speed. Solutions that lie in the fast regime are, initially, insensitive to increasing inlet velocity; however, when $S_b \simeq S_u$, there is a drastic change in the solution trajectory due to transition to the slow regime. For slowly-propagating flames, heat recirculation through the channel wall counteracts increased mass flow. Therefore, slow flames have smaller propagation speeds, but are strongly burning flames due to larger burning rates.

The extended volumetric model shows two notable improvements over solutions that use

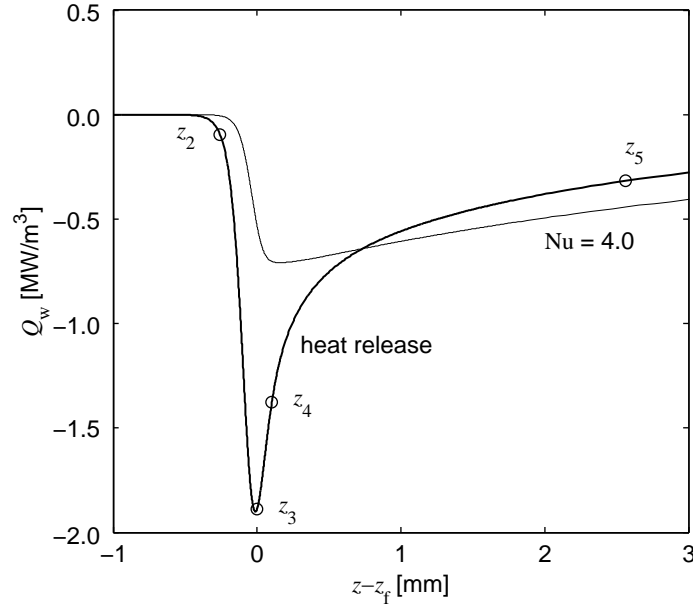


Figure 6.8 Interfacial heat transfer profiles for volumetric models. Solution parameters as in Figure 6.3.

a constant Nusselt number. First, the improved formulation replaces an assumed Nusselt number with a physical model describing the diffusion of heat and mass in the reaction zone. Solutions that include the effects of heat release have burning velocities which are smaller than what is predicted by typical constant-Nu models. Reduced burning velocities result from higher predicted heat loss due to non-linear heat release and steep temperature gradients. The second improvement lies in the inclusion of radial flow effects into the problem. A constant-Nu model assumes fully-developed profiles, which is not correct in the reaction zone. Solutions from the extended formulation show burning velocities which vary non-monotonically with inlet flow velocity. This is especially true for fast flames with $Le > 1.0$ where burning velocity first decreases with increasing inlet flow rate, which is a behaviour consistent with experiments [2].

Q_w terms derived from the different boundary layer assumptions are shown in Figure 6.8. In this figure, a negative value indicates heat loss from the gas to the wall. Again, it is seen that the location of peak heat loss is at the location of peak heat release, and not at the location of peak temperature, as required by the constant-Nu case. The rate of energy loss in the reaction zone is much larger when heat release and its effects are accounted for in the interfacial heat transfer sub-model (see z_3). For this fast flame, chemical composition

Table 6.1 Wall thermal properties.

Material	ρ_w [kg/m ³]	c_w [J/kg·K]	λ_w [W/m·K]	ϵ
SiO ₂	2650	750	1.1	0.93
Al ₂ O ₃	3690	880	18	0.45
SiC	3100	750	120	0.83

and inlet flow rate are the same for both cases, therefore improved prediction of local heat loss in the reaction zone results in reduced values for burning rate, as seen in Figure 6.7.

6.4.3 Influence of wall properties

The mode most relevant to micro-combustors is the slowly-propagating flame. In this regime, flames are coupled to a thermal wave in the channel wall via interfacial heat transfer. The thermal wave allows for heat recirculation from the burned gas to preheat the reactants, increasing flame burning rate and enhancing flammability limits [2]. It is, therefore, expected that wall thermal properties influence the burning rate of slowly-propagating flames. Figure 6.9 shows solution curves for burning rate versus inlet velocity for the slowly-propagating regime. To show the influence of wall thermal properties, solution curves have been calculated for three common high-temperature ceramic wall materials: quartz (SiO₂), alumina (Al₂O₃), and silicon carbide (SiC). The thermal properties of these materials are summarized in Table 6.1.

In Figure 6.9, there is a smooth transition from the fast to slow regimes of propagation. For slowly-propagating flames, solution curves lie close to, but to the left of, the $S_b = S_u$ line indicating small counter-current propagation speeds. Solution curves for the three wall materials show similar trends in burning rate; however, there are slight differences in the solution curves that depend on the wall material. This is especially noticeable for silicon carbide which shows transition to the slow flame regime at smaller inlet flow velocities. The ordering of these transitions correspond to differences in thermal conductivities of the materials, thus underlying the effect of heat recirculation on burning rate. However, all solutions follow the $S_b = S_u$ line at higher inlet velocities. For these boundary conditions, it is the rate at which heat is transferred to and from the wall that controls burning velocity and the enhanced model presented here is able to more accurately capture this effect than previous 1-D models.

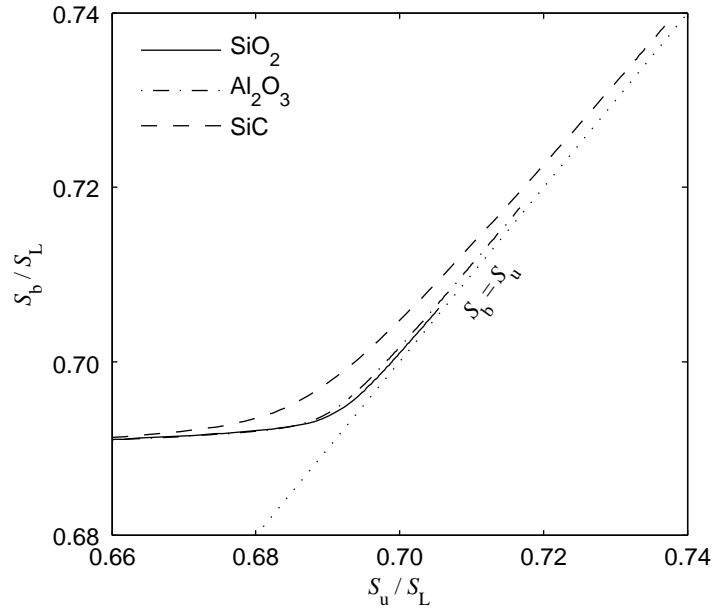


Figure 6.9 slowly-propagating regime for quartz, alumina, and silicon carbide walls. Solution parameters as in Figure 6.3.

6.5 Conclusion

An interfacial heat transfer sub-model has been developed to extend the standard 1-D volumetric model for a flame propagating in a small, heated channel. The extended model provides improved predictions for flame behaviour over the standard method of using Newton's Law of Cooling and an assumed Nusselt number.

Only a fully elliptic, multi-dimensional model can account for all phenomena, but such a model is currently impractical due to the high computational costs associated with flame-wall coupling in this problem. Comparisons of the present model with a simpler detailed simulation, with an isothermal wall, show similar trends for flame extinction. These trends are more reasonable than those from the standard volumetric formulation, but the flames are weaker than those found in detailed simulations.

Results from the extended model confirm the existence of regimes for fast and slow flame propagation. High temperature kinetics and heat loss govern the burning rate of fast-propagating flames. These flames also exhibit a non-monotonic variation of burning rate with inlet mass flow rate, which is consistent with experimental measurements. At higher inlet flow velocities, there is a transition to slowly-propagating flames. In this regime, heat

recirculation via flame-wall coupling sustains elevated mass burning rates. Wall thermal properties are also found to influence the transition point from fast- to slowly-propagating flames.

The interfacial heat transfer sub-model is based on boundary layer assumptions and does not treat the heat transfer problem as being fully-developed. Instead, the channel boundary layer equations are solved taking into account radial temperature and velocity variations due to a volumetric heat release profile. Typical values for Nusselt number are found to under-predict heat loss for this case due to strong chemical reactions which produce steep local temperature gradients. The location of peak heat loss is also found to correspond to peak heat release and not to the location of peak temperature, as would be predicted by Newton's Law of Cooling.

Chapter 7

Conclusions

This dissertation investigates the role of interfacial heat transfer on confined flames in small heated channels, when the channel dimension is on the order of the flame thickness. The case is found in a diverse array of new burner technologies which rely on interfacial energy exchange for flame propagation and stabilization. There are many phenomena at play in such systems, but the small size of the channel makes interfacial heat transfer the dominant phenomenon, governing the characteristics of flames at these scales.

7.1 Synopsis

In the first chapters, the simple case of stabilized combustion in a non-participating, heated channel is investigated to study the interfacial heat transfer phenomenon without the effects of heat recirculation. Standard volumetric models, which are extensively used in literature, are found to inadequately predict the structure of strongly-burning flames. Instead, an alternative model formulation is proposed, where the detailed 1-D structure of the flame is determined by coupling elliptical volumetric equations, for axial diffusion and detailed chemistry, to an interfacial heat transfer sub-model. The new approach allows for improved predictions by accounting for the development of two-dimensional, channel boundary layer and its response to chemical heat release. This is accomplished by tracking the spatial consumption of chemical enthalpy to determine an approximate temperature distribution inside the channel.

An improved apparatus and methodology allows model predictions to be validated with

experimentally-derived stable flat flames at variable inlet flow rates. Predictions from the extended volumetric model are found to give acceptable agreement for stoichiometric flames, when accounting for the uncertainty in the measurements. These results demonstrate the significant role of heat loss in governing the stabilization position and structure of strongly burning, confined flames.

The extended volumetric model is also compared to detailed multi-dimensional simulations, which consider the full elliptical equations for mass, momentum, energy and species transport. This model has few assumptions and is, therefore, expected to give accurate predictions for flame structure. Detailed simulations of strongly burning stoichiometric flames are found to be flat for the small tube dimension, at the flow rates used, which is a key assumption in the volumetric formulation. There is also good agreement in bulk temperature and species profiles, and much lower inaccuracies in flame stabilization position, resulting in significantly improved predictions over the standard 1-D model.

Discrepancies are also noted in the volumetric simulations. A discrepancy is found in 2-D heat release profiles. In the interfacial heat transfer sub-model, heat release is linked to the local value of chemical enthalpy, as in the Law of Mass Action, but not to local temperature variation. Heat release is, therefore, found to be higher at the wall than in the detailed simulations, where local quenching of chemical reactions lessens heat loss and reduces wall temperature gradients. Another discrepancy is related to the 2-D distribution of the species: H, OH and O, which are important radicals for setting burning rate. In the interfacial heat transfer sub-model, all species are modeled by a single profile for chemical enthalpy, thus assuming that all species diffuse at, more or less, similar rates. However, this is not the case for the H radical, whose enhanced diffusivity, compared to other species, result in a distribution which is quite uniform across the channel. A third discrepancy relates to the 2-D velocity profile and flow-redirection, which is found to be non-negligible. This effect is not included in the interfacial heat transfer sub-model. Such discrepancies result in reduced accuracy of the volumetric model and an overall 5% deviation in flame position, between volumetric and detailed simulations. However, while a multi-dimensional formulation is assumed to be superior, the improved accuracy that the detailed model produces is offset by the enormous computational expense of such simulations.

In the final chapter, focus then turns to the case of flame propagation and extinction in a participating channel. This allows for the effects of flame / wall heat loss and heat recirculation to be studied – to determine their combined influence on flame burning rate.

To model propagating flames, the interfacial heat transfer sub-model is revised to account for flow re-direction and the various inlet boundary conditions which occur for propagating flames. The model is evaluated with stoichiometric flames over a range of channel inlet flow velocities and confirms the existence of regimes for fast and slow flame propagation over a range of burning velocities. Flame burning velocities are also found to have non-monotonic variation due to the combined influences of heat release and the flow profile. Detailed simulations are also compared to volumetric predictions for flame propagation in isothermal channels. Improved predictions for flame extinction are, once again, found from the extended volumetric formulation.

7.2 Contributions

An important scientific contribution of this dissertation is in discerning the influence of interfacial heat transfer on flames in small channels, so that its effects can be incorporated into simple volumetric models. Interfacial heat transfer is primarily responsible for energy lost from the flame. The phenomenon, thus, has a direct influence on stabilization and burning rate. It is found that heat loss inside the reaction zone has a strong influence. In this zone, heat loss is directly coupled to the rate and magnitude of heat released from combustion reactions, and on the spatial distribution of chemical enthalpy inside the channel. This phenomenon acts to produce a local thermal discontinuity in the development of the channel boundary layer and results in steep wall temperature gradients. Heat loss in a reaction zone is, therefore, an important phenomenon which cannot be ignored for strongly burning flames.

A secondary role of interfacial heat transfer is to assist in heat recirculation. In such a process, gas / wall coupling in the preheat zone acts as a passage for heat lost in the reaction zone to be deposited upstream of the flame to preheat reactants. Such a process enhances burning rate, but the effect is only significant for slowly propagating flames.

It has also been shown that models which neglect the effects of chemical energy release, in the reaction zone, significantly underestimate heat loss from flames in small channels. For confined flames, chemical reactivity does more than just set the laminar flame speed, and the burning rate. The spacial extent of chemical reactions is also important for determining the structure of a confined flame. Therefore, accurate predictions of flame / wall heat loss must come from model formulations which use a comprehensive list of species, and

elementary chemical reactions.

Volumetric models which use Newton's Law of Cooling are incapable of capturing local thermal discontinuities caused by heat release. This is due to the assumption of a thermally fully-developed flow in Nusselt number correlations. It is also found that the Nusselt number is orders of magnitude higher than is often assumed within the reaction zone. Asymptotic models which utilize a thin flame sheet assumption, and neglect interfacial heat transfer, when deriving jump conditions are also susceptible to such problems.

The interfacial heat transfer sub-model replaces common assumptions for Nusselt number with a computationally efficient model built around the effects of chemical energy release. Only a fully 2-D, elliptic formulation can determine the exact topography of heat release for this case, but the results show that significantly improved agreement over standard approaches can be achieved using the simplified model developed in this dissertation.

The interfacial heat transfer sub-model is for tubular channels, but can be easily reformulated, using appropriate coordinate transformations, for other geometries. This would allow its use in practical settings that require a 2-D geometry, using either planar or radial coordinates. The extended model can also accommodate detailed chemical models of different hydrocarbon fuels, different wall materials, and is relatively inexpensive to implement, compared with detailed simulations. Such a model would be useful for the optimization of novel heat-recirculating burners, which is not practical with present multi-dimensional formulations.

Appendix A

Analytical models

A.1 Stationary flame in a steady wall temperature profile

The analytical solution of Maruta et al. [46] is derived for a flame in a tubular duct stabilized within a steady, monotonically increasing wall temperature profile, $T_w(z)$, to obtain solutions for the approximate flame behaviour (stabilization position, temperature, burning velocities, stable/unstable behaviour, etc.) over a wide parameter range. The steady, energy and species equations for the gas are:

$$-\rho c_p S_u \frac{dT}{dz} = \lambda \frac{d^2 T}{dz^2} - \frac{4h_V}{D}(T - T_w) + Q_c \dot{\omega}, \quad (\text{A.1})$$

$$-\rho S_u \frac{dY}{dz} = \mathcal{D} \frac{d^2 Y}{dz^2} - \dot{\omega}, \quad (\text{A.2})$$

where constant properties are assumed. The combustible mixture is made sufficiently lean such that it is the concentration of fuel (the deficient reactant) which governs the problem. Y and Q_c are, therefore, the mass fraction and the heat of combustion of the fuel. Consumption of the fuel is by a single component one-step chemical reaction which is assumed to have sufficiently high activation energy such that it occurs in a thin reaction layer. The reaction rate is, therefore, governed by

$$\dot{\omega} = \rho Y_u B \exp\left(\frac{-E_A}{2Rt_f}\right) \delta(z - z_f), \quad (\text{A.3})$$

which follows the formulation of Buckmaster and Ludford [105] with a delta function with the units [1/m].

Equations A.1–A.3 are re-scaled into dimensionless forms using the following substitutions:

$$\xi = z \frac{\rho c_p S_L}{\lambda} = \frac{z}{\delta_f}, \quad (\text{A.4})$$

$$\mathcal{S}_u = \frac{S_u}{S_L}, \quad (\text{A.5})$$

$$\theta = \frac{T - T_u}{T_{af} - T_u}, \quad (\text{A.6})$$

$$\text{Le} = \frac{\lambda}{\rho c_p \mathcal{D}}, \quad (\text{A.7})$$

$$\text{H} = 4 \left(\frac{hD}{\lambda} \right) \left(\frac{\lambda}{\rho c_p S_L D} \right)^2 = \frac{4\text{Nu}}{\text{Pe}^2}, \quad (\text{A.8})$$

$$\beta = -\frac{E_A}{R} \frac{T_{af}^2}{(T_{af} - T_u)}, \quad (\text{A.9})$$

$$T_{af} - T_u = \frac{Q_c Y_u}{c_p}, \quad (\text{A.10})$$

$$S_L = B \exp \left(\frac{-E_A}{2RT_{af}} \right). \quad (\text{A.11})$$

The conservation equations become

$$\frac{d^2\theta}{d\xi^2} + \mathcal{S}_u \frac{d\theta}{d\xi} - \text{H}(\theta - \theta_w) = -\exp \left[-\frac{\beta}{2} \frac{(1 - \theta_f)}{1 - a(1 - \theta_f)} \right] \delta(\xi - \xi_f), \quad (\text{A.12})$$

$$\frac{1}{\text{Le}} \frac{d^2 Y}{d\xi^2} + \mathcal{S}_u \frac{dY}{d\xi} = \exp \left[-\frac{\beta}{2} \frac{(1 - \theta_f)}{1 - a(1 - \theta_f)} \right] \delta(\xi - \xi_f), \quad (\text{A.13})$$

where $a = (T_{af} - T_u)/T_{af}$ is a reduced reaction enthalpy and β is the Zel'dovich number. The boundary conditions are

$$\begin{aligned} \xi \rightarrow +\infty : \quad & \theta = 0, \quad Y = 1; \\ \xi \rightarrow -\infty : \quad & \theta = \theta_w(-\infty) = \Theta, \quad Y = 0. \end{aligned} \quad (\text{A.14})$$

An asymptotic solution shall be sought for these coupled equations. In such an analysis,

the domain is split into three zones: an upstream zone, a downstream zone and zone which contains the reaction layer. The zones are then solved independently and then asymptotically matched to obtain the full solution. Here, a solution in the limit of β being very large is explored. In this limit, the leading-order solution has a reaction layer which can be treated as an unstructured reaction sheet. Inside the reaction layer, diffusion and reaction terms dominate:

$$\frac{d^2\theta}{d\xi^2} = -\exp\left[-\frac{\beta}{2} \frac{(1-\theta_f)}{1-a(1-\theta_f)}\right] \delta(\xi - \xi_f), \quad (\text{A.15})$$

$$\frac{1}{\text{Le}} \frac{d^2Y}{d\xi^2} = \exp\left[-\frac{\beta}{2} \frac{(1-\theta_f)}{1-a(1-\theta_f)}\right] \delta(\xi - \xi_f). \quad (\text{A.16})$$

In order to obtain profiles outside the reaction layer, new boundary conditions must be specified on either side of the reaction layer. These conditions are that the temperature inside to the zone is equal to the flame temperature, which is to be solved later, and that the fuel is fully consumed at the downstream boundary of the layer:

$$\xi = \xi_f : \quad \theta^+ = \theta^- = \theta_f, \quad Y^- = 0, \quad (\text{A.17})$$

where the plus and minus signs represent upstream and downstream boundaries of the reaction layer, respectively. The slope of the outside solutions must also be specified at these boundaries. These are set by the jump conditions. Adding Equations A.15 and A.16 and integrating across the reaction sheet gives the first jump condition:

$$\left. \frac{d\theta}{d\xi} \right|_{\xi_f}^- - \left. \frac{d\theta}{d\xi} \right|_{\xi_f}^+ = \frac{1}{\text{Le}} \left. \frac{dY}{d\xi} \right|_{\xi_f}^+, \quad (\text{A.18})$$

where $dY/d\xi|_{\xi_f}^- \equiv 0$ has been used. The second jump condition comes directly from Equation A.16 by integrating on the domain $\infty < \xi \leq \xi_f^-$ and utilizing the boundary conditions in A.15, which gives

$$\left. \frac{1}{\text{Le}} \frac{dY}{d\xi} \right|_{\xi_f}^- = \exp\left[-\frac{\beta}{2} \frac{(1-\theta_f)}{1-a(1-\theta_f)}\right]. \quad (\text{A.19})$$

This condition ensures the important physical result that the rate of consumption of the

fuel should be equal to the reaction rate inside the sheet.

Outside the reaction zone, the reaction rate is exponentially small. Equations A.12–A.13 take the form

$$\frac{d^2\theta}{d\xi^2} + \mathcal{S}_u \frac{d\theta}{d\xi} - H(\theta - \theta_w) = 0, \quad (\text{A.20})$$

$$\frac{1}{\text{Le}} \frac{d^2Y}{d\xi^2} + \mathcal{S}_u \frac{dY}{d\xi} = 0. \quad (\text{A.21})$$

Equation A.21 can be solved immediately for the species profile with the boundary conditions A.15 and A.17. The species profile is:

$$Y = \begin{cases} 0 & \text{if } \xi \leq \xi_f^- \\ 1 - \exp[-\text{Le}\mathcal{S}_u(\xi - \xi_f)] & \text{if } \xi > \xi_f^- \end{cases} \quad (\text{A.22})$$

Obtaining the temperature profiles from Equation A.20 is a straight forward, but lengthy, procedure. This equation is a linear, nonhomogeneous second order equation with two eigenvalues:

$$\begin{aligned} \lambda_1 &= -\frac{\mathcal{S}_u}{2} - \sqrt{\frac{\mathcal{S}_u^2}{4} + H} < 0 \\ \lambda_2 &= -\frac{\mathcal{S}_u}{2} + \sqrt{\frac{\mathcal{S}_u^2}{4} + H} > 0 \end{aligned}, \quad (\text{A.23})$$

and with the boundary conditions A.15 and A.17, and some algebraic manipulation, the temperature profiles are obtained:

$$\theta = \begin{cases} \Theta - \Theta \exp[\lambda_2(\xi - \xi_f)] + \theta_f \exp[\lambda_2(\xi - \xi_f)] \\ - \frac{\exp[\lambda_2(\xi - \xi_f)] \exp(\lambda_1 \xi_f)}{\lambda_2 - \lambda_1} \int_{-\infty}^{\xi_f} \exp(-\lambda_1 \xi) H \theta_w d\xi \\ + \frac{\exp(\lambda_1 \xi)}{\lambda_2 - \lambda_1} \int_{-\infty}^{\xi} \exp(-\lambda_1 \xi) H \theta_w d\xi & \text{if } \xi < \xi_f \\ \theta_f \exp[\lambda_1(\xi - \xi_f)] \\ - \frac{\exp[\lambda_1(\xi - \xi_f)] \exp(\lambda_2 \xi_f)}{\lambda_2 - \lambda_1} \int_{\xi_f}^{\infty} \exp(-\lambda_2 \xi) H \theta_w d\xi \\ + \frac{\exp(\lambda_2 \xi)}{\lambda_2 - \lambda_1} \int_{\xi}^{\infty} \exp(-\lambda_2 \xi) H \theta_w d\xi & \text{if } \xi > \xi_f \end{cases} \quad (\text{A.24})$$

The flame temperature, θ_f , is needed for the above profiles. This is the eigenvalue of the problem. The expressions needed to obtain θ_f are obtained from the jump conditions A.18–A.19. Substitution of the species and temperature profiles into the jump conditions gives

an algebraic system of equations for the flame temperature at the flame position, ξ_f , within the wall profile

$$\mathcal{S}_u = \exp \left[-\frac{\beta}{2} \frac{(1 - \theta_f)}{1 - a(1 - \theta_f)} \right], \quad (\text{A.25})$$

$$\mathcal{S}_u - \theta_f(\lambda_2 - \lambda_1) = \exp(\lambda_2 \xi_f) \int_{\xi_f}^{\infty} \exp(-\lambda_2 \xi) H \theta_w d\xi - \exp(\lambda_1 \xi_f) \int_{-\infty}^{\xi_f} \exp(-\lambda_1 \xi) H \theta_w d\xi. \quad (\text{A.26})$$

Equations A.25 and A.26 are implicit equations which can be solved with a continuation strategy, stepping in \mathcal{S}_u . In this scheme, the flame position, ξ_f , is obtained by applying a root finding procedure to Equation A.26. The resulting solution profiles are shown in Figure 2.1.

A.2 Propagating flame in a participating channel

The analytical solution of Ju and Xu [2] is derived for a flame propagating inside a channel. This problem is solved allowing for energy transport in the inert channel walls. The conservation equations are

$$\rho c_p \frac{dT}{dt} + \rho c_p S_u \frac{dT}{dz} = \lambda \frac{d^2 T}{dz^2} - \frac{4h_V}{D}(T - T_w) + Q_c \omega, \quad (\text{A.27})$$

$$\rho c_p \frac{dY}{dt} + \rho S_u \frac{dY}{dz} = \mathcal{D} \frac{d^2 Y}{dz^2} - \omega, \quad (\text{A.28})$$

$$\rho_w c_w \frac{dT_w}{dt} = \lambda_w \frac{d^2 T_w}{dz^2} + \frac{4h_V}{D}(T - T_w), \quad (\text{A.29})$$

where reaction rate is given by Equation A.3 and constant properties are assumed. It is also assumed that the flame propagates at a constant propagation speed, S_f , which is defined to have a velocity in opposite direction to the flow, $-S_f$. A galilean transformation is used to convert the equation into a fixed flame coordinate system. In this frame of reference the transient terms are transformed into a convective terms. For example, for gas temperature

$$\rho c_p \frac{dT}{d\hat{t}} \equiv -\rho c_p S_f \frac{dT}{dz}. \quad (\text{A.30})$$

Equations A.27–A.29 are also re-scaled by Equations A.5–A.11 and the additional dimensionless parameter

$$\mathcal{C} = \frac{\rho c_p}{\rho_w c_w}, \quad (\text{A.31})$$

to give the steady, dimensionless conservation equations

$$\frac{d^2\theta}{d\xi^2} - (\mathcal{S}_u - \mathcal{S}_f) \frac{d\theta}{d\xi} - H(\theta - \theta_w) = -\exp\left[-\frac{\beta}{2} \frac{(1 - \theta_f)}{1 - a(1 - \theta_f)}\right] \delta(\xi - \xi_f), \quad (\text{A.32})$$

$$\frac{1}{\text{Le}} \frac{d^2 Y}{d\xi^2} - (\mathcal{S}_u - \mathcal{S}_f) \frac{dY}{d\xi} = \exp\left[-\frac{\beta}{2} \frac{(1 - \theta_f)}{1 - a(1 - \theta_f)}\right] \delta(\xi - \xi_f), \quad (\text{A.33})$$

$$\frac{d^2\theta_w}{d\xi^2} \frac{\alpha_w}{\alpha} - \mathcal{S}_f \frac{d\theta_w}{d\xi} + HC(\theta - \theta_w) = 0. \quad (\text{A.34})$$

The boundary conditions are:

$$\begin{aligned} \xi \rightarrow -\infty : \quad & \theta = 0, \quad \theta_w = 0, \quad Y = 1; \\ \xi \rightarrow +\infty : \quad & \frac{d\theta}{d\xi} = 0, \quad \frac{d\theta_w}{d\xi} = 0, \quad \frac{dY}{d\xi} = 0, \end{aligned} \quad (\text{A.35})$$

where the coordinate system is centred around the reaction layer at $\xi = \xi_f = 0$.

These equations are to be solved asymptotically. Following the procedure in Section, the jump conditions at the reaction layer are:

$$\xi = \xi_f : \quad \theta^+ = \theta^- = \theta_f, \quad Y^+ = 0, \quad (\text{A.36})$$

$$\left. \frac{d\theta}{d\xi} \right|_{\xi_f}^+ - \left. \frac{d\theta}{d\xi} \right|_{\xi_f}^- = \frac{1}{\text{Le}} \left. \frac{dY}{d\xi} \right|_{\xi_f}^-, \quad (\text{A.37})$$

$$\frac{1}{\text{Le}} \frac{dY}{d\xi} \Big|_{\xi_f}^- = \exp \left[-\frac{\beta}{2} \frac{(1 - \theta_f)}{1 - a(1 - \theta_f)} \right]. \quad (\text{A.38})$$

The species equation (A.33) can, again, be solved directly with the boundary conditions to obtain the species profile:

$$Y = \begin{cases} 1 - \exp[-\text{Le}(\mathcal{S}_u - \mathcal{S}_f)\xi] & \text{if } \xi < \xi_f^+ \\ 0 & \text{if } \xi \geq \xi_f^+ \end{cases} \quad (\text{A.39})$$

Isolating θ_w in Equation A.32 and substitution into Equation A.34 gives a third-order homogeneous differential equation in θ :

$$\begin{aligned} \frac{\alpha_w}{\alpha} \frac{1}{\mathcal{C}} \frac{d^3\theta}{d\xi^3} - \left[\left(\frac{\mathcal{S}_u - \mathcal{S}_f}{\mathcal{C}} \right) \frac{\alpha_w}{\alpha} - \frac{\mathcal{S}_f}{\mathcal{C}} \right] \frac{d^2\theta}{d\xi^2} - \left[\frac{\alpha_w}{\alpha} \frac{H}{\mathcal{C}} + H + \frac{\mathcal{S}_f(\mathcal{S}_u - \mathcal{S}_f)}{\mathcal{C}} \right] \frac{d\theta}{d\xi} \\ + \left[(\mathcal{S}_u - \mathcal{S}_f)H - \frac{\mathcal{S}_f}{\mathcal{C}} \right] \theta = 0. \end{aligned} \quad (\text{A.40})$$

This ordinary differential equation has three eigenvalues. Assuming that they are real and distinct:

$$\lambda_1 > 0, \quad (\text{A.41})$$

$$\lambda_2 > 0, \quad (\text{A.42})$$

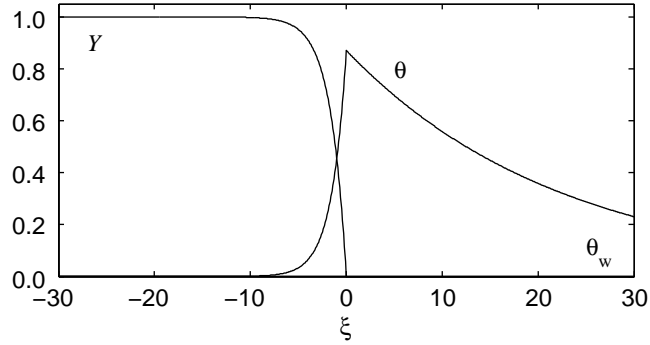
$$\lambda_3 < 0. \quad (\text{A.43})$$

The resulting temperature profiles are

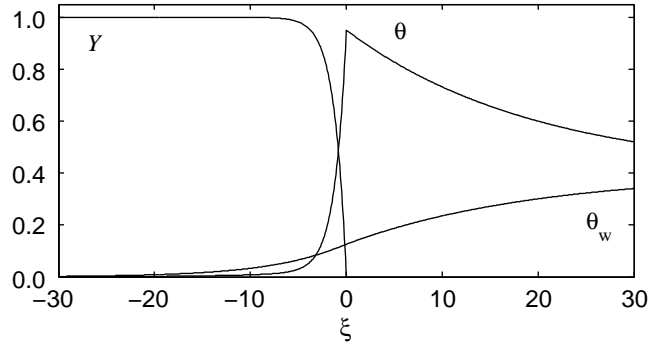
$$\theta = \begin{cases} (\theta_f - C_1) \exp(\lambda_1 \xi) + C_1 \exp(\lambda_2 \xi) & \text{if } \xi < \xi_f \\ (\theta_f - C_2) \exp(\lambda_3 \xi) + C_2 & \text{if } \xi > \xi_f \end{cases} \quad (\text{A.44})$$

$$\theta_w = \begin{cases} C_3(\theta_f - C_1) \exp(\lambda_1 \xi) + C_4 C_1 \exp(\lambda_2 \xi) & \text{if } \xi < \xi_f \\ C_5(\theta_f - C_2) \exp(\lambda_3 \xi) + C_2 & \text{if } \xi > \xi_f \end{cases} \quad (\text{A.45})$$

where it is assumed that the far downstream temperature in the gas and the wall are at equilibrium, therefore



(a)



(b)

Figure A.1 Typical profiles obtained from the propagating solution: (a) fast flame, (b) slow flame.

$$\theta(\infty) = \theta_w(\infty) = C_2 = \frac{(\mathcal{S}_u - \mathcal{S}_f)\mathcal{C}}{\mathcal{S}_u\mathcal{C} - \mathcal{S}_f(\mathcal{C} - 1)}. \quad (\text{A.46})$$

The other constants are obtained from the boundary conditions and have the form

$$C_3 = 1 + \frac{(\mathcal{S}_u - \mathcal{S}_f)\lambda_1 - \lambda_1^2}{H}, \quad (\text{A.47})$$

$$C_4 = 1 + \frac{(\mathcal{S}_u - \mathcal{S}_f)\lambda_2 - \lambda_2^2}{H}, \quad (\text{A.48})$$

$$C_5 = 1 + \frac{(\mathcal{S}_u - \mathcal{S}_f)\lambda_3 - \lambda_3^2}{H}. \quad (\text{A.49})$$

$$C_3(\theta_f - C_1) + C_4C_2 = C_5(\theta_f - C_2) + C_2, \quad (\text{A.50})$$

$$\mathcal{S}_f - \mathcal{S}_u = \theta_f(\lambda_3 - \lambda_1) - C_2\lambda_3. \quad (\text{A.51})$$

Typical temperature and specie profiles which result from the calculation are shown in Figure A.1. The resulting solution is

$$\mathcal{S}_u - \mathcal{S}_f = \exp \left[-\frac{\beta}{2} \frac{(1 - \theta_f)}{1 - a(1 - \theta_f)} \right]. \quad (\text{A.52})$$

A solution curve can be obtained by a continuation methodology where the solution is stepped in burning rate, $\mathcal{S}_u - \mathcal{S}_f$, while the independent variable, either H or \mathcal{S}_u , is determined by applying a root finding algorithm to Equation A.52. The resulting solution curves are shown in Figure 6.1 and 6.2.

Equation A.52 reduces to other canonical solutions, with certain assumptions [106]. For no inlet flow velocity and in the limit of zero wall thermal conductivity, $\alpha_w = 0$, there is coupling between the flame and the wall, but no heat recirculation through them. The problem reduces to the Joulin and Deshaies [107] solution for a diluted, particle laden flame

$$\ln(\mathcal{S}_u - \mathcal{S}_f)^2 = -\frac{\beta H [2(\mathcal{S}_u - \mathcal{S}_f)^2 + \mathcal{C}H]}{[(\mathcal{S}_u - \mathcal{S}_f)^2 + \mathcal{C}H]^2}, \quad (\text{A.53})$$

and, in the limit of $\mathcal{C} \rightarrow 0$, there is no temperature variation in the wall, and the solution reduces to Spalding [6] for a flame propagating in an isothermal wall

$$\ln(\mathcal{S}_u - \mathcal{S}_f)^2 = -\frac{2\beta H}{(\mathcal{S}_u - \mathcal{S}_f)^2}, \quad (\text{A.54})$$

which produces the characteristic behaviour of a stable and unstable solution for fast propagation connected at the extinction point, S_{cr} , in Figure A.2.

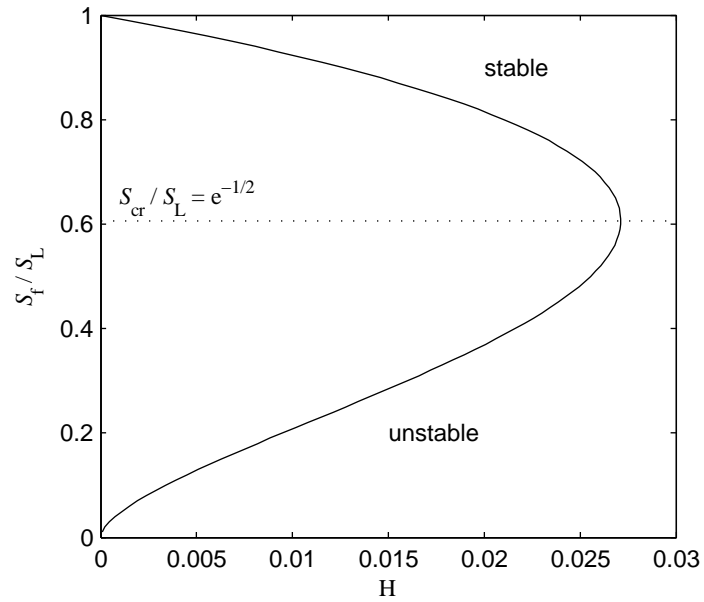


Figure A.2 Solution for normalized burning rate versus dimensionless interfacial heat transfer coefficient, H , for the Spalding [6] solution of a flame in an isothermal channel. The value S_{cr} represents the critical burning rate where extinction occurs.

Appendix B

Furnace heat transfer analysis

A reason for choosing the furnace geometry used in the experiments is the possibility of constructing idealised heat transfer models to analytically determine tube wall temperature profiles. This appendix outlines one approach to solve this problem. The furnace consists of radiant heaters which are used to supply the energy needed to produce very high temperatures in the tube wall. Radiation is, therefore, assumed to be the dominant mode of heat transfer. The analysis will take the form of a simple radiation problem where the furnace-tube assembly is modeled as an enclosure where radiation is exchanged between the surfaces and some is also lost to the ambient environment. Temperature profiles along the tube and furnace walls can be calculated as long as the enclosure geometry, the radiant flux, \dot{q}_{rad} of the heaters, the emissivities, ϵ , of the tube and furnace walls, and ambient temperature, T_{∞} , are known.

View factors for each surface on the furnace and tube walls must be determined to account for the effects of orientation on radiant heat transfer. A view factor represents the fraction of radiation that leaves a surface to strike another in the enclosure, and is a purely geometric quantity that is independent of surface properties and temperature. The basis of the calculation is a simple unit cell, shown in Figure B.1a, which consists of four surfaces: one for the tube (1), one for furnace wall (2), and two end caps (3 and 4) which can be either opaque or transparent to radiant heat transfer. Many of the view factors for these surfaces are known and can be found in the literature [7–9, 108, 109]. The view factor, F , of the tube onto the furnace is given by [7]:

$$F_{1 \rightarrow 2} = \frac{1}{\pi \mathcal{R}_1} \left[\begin{aligned} & \frac{1}{2}(\mathcal{R}_2^2 - \mathcal{R}_1^2 - 1) \cos^{-1} \frac{\mathcal{R}_1}{\mathcal{R}_2} + \pi \mathcal{R}_1 \\ & - \frac{\pi}{2} \mathcal{A} \mathcal{B} - 2 \mathcal{R}_1 \tan^{-1} \sqrt{\mathcal{R}_2^2 - \mathcal{R}_1^2} \\ & + \sqrt{(1 + \mathcal{A}^2)(1 + \mathcal{B}^2)} \sqrt{\frac{(1 + \mathcal{A}^2)\mathcal{B}}{(1 + \mathcal{B}^2)\mathcal{A}}} \end{aligned} \right], \quad (\text{B.1})$$

where $\mathcal{R}_1 = r_1/l$, $\mathcal{R}_2 = r_2/l$, $\mathcal{A} = \mathcal{R}_2 + \mathcal{R}_1$ and $\mathcal{B} = \mathcal{R}_2 - \mathcal{R}_1$. The concentric nature of the geometry also allows for the furnace wall to see itself, generating a second view factor:

$$F_{2 \rightarrow 2} = \frac{1}{\pi \mathcal{R}_1} \left[\begin{aligned} & \pi(\mathcal{R}_1 - \mathcal{R}_2) + \cos^{-1} \left(\frac{\mathcal{R}_2}{\mathcal{R}_1} \right) \\ & - \sqrt{1 + 4\mathcal{R}_1^2} \tan^{-1} \frac{\sqrt{(1 + 4\mathcal{R}_1^2)(\mathcal{R}_1^2 - \mathcal{R}_2^2)}}{\mathcal{R}_2} \\ & + 2\mathcal{R}_2 \tan^{-1} 2\sqrt{\mathcal{R}_1^2 - \mathcal{R}_2^2} \end{aligned} \right]. \quad (\text{B.2})$$

Furthermore, the tube wall has oblique views of the end caps, through which heat will flow into or out of the unit cell. For example, $F_{1 \rightarrow 4}$ is given by

$$F_{1 \rightarrow 4} = \frac{1}{\pi} \left[\begin{aligned} & \mathcal{D}_{1-4} \left(\tan^{-1} \frac{\mathcal{X}}{\mathcal{L}_4} - \tan^{-1} \frac{2\mathcal{X}}{\mathcal{L}_4} \right) + \frac{\mathcal{L}_4}{4} \left\{ \sin^{-1}(2\mathcal{D}_{1-4} - 1) - \sin^{-1} \mathcal{D}_{1-4} \right\} \\ & + \frac{\mathcal{X}^2}{4\mathcal{L}_4} \left(\frac{\pi}{2} + \sin^{-1} \mathcal{D}_{1-4} \right) - \frac{\sqrt{(1 + \mathcal{D}_{1-4}^2 + \mathcal{L}_4^2)^2 - 4\mathcal{D}_{1-4}^2}}{4\mathcal{L}_4} \left(\frac{\pi}{2} + \sin^{-1} \mathcal{Y} \right) \\ & + \frac{\sqrt{4 + \mathcal{L}_4^2}}{4} \left\{ \frac{\pi}{2} + \sin^{-1} \left(1 - \frac{2\mathcal{D}_{1-4}\mathcal{L}_4^2}{4\mathcal{X}^2 + \mathcal{L}_4^2} \right) \right\} \end{aligned} \right], \quad (\text{B.3})$$

where $\mathcal{L}_4 = l/r_4$, $\mathcal{D}_{1-4} = r_1/r_4$, $\mathcal{X} = \sqrt{1 - \mathcal{D}_{1-4}^2}$, $\mathcal{Y} = \mathcal{D}_{1-4}(1 - \mathcal{D}_{1-4}^2 - \mathcal{L}_4^2)/(1 - \mathcal{D}_{1-4}^2 + \mathcal{L}_4^2)$. These end caps can, likewise, communicate with each other, with the following view factor:

$$F_{3 \rightarrow 4} = 1 - \left(\frac{\mathcal{L}_3}{\mathcal{D}_{3-4}^2 - 1} \right) [1 - \mathcal{D}_{3 \rightarrow 4}(F_{2 \rightarrow 2} + 2F_{2 \rightarrow 1} - 1)]. \quad (\text{B.4})$$

The above equations allow for direct calculation of 8 view factors out of the 16 view factors in the cell. Many of the remaining factors are determined from the reciprocity rule:

$$A_i F_{i \rightarrow n} = A_n F_{n \rightarrow i}, \quad (\text{B.5})$$

where A is the area surface; and, because radiation leaving a surface is conserved, the sum of all view factors from a surface is unity:

$$\sum_{n=1}^N F_{i \rightarrow n} = 1, \quad (\text{B.6})$$

allowing determination of the remaining view factors.

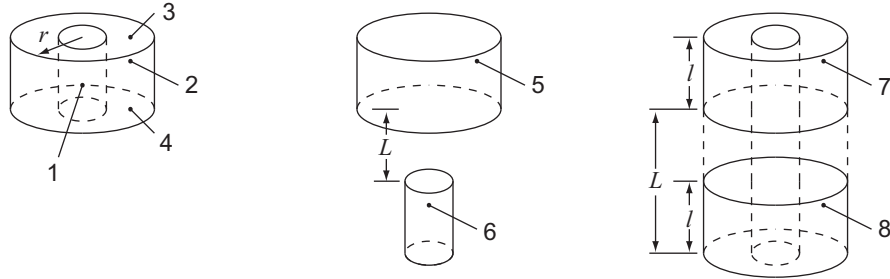


Figure B.1 Fundamental cell geometries: (a) unit cell of concentric cylinders [7], (b) offset cylinders [8] separated by a distance, L , and (c) parallel cylinders [9].

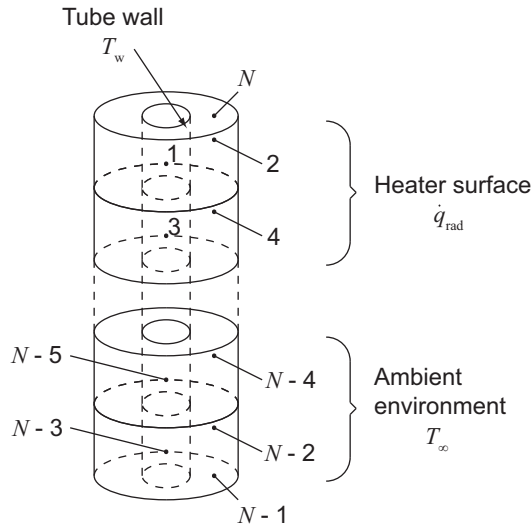


Figure B.2 Unit cell stack for calculation of radiant furnace and tube view factors, of N faces.

Unit cells are stacked together, in Figure B.3, to form the enclosure for the furnace and tube wall. This discretisation is done so that the surfaces can be treated, later on, as being isothermal when carrying out the heat transfer analysis. There are three types of surfaces found in the enclosure. The first are furnace surfaces where radiant energy is injected into the enclosure. This energy soaked up by the second type of central surfaces, which are the tube walls. In the experimental apparatus, the tube is longer than the furnace to set-up

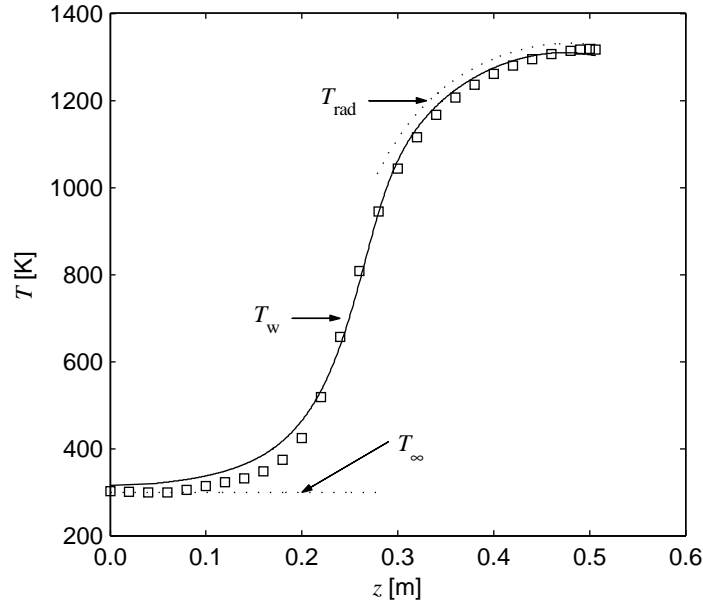


Figure B.3 Predicted furnace surface, T_{rad} , and tube wall, T_w , temperature profiles compared to experimentally obtained temperatures (squares) for the tube wall.

the monotonically varying wall temperature profile. This is modeled here by a third type of non-reradiating surface in the place of the furnace walls, on the outer part of the enclosure, which is set to the ambient temperature of the environment.

There are a total of N surfaces which define the enclosure, where $N(N - 1)/2$ view factors must be determined directly by application of the configurations in Figure B.1, by some combination of these geometries, or by symmetry, while the remaining are determined by reciprocity relations. Hundreds of surfaces are needed to get fully resolved temperature profiles. The number of view factor calculations goes up quadratically with N , therefore, the calculation can quickly become quite cumbersome. An algorithm to solve an arbitrary number of these factors is presented at the end of this appendix which makes these calculations easier.

During a radiation interaction, a surface loses energy by emitting radiation and gains energy by absorbing emitted radiation from other surfaces. The radiative energy leaving a surface is represented by surface radiosity, J . The radiosity of a surface consists of emitted and reflected radiation and, thus, represents the total radiation energy leaving the surface. In the N -surface enclosure, conservation of energy requires that the net heat transfer from

a surface, i , be equal to the sum of the net heat transfers from this surface to each of the N surfaces in the enclosure. When the surface heat flux, \dot{q}_i , is known:

$$\dot{q}_i = \sum_{n=1}^N \dot{q}_{i \rightarrow n} = \sum_{n=1}^N A_i F_{i \rightarrow n} (J_i - J_n). \quad (\text{B.7})$$

This network representation can also be recast to determine radiocities where the surface temperature, T_i , is known:

$$\sigma T_i^4 - J_i = \sum_{n=1}^N \frac{1 - \epsilon_i}{\epsilon_i} F_{i \rightarrow n} (J_i - J_n). \quad (\text{B.8})$$

A third, and final, type of relation are for re-radiating surfaces where

$$\sigma T_i^4 = J_i. \quad (\text{B.9})$$

The above equations give N algebraic equations for the enclosure, for determination of the N unknown radiocities. In the calculation, the surfaces are assumed to be opaque, diffuse absorbers and emitters, and that the surfaces are “grey,” in that their radiation properties are independent of wavelength. Once the radiocities, $J_1 \dots J_N$, are available, the unknown heat transfer rates and temperatures are determined from Equations B.7 and B.8.

Figure B.3 shows a comparison of the simulated temperature profiles, obtained from the calculation, to experimental measurements of the tube wall. There is good agreement in the furnace zone, however, agreement is less perfect outside the furnace at the tube inlet, where the effect of radiation is reduced and conduction is more influential. Nevertheless, the results illustrate the dominance of radiative heat transfer in setting the wall temperature profile.

```

%%%%%%%%%%%%%%%%%%%%%%%%%%%%%%%%%%%%%%%%%%%%%%%%%%%%%%%%%%%%%%%%%%%%%%%%%%%%%%
% FURNACE VIEW FACTORS
%   Calculates view factors for tube and surface elements in a furnace
%   made of an idealised concentric cylinder geometry. In this
%   calculation, the length of each element is set to be equal,
%   however, this could be made to be general by modifying the equations.
%
%   The equations to calculate view factors have been cited. Another
%   source for these equations is J.R. Howell's "Catalog of Radiation
%   Heat Transfer Configuration Factors":
%
%       http://www.engr.uky.edu/rtl/Catalog/
%
%   The catalog number has been given, where possible.
%%%%%%%%%%%%%%%%%%%%%%%%%%%%%%%%%%%%%%%%%%%%%%%%%%%%%%%%%%%%%%%%%%%%%%%%%%%%%%

% variables

LnHtr = 30;      % length of heater

IHtr = 100;      % number of heater surfaces
ITube = 200;     % number of tube surfaces

R1 = 1;         % radius of quartz tube
R2 = 10;        % radius of burner

N = ITube;       % number of unit cells
l = LnHtr / IHtr; % length of each unit cell [cm/cell]
I = 2*N + 2;     % total number of surfaces (includes end surfaces) in the enclosure

LnTube = l*ITube;

fprintf('Parameters:\n')
fprintf('Heater: Length = %8.4f, Radius = %8.4f.\n',LnHtr,R2)
fprintf('Tube: Length = %8.4f, Radius = %8.4f.\n',LnTube,R1)
fprintf('%d unit element(s).\n\n',N)

fprintf('Calculating view factors ... ')

% initialize the view factor matrix
F = zeros(I,I);

% set the self views to zero
for i = 1 : 2 : I-2
    for j = 1 : 2 : I-2
        F(i,j) = 0;
    end
end

% using (Leuenberger, H. and Person, R.A., 1956) [C-91: Interior of finite
% length right circular coaxial cylinder to itself.]
R = R2/R1; L = l/R1;
A = L^2 + R^2 - 1; B = L^2 - R^2 + 1;
j = 1;
for i = 2 : 2 : I-2
    F(i,j) = 1/R - 1/pi/R * (acos(B/A) - 1/2/L * (sqrt((A+2)^2 - (2*R)^2)*acos(B/R/A)+B*asin(1/R)-pi*A/2));
    F(i,j+1) = 1 - 1/R + 2/pi/R*atan(2*sqrt(R^2-1)/L) - L/2/pi/R
        * (sqrt(4*R^2+L^2)/L*asin((4*(R^2-1)+(L^2/R^2)*(R^2-2))/(L^2+4*(R^2-1)))
        - asin((R^2-2)/R^2) + pi/2*(sqrt(4*R^2+L^2)/L - 1));
    F(j,i) = R2/R1 * F(i,j); % reciprocity relation
    j = j + 2;
end

% Calculate the factors for a unit cell. This will be important for later.
F_unit(1,1) = 0;
F_unit(1,2) = F(1,2);
F_unit(1,3) = (1 - F_unit(1,2)) / 2; F_unit(3,1) = 2*R1*l/(R2^2-R1^2)*F_unit(1,3);
F_unit(1,4) = F_unit(1,3); F_unit(4,1) = F_unit(3,1);
F_unit(2,1) = F(2,1);
F_unit(2,2) = F(2,2);
F_unit(2,3) = (1 - F_unit(2,1) - F_unit(2,2))/2; F_unit(3,2) = 2*R2*l/(R2^2-R1^2)*F_unit(2,3);
F_unit(2,4) = F_unit(2,3); F_unit(4,2) = F_unit(3,2);
F_unit(3,3) = 0;
F_unit(3,4) = 1 - F_unit(3,1) - F_unit(3,2);
F_unit(4,3) = 1 - F_unit(4,1) - F_unit(4,2);
F_unit(4,4) = 0;

% using (Leuenberger, H. and Person, R.A., 1956) [C-91: Interior of finite
% length right circular coaxial cylinder to itself.] for double stacked
% unit cells
R = R2/R1; L = 2*l/R1;
A = L^2 + R^2 - 1; B = L^2 - R^2 + 1;

F_ba = 1/R - 1/pi/R * (acos(B/A) - 1/2/L * (sqrt((A+2)^2 - (2*R)^2)*acos(B/R/A)+B*asin(1/R)-pi*A/2));

```

Figure B.4 A code to calculate furnace and tube view factors.


```

% back to the view factor calc. using (Rea, Samuel N., 1975)
R = R1/R2; Y = 1/R2; L = 1/R2;
% do the odd lines. Fill in the rest with reciprocity.
for i = 1 : 2 : I-2
    for j = 2 : 2 : I-2
        if (i ~= j-1) && (mod(j,2)==0)
            % determine displacement wrt. unit cell number
            D = (abs((i+1)/2-j/2)-1)*1/R2;
            if (D == 0)
                % special case. use a double stacked unit cell formulation
                F(j,i) = F_ba - F(2,1);
                F(i,j) = R2/R1 * F(j,i); % reciprocity relation
            elseif (D > 0)
                % [C-98: Outside of inner (smaller) coaxial cylinder to
                % inside of larger cylinder; smaller cylinder completely
                % outside larger.]

                % F_L+D
                zeta = L+D;
                A = (zeta)^2 + R^2 - 1; B = (zeta)^2 - R^2 + 1;
                F_L_D = B/8/R/zeta + 1/2/pi * (acos(A/B) - 1/2/zeta*((A+2)^2/R^2-4)^0.5*acos(A*R/B) - A/2/zeta/R*asin(R));
                % F_Y+D
                zeta = Y+D;
                A = (zeta)^2 + R^2 - 1; B = (zeta)^2 - R^2 + 1;
                F_Y_D = B/8/R/zeta + 1/2/pi * (acos(A/B) - 1/2/zeta*((A+2)^2/R^2-4)^0.5*acos(A*R/B) - A/2/zeta/R*asin(R));
                % F_D
                zeta = D;
                A = (zeta)^2 + R^2 - 1; B = (zeta)^2 - R^2 + 1;
                F_D = B/8/R/zeta + 1/2/pi * (acos(A/B) - 1/2/zeta*((A+2)^2/R^2-4)^0.5*acos(A*R/B) - A/2/zeta/R*asin(R));
                % F_L+D+Y
                zeta = L+D+Y;
                A = (zeta)^2 + R^2 - 1; B = (zeta)^2 - R^2 + 1;
                F_L_D_Y = B/8/R/zeta + 1/2/pi * (acos(A/B) - 1/2/zeta*((A+2)^2/R^2-4)^0.5*acos(A*R/B) - A/2/zeta/R*asin(R));
                F(i,j) = (L+D)/L*F_L_D + (Y+D)/L*F_Y_D - D/L*F_D - (L+D+Y)/L*F_L_D_Y;
                F(j,i) = R1/R2 * F(i,j); % reciprocity relation
            end
        end
    end
end
end

L1 = 1;
L2 = 1;
for i = 2 : 2 : I-2
    for j = 2 : 2 : I-2
        if (i ~= j)
            d = (abs(i/2-j/2)-1)*1; % determine displacement wrt unit cell number

            if (d > 0)
                % using (Tso, C.P. and Mahulikar, S.P., 1999) [C-99: Between equal
                % length cylindrical areas on interior of outer coaxial cylinder.]

                % F_L1+L2+d
                zeta = L1+L2+d; Xt = R1/zeta; Xs = R2/zeta;
                F_L1_L2_d = 1/pi/Xs * (pi*(Xs-Xt) + acos(Xt/Xs) - sqrt(1+4*Xs^2)*atan(sqrt((1+4*Xs^2)*(Xs^2-Xt^2))/Xt)
                + 2*Xt*atan(2*sqrt(Xs^2-Xt^2)));
                % F_L1+d
                zeta = L1+d; Xt = R1/zeta; Xs = R2/zeta;
                F_L1_d = 1/pi/Xs * (pi*(Xs-Xt) + acos(Xt/Xs) - sqrt(1+4*Xs^2)*atan(sqrt((1+4*Xs^2)*(Xs^2-Xt^2))/Xt)
                + 2*Xt*atan(2*sqrt(Xs^2-Xt^2)));
                % F_L2+d
                zeta = L2+d; Xt = R1/zeta; Xs = R2/zeta;
                F_L2_d = 1/pi/Xs * (pi*(Xs-Xt) + acos(Xt/Xs) - sqrt(1+4*Xs^2)*atan(sqrt((1+4*Xs^2)*(Xs^2-Xt^2))/Xt)
                + 2*Xt*atan(2*sqrt(Xs^2-Xt^2)));
                % F_d
                zeta = d; Xt = R1/zeta; Xs = R2/zeta;
                F_d = 1/pi/Xs * (pi*(Xs-Xt) + acos(Xt/Xs) - sqrt(1+4*Xs^2)*atan(sqrt((1+4*Xs^2)*(Xs^2-Xt^2))/Xt)
                + 2*Xt*atan(2*sqrt(Xs^2-Xt^2)));
                F(i,j) = ((L1+L2+d)*F_L1_L2_d - (L1+d)*F_L1_d - (L2+d)*F_L2_d + d*F_d)/2/L1;
            elseif (d == 0)
                % special case. tried a double stacked unit cell
                % formulation, however could not find the analytical
                % solution. Instead, use the limit d->0 of the solution
                % for d>0 (outlined above)

                d = 1e-14; % set the distance to a very small number
                % F_L1+L2+d
                zeta = L1+L2+d; Xt = R1/zeta; Xs = R2/zeta;
                F_L1_L2_d = 1/pi/Xs * (pi*(Xs-Xt) + acos(Xt/Xs) - sqrt(1+4*Xs^2)*atan(sqrt((1+4*Xs^2)*(Xs^2-Xt^2))/Xt)
                + 2*Xt*atan(2*sqrt(Xs^2-Xt^2)));
                % F_L1+d
                zeta = L1+d; Xt = R1/zeta; Xs = R2/zeta;
                F_L1_d = 1/pi/Xs * (pi*(Xs-Xt) + acos(Xt/Xs) - sqrt(1+4*Xs^2)*atan(sqrt((1+4*Xs^2)*(Xs^2-Xt^2))/Xt)
                + 2*Xt*atan(2*sqrt(Xs^2-Xt^2)));
            end
        end
    end
end

```

Figure B.4 View factor code, continued.

```

    % F_L2+d
    zeta = L2+d; Xt = R1/zeta; Xs = R2/zeta;
    F_L2_d = 1/pi/Xs * (pi*(Xs-Xt) + acos(Xt/Xs) - sqrt(1+4*Xs^2)*atan(sqrt((1+4*Xs^2)*(Xs^2-Xt^2))/Xt)
    + 2*Xt*atan(2*sqrt(Xs^2-Xt^2)));
    % F_d
    zeta = d; Xt = R1/zeta; Xs = R2/zeta;
    F_d = 1/pi/Xs * (pi*(Xs-Xt) + acos(Xt/Xs) - sqrt(1+4*Xs^2)*atan(sqrt((1+4*Xs^2)*(Xs^2-Xt^2))/Xt)
    + 2*Xt*atan(2*sqrt(Xs^2-Xt^2)));
    F(i,j) = ((L1+L2+d)*F_L1_L2_d - (L1+d)*F_L1_d - (L2+d)*F_L2_d + d*F_d)/2/L1;
end
end
end
end

% now do the ends...

% cap factors first. Using (Sparrow, E.M.; Miller, G.B.; and Jonsson, V.K.,
% 1962) [C-94: Annular end enclosing space between coaxial right circular
% cylinders to opposite annular end.]
R = R2/R1; L = LnHtr/R1;
A = L^2 + R^2 - 1; B = L^2 - R^2 + 1;
F_b_a = 1/R - 1/pi/R * (acos(B/A) - 1/2/L * (sqrt((A+2)^2 - (2*R)^2)*acos(B/R/A)+B*asin(1/R)-pi*A/2));
F_b_b = 1 - 1/R + 2/pi/R*atan(2*sqrt(R^2-1)/L) - L/2/pi/R
    * (sqrt(4*R^2+L^2)/L*asin((4*(R^2-1)+(L^2/R^2)*(R^2-2))/(L^2+4*(R^2-1)))
    - asin((R^2-2)/R^2) + pi/2*(sqrt(4*R^2+L^2)/L - 1));

H = LnHtr/R1;
F(2*N+1,2*N+2) = 1 - (H/(R^2-1))*(1-R*(F_b_b + 2*F_b_a - 1));
F(2*N+2,2*N+1) = F(2*N+1,2*N+2);
F(2*N+1,2*N+1) = 0;
F(2*N+2,2*N+2) = 0;

% now from unit cell analysis, complete the bottom and top rows
F(1,I-1) = F_unit(1,3); F(I-1,1) = F_unit(3,1);
F(2,I-1) = F_unit(2,3); F(I-1,2) = F_unit(3,2);
sum = 0;
sum2 = 0;
for j = 1 : I-1
    sum = sum + F(1,j);
    sum2 = sum2 + F(2,j);
end
F(1,I) = 1 - sum; F(I,1) = 2*R1*1/(R2^2-R1^2)*F(1,I);
F(2,I) = 1 - sum2; F(I,2) = 2*R2*1/(R2^2-R1^2)*F(2,I);

% fill in the rest with fictitious upper and lower surfaces and the
% summation rule

% odd rows
for i = 3 : 2 : I-2
    % above the unit cell
    sum = 0;
    for j = 1 : i-1
        sum = sum + F(i,j);
    end
    F(i,I-1) = F_unit(1,3) - sum;
    F(I-1,i) = 2*R1*1/(R2^2-R1^2) * F(i,I-1);
    % below the unit cell
    sum = 0;
    for j = i+2 : I-2
        sum = sum + F(i,j);
    end
    F(i,I) = F_unit(1,4) - sum;
    F(I,i) = 2*R1*1/(R2^2-R1^2) * F(i,I);
end

% even rows
for i = 4 : 2 : I-2
    % above the unit cell
    sum2 = 0;
    for j = 1 : i-2
        sum2 = sum2 + F(i,j);
    end
    F(i,I-1) = F_unit(2,3) - sum2;
    F(I-1,i) = 2*R2*1/(R2^2-R1^2) * F(i,I-1);
    % below the unit cell
    sum2 = 0;
    for j = i+1 : I-2
        sum2 = sum2 + F(i,j);
    end
    F(i,I) = F_unit(2,4) - sum2;
    F(I,i) = 2*R2*1/(R2^2-R1^2) * F(i,I);
end

fprintf('DONE.\n\n')

```

Figure B.4 View factor code, continued.

Appendix C

Mixture composition

Two parameters of considerable importance in scaling the flame-in-tube problem are flame speed, S_L , and flame thickness, δ_f . For a standard, adiabatic flame, these are given by classic Thermal Theory [110] as

$$S_L \propto \sqrt{\frac{\alpha_{\text{eff}}}{\tau_c}}, \quad \delta_f \propto \sqrt{\alpha_{\text{eff}} \tau_c}, \quad (\text{C.1})$$

where α_{eff} is the effective thermal diffusivity and τ_c is a characteristic combustion time. In a standard flame, the system is defined by flame speed. But for a confined flame, heat losses become more important as the tube becomes smaller and flame thickness becomes a controlling parameter. These fundamental parameters are a function of fuel / air mixture. Therefore, it is necessary verify that flame speed and flame thickness are able to scale flame-in-tube problem over a wide range of mixture composition.

Metered methane/air mixtures at fuel lean, stoichiometric and rich equivalence ratios are chosen to test the scaling for burning rate and heat loss. The parameters for these mixtures (A to G) are shown in Table C.1. To test the effect of composition, nitrogen diluent and oxygen concentrations are chosen to tailor the adiabatic flame speed and the flame thickness which result of the mixtures.

Figure C.1 shows a summary of flame position data, obtained experimentally and numerically, for mixtures A, B and C for temperature stabilized combustion in a heat tube (as in Chapter 4). The inner tube diameter is 2 mm. This figure shows inlet flow velocity, S_u , verses the wall temperature at the flame stabilization position, $T_w(z_f)$. Simulated flame

Table C.1 Mixture parameters. Normalized equivalence ratio, $\Phi = \phi/(1+\phi)$. Flame thickness, $\delta_f = (T_{af} - T_u)/(dT/dz|_{\max})$. All parameters are calculated from an adiabatic free flame with the GRI-Mech 3.0 kinetics mechanism.

Mixture	ϕ (Φ)	%O ₂	%N ₂	T_u [K]	T_{af} [K]	S_L [m/s]	δ_f [mm]
A	1.0 (0.50)	21.0	79.0	300	2230	0.372	0.436
B	0.7 (0.41)	21.0	79.0	300	1843	0.190	0.655
C	1.4 (0.58)	21.0	79.0	300	1978	0.137	1.000
D	1.0 (0.50)	17.2	82.8	300	2015	0.204	0.677
E	1.0 (0.50)	15.4	84.6	300	1888	0.136	0.918
F	0.7 (0.41)	25.8	74.2	300	2087	0.369	0.407
G	1.4 (0.58)	26.9	73.1	300	2253	0.372	0.447

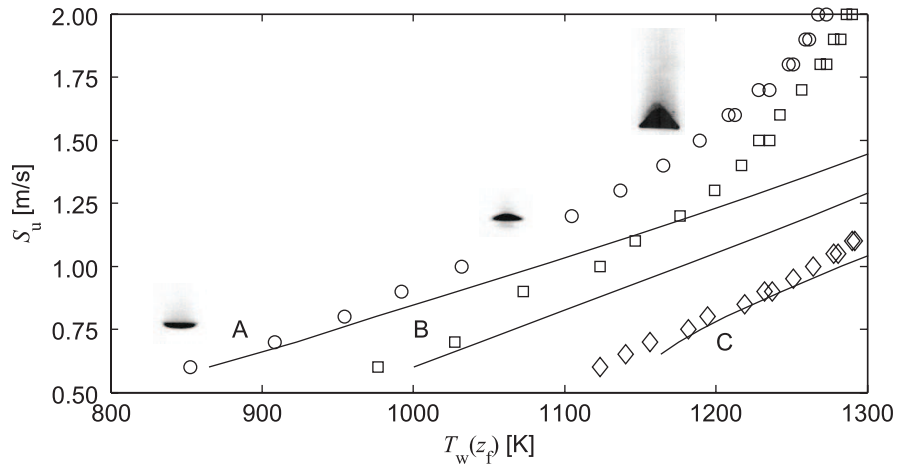
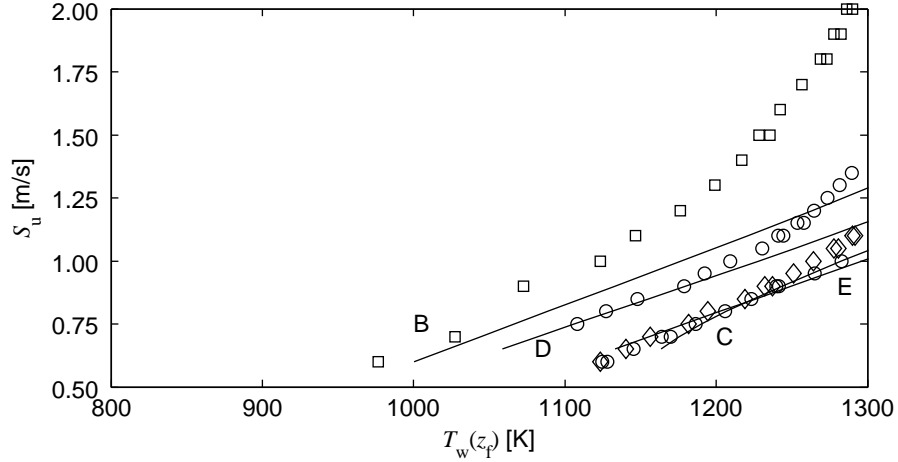
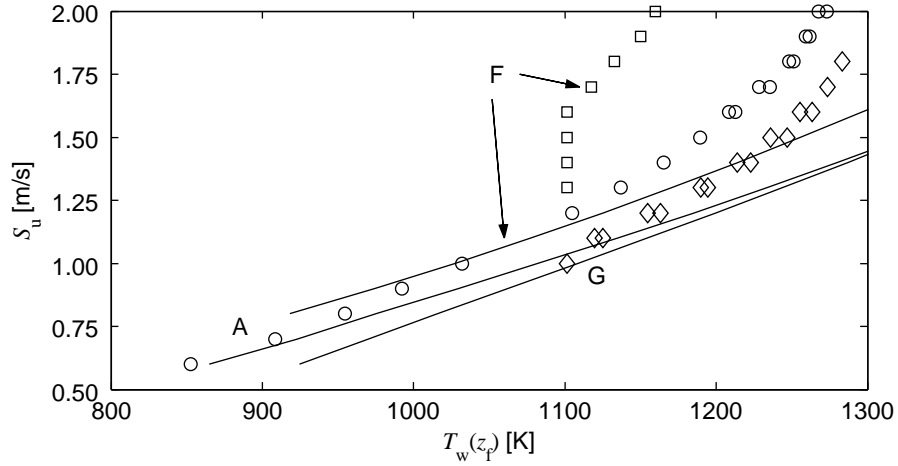


Figure C.1 Experimental (symbols) and simulated (lines) trends in flame stabilization wall temperature, $T_w(z_f)$, due to flame speed, S_L . Stoichiometric (\circ) mixture A, lean (\square) mixture B, rich (\diamond) mixture C. Three images of the stoichiometric flame front, which becomes more curved with increasing inlet velocity, are also shown.



(a)



(b)

Figure C.2 Experimental (symbols) and simulated (lines) trends in flame stabilization wall temperature, $T_w(z_f)$, with flame speeds, S_L , matched via nitrogen-to-oxygen ratio. (a) Lean (\square) mixture B is matched with stoichiometric (\circ), diluted mixture D. Rich (\diamond) mixture C is matched with stoichiometric, diluted mixture E. (b) Stoichiometric mixture A is matched with lean, enriched mixture F and rich, enriched mixture G.

positions are obtained from a 1-D volumetric model, with an interfacial heat transfer sub-model accounting for heat release, developed in Section 2.3.2. The flames in the figure are strongly burning, stable, symmetric flames that have a unique stabilization position within the wall temperature profile. For each mixture, the flame position progressively moves upstream to lower wall temperatures with decreasing inlet flow velocity. Below the lower velocity limit shown in Figure C.1, unstable “flames with repetitive extinction and ignition” (FREI) were observed [46]. It is not possible to reproduce FREI with the present numerical model due to the highly unsteady flame conditions, therefore flames in this regime are not considered.

Trends for flame position can be extracted from the experimental and numerical data, and is shown in Figures C.1 and C.2. It is clear from the figures that flame speed is a leading-order effect for these flames. Flames with higher flame speeds (see Table C.1) have faster burning rates resulting in stabilization positions at lower wall temperatures.

Discrepancies in simulated and experimental flame stabilization positions result from two-dimensional interfacial heat transfer effects and flame curvature. This is apparent when looking at the relative position and shape of the stoichiometric flames (mixture A) in Figure C.1. At low inlet velocities, the flames are relatively flat and there is reasonable agreement between the simulated flames and the experimental measurements. These flat flames lie within the assumption of the volumetric model. However, at the higher inlet flow velocities, the flame position is affected by flame curvature which causes enhanced burning rates due to the increase in flame area perpendicular to the reactant stream. This effect is quite strong at the highest velocities where curved experimental flames are upstream of the predicted stabilization positions.

To clarify the effects of flame thickness, δ_f , mixtures are also tuned to have the same flame speed by modification of nitrogen-to-oxygen ratio. In Figure C.2(a), mixture D and E have stoichiometric equivalence ratios, but are made to have similar flame speeds to mixtures B and C, respectively. Similarly, lean and rich mixtures F and G are tuned to match the flame speed of mixture A in Figure C.2(b).

Figure C.3 gives a summary of all mixture data taken in the experiments. Tuning for flame speed gives stabilization positions which are close to, but do not exactly match corresponding mixtures at the same inlet flow velocity. But, matching S_L through the ratio of α_{eff} and τ_c does not ensure that the product of these variables will give equivalent flame thicknesses (see Equation C.1). These mixtures capture the second-order dependence of

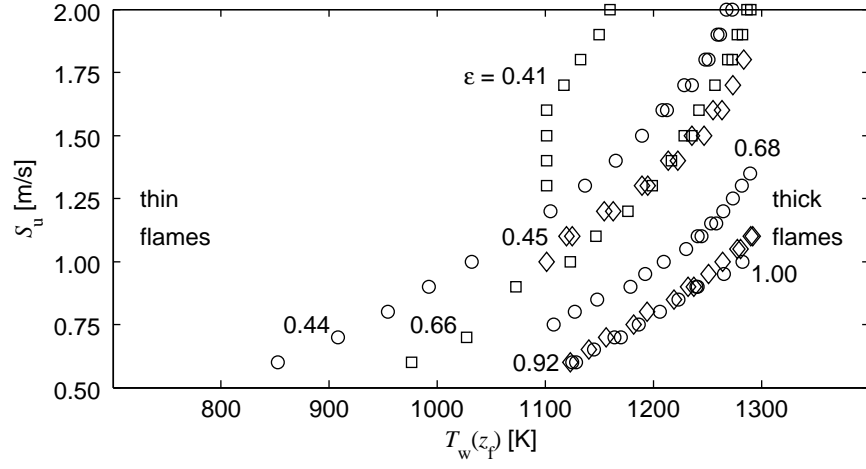


Figure C.3 Experimental (symbols) and simulated (lines) flame stabilization wall temperature, $T_w(z_f)$, versus inlet flow velocity of S_u . Flame thickness is given in terms of the dimensionless value, $\varepsilon = \delta_f/r_w$. Legend as in Figure C.2.

flame thickness. For confined flames, flame stabilization position and the characteristic flame thickness are correlated in that thinner flames have lower heat loss and, therefore, sit upstream of thicker flames.

Appendix D

Solution of the channel boundary layer equations

Using standard boundary layer approximations, the equations for thermal-momentum interaction in the channel are:

Continuity:

$$\frac{\partial \rho u}{\partial z} + \frac{1}{r} \frac{\partial r \rho v}{\partial r} = 0, \quad (\text{D.1})$$

Momentum:

$$\rho u \frac{\partial u}{\partial z} + \rho v \frac{\partial u}{\partial r} + \frac{\partial p}{\partial z} = \frac{\mu}{r} \frac{\partial}{\partial r} \left(r \frac{\partial u}{\partial r} \right), \quad \frac{\partial p}{\partial r} = 0, \quad (\text{D.2})$$

Sensible heat:

$$\rho c_p u \frac{\partial t}{\partial z} + \rho c_p v \frac{\partial t}{\partial r} = \frac{1}{r} \frac{\partial}{\partial r} \left(r \lambda \frac{\partial t}{\partial r} \right) - q_s(r, z), \quad (\text{D.3})$$

Chemical enthalpy:

$$u \frac{\partial \zeta}{\partial z} + v \frac{\partial \zeta}{\partial r} = \frac{\lambda}{\rho c_p} \frac{1}{r} \frac{\partial}{\partial r} \left(r \frac{\partial \zeta}{\partial r} \right) - \dot{\zeta}(r, z), \quad (\text{D.4})$$

where the pressure term in the all but the momentum equation has been neglected. One should also note from momentum that pressure is assumed to be uniform along the radius and a function only of distance down the flow axis.

For reasons which will soon become clear, it is best to first transform the above equations with the von Mises coordinate transformation. The stream function is defined which exactly

satisfies the continuity equation:

$$\rho u r = \frac{\partial \psi}{\partial r} \quad \text{and} \quad \rho v r = -\frac{\partial \psi}{\partial z}. \quad (\text{D.5})$$

Doing so allows for ψ to replace r as the new independent variable. The partial differential operators are transformed with the chain rule:

$$\left(\frac{\partial}{\partial z} \right)_r = \left(\frac{\partial z}{\partial \psi} \right)_r \left(\frac{\partial}{\partial z} \right)_\psi + \left(\frac{\partial \psi}{\partial z} \right)_r \left(\frac{\partial}{\partial \psi} \right)_z, \quad (\text{D.6})$$

$$\left(\frac{\partial}{\partial r} \right)_z = \left(\frac{\partial z}{\partial r} \right)_z \left(\frac{\partial}{\partial z} \right)_\psi + \left(\frac{\partial \psi}{\partial r} \right)_z \left(\frac{\partial}{\partial \psi} \right)_z, \quad (\text{D.7})$$

yielding the following transformed equations:

Continuity:

$$0 = \frac{\partial r^2}{\partial \psi} - \frac{2}{\rho u}, \quad (\text{D.8})$$

Momentum:

$$\rho u \frac{\partial u}{\partial z} + \frac{\partial p}{\partial z} = \mu \rho u \frac{\partial}{\partial \psi} \left(\rho u r^2 \frac{\partial u}{\partial \psi} \right), \quad 0 = \frac{\partial p}{\partial \psi}, \quad (\text{D.9})$$

Gas energy (sensible heat):

$$\rho u c_p \frac{\partial t}{\partial z} = \lambda \rho u \frac{\partial}{\partial \psi} \left(\rho u r^2 \frac{\partial t}{\partial \psi} \right) - q_s(r, z), \quad (\text{D.10})$$

Species (chemical enthalpy):

$$u \frac{\partial \zeta}{\partial z} = \text{Le} \frac{\lambda}{\rho c_p} \rho u \frac{\partial}{\partial \psi} \left(\rho u r^2 \frac{\partial \zeta}{\partial \psi} \right) - \dot{\zeta}_s(r, z), \quad (\text{D.11})$$

in differential-algebraic equation (DAE) form, $\mathbf{F}(\mathbf{y}', \mathbf{y}) = 0$. An explanation of DAEs is provided in Brenan et al. [102]. The transformed boundary conditions are:

$$\begin{aligned} \psi = 0 : \quad r = 0, \quad \frac{\partial u}{\partial \psi} = 0, \quad \frac{\partial t}{\partial \psi} = 0, \quad \frac{\partial \zeta}{\partial \psi} = 0, \\ \psi = \psi_w : \quad r = r_w, \quad u = S_f, \quad t = T_w, \quad \frac{\partial \zeta}{\partial \psi} = 0. \end{aligned} \quad (\text{D.12})$$

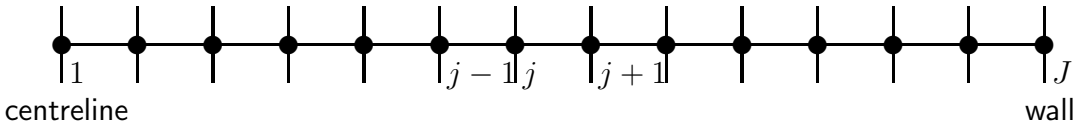
Above, v , as a dependent variable, and the initial form of the continuity equation have been eliminated, but r is no longer independent and must be obtained from Equation D.8. Therefore, there is still four equations and four dependent variables, but the form of the DAEs do offer several improvements.

For initial conditions, the profiles for axial velocity, temperature, and pressure can be specified easily, provided that they are consistent with the physics. However, even though radial velocity was initially an independent variable, it could not be specified independently. This can be seen in the transformed equations. Therefore, there is only one r profile which is consistent with the initial conditions.

It would also be impossible for such equations to be solved by traditional ODE software, which treat equations in the form $\mathbf{y}' = \mathbf{F}(\mathbf{y})$. Thus, such software could only have one time-like derivative in each equation (the momentum equation has two time-like derivatives: $u' = \partial u / \partial z$ and $p' = \partial p / \partial z$). Solution of the initial form of the equations would also be impeded by the fact that there is no explicit boundary condition for pressure, even though this is one of the dependent variables. Contrastingly, the DAE formulation handles these problems easily by the additional algebraic equations that the solution must satisfy.

Figure D.1 shows a stencil of the solution approach at each axial location. The solution uses the Method of Lines and a finite-difference discretization [102]. There are a few things to note. First, the equations have been semi-discretized to form a system of ODEs which are solved with high level software. The residual, \mathbf{F} , is structured as a two-dimensional matrix for each of the solution variables. For example, $F_{u,j}$ is for the axial velocity, u , at each location, j , in the grid, which is solved from the momentum equation D.9. Secondly, the boundary conditions are handled in an unusual manner. It is usually convenient to have one boundary condition for each equation, however there is none for pressure. Though, there are two for r , therefore, the extra condition can be, thus, associated with pressure as an implicit boundary condition. Thirdly, the direction for differencing between the conservation equations and the algebraic constraints are also different. This is especially true for pressure, which involves the points $j + 1$ and j , while the radial coordinate involves the points j and $j - 1$. This is essential for the implicit boundary condition to work. As a final note, in Figure D.1 the variables r and p have been introduced as dependent variables at each grid location. This is for programming convenience. It would be possible to solve r with an integral equivalent to Equation D.8 and p as a global variable, but such a procedure would produce a dense Jacobian structure which would be more difficult to implement in

a computer. Instead, the procedure shown here allows the Jacobian matrix to maintain a banded structure, for which there are many efficient algorithms.

$$\begin{aligned}
 & F_{u,1} = u_2 - u_1 & F_{u,J} &= u_J - 0 \\
 & F_{r,1} = r_1 - 0 & F_{r,J} &= r_J - r_w \\
 & F_{p,1} = p_2 - p_1 & F_{p,J} &= \frac{r_J^2 - r_{J-1}^2}{\psi_J - \psi_{J-1}} - \frac{4}{\rho_J u_J - \rho_{J-1} u_{J-1}} \\
 & F_{T,1} = T_2 - T_1 & F_{T,J} &= T_J - T_w \\
 & F_{\zeta,1} = \zeta_2 - \zeta_1 & F_{\zeta,J} &= \zeta_J - \zeta_{J-1}
 \end{aligned}$$


$$\begin{aligned}
 F_{u,j} &= u'_j + \frac{p'_j}{\rho_j u_j} - \frac{2\mu_j}{\psi_{j+1} - \psi_{j-1}} \left[(\rho u r^2)_{j+1/2} \frac{u_{j+1} - u_j}{\psi_{j+1} - \psi_j} - (\rho u r^2)_{j-1/2} \frac{u_j - u_{j-1}}{\psi_j - \psi_{j-1}} \right] \\
 F_{r,j} &= \frac{r_j^2 - r_{j-1}^2}{\psi_j - \psi_{j-1}} - \frac{4}{\rho_j u_j - \rho_{j-1} u_{j-1}} \\
 F_{p,j} &= p_{j+1} - p_j \\
 F_{T,j} &= c_{p,j} T'_j - \frac{2\lambda_j}{\psi_{j+1} - \psi_{j-1}} \left[(\rho u r^2)_{j+1/2} \frac{T_{j+1} - T_j}{\psi_{j+1} - \psi_j} - (\rho u r^2)_{j-1/2} \frac{T_j - T_{j-1}}{\psi_j - \psi_{j-1}} \right] - \frac{q_{s,j}}{\rho_j} \\
 F_{\zeta,j} &= \zeta'_j - \frac{2\text{Le}\lambda_j}{c_{p,j}(\psi_{j+1} - \psi_{j-1})} \left[(\rho u r^2)_{j+1/2} \frac{\zeta_{j+1} - \zeta_j}{\psi_{j+1} - \psi_j} - (\rho u r^2)_{j-1/2} \frac{\zeta_j - \zeta_{j-1}}{\psi_j - \psi_{j-1}} \right] - \dot{\zeta}_{s,j}
 \end{aligned}$$

Figure D.1 Stencil for the finite-difference representation of the DAE system for the channel boundary layer. The solution procedure is the Method of Lines.

Appendix E

Model sensitivity

The influence of model input parameters on the simulated flame structures can be determined by sensitivity analysis. A burner-stabilized flame can be used to show the sensitivity of flame stabilization position, z_f , to experimental parameters. The logarithmic sensitivity of flame position to each input parameter, x_j , is calculated by

$$L.S.(z_f)_j = \frac{d \log z_f}{d \log x_j} = \frac{\Delta z_f}{z_f} \frac{x_j}{\Delta x_j}. \quad (E.1)$$

The input parameters of interest are the model boundary conditions. To obtain the sensitivities, each boundary condition is manually perturbed by a small amount and the model is re-computed to determine the change in the simulated flame stabilization position, Δz_f .

These logarithmic sensitivities are then used to determine the total uncertainty in the model prediction. The uncertainties in the boundary conditions, σ_{x_j} , are assumed to be independent and the uncertainty in the predicted flame stabilization position is estimated as:

$$\begin{aligned} \sigma_{z_f}^2 &\simeq \sum_j \left(\frac{\Delta z_f}{\Delta x_j} \right)^2 \sigma_{x_j}^2 \simeq z_f^2 \sum_j \left(\frac{\Delta z_f}{z_f} \frac{x_j}{\Delta x_j} \right)^2 \left(\frac{\sigma_{x_j}}{x_j} \right)^2, \\ \sigma_{z_f} &\simeq z_f \sqrt{\sum_j L.S.(z_f)_j^2 \left(\frac{\sigma_{x_j}}{x_j} \right)^2}. \end{aligned} \quad (E.2)$$

Therefore, the $\pm 2\sigma$ error band in Figure 4.7 represents the total uncertainty in the model due to combined uncertainties in boundary conditions obtained from experimental operat-

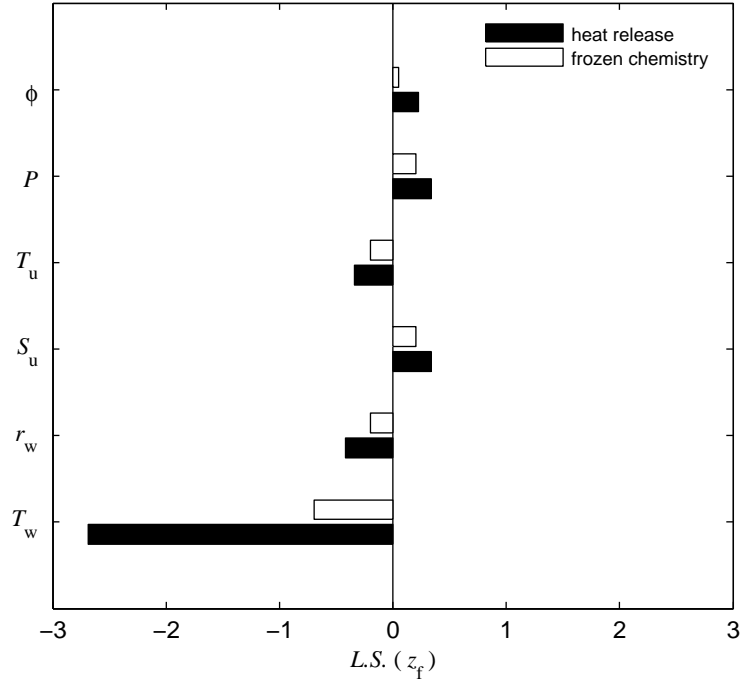


Figure E.1 Flame stabilization position logarithmic sensitivities to the boundary conditions of models which use a boundary layer for interfacial heat transfer with frozen chemistry (white) and with heat release, $Le = 1.0$ (black). $\phi = 1.0$, $S_u = 1.00$ m/s, $T_u = 300$ K.

ing parameters and the measurements.

Figure E.1 compares the logarithmic sensitivities for the predicted flame position for volumetric models which use the boundary layer sub-model with frozen chemistry and with heat release to generate interfacial heat transfer profiles. Positive and negative logarithmic sensitivities indicate downstream and upstream flame movement, respectively, to a positive perturbation of the boundary condition. Both models are sensitive to the wall temperature boundary condition. The influence of T_w on the model with the reactive boundary layer is particularly strong due to the shallower wall temperature gradient at its stabilization position. Therefore, the error bars in Figure 4.7 are strongly dependent on the uncertainty in the axial wall temperature gradient.

A similar analysis can be done on fast and slowly propagating flames in a participating channel. The impact of operating parameters, solid properties and boundary conditions are shown in Figure E.2. At the set wall temperature, it is the inner wall radius which controls

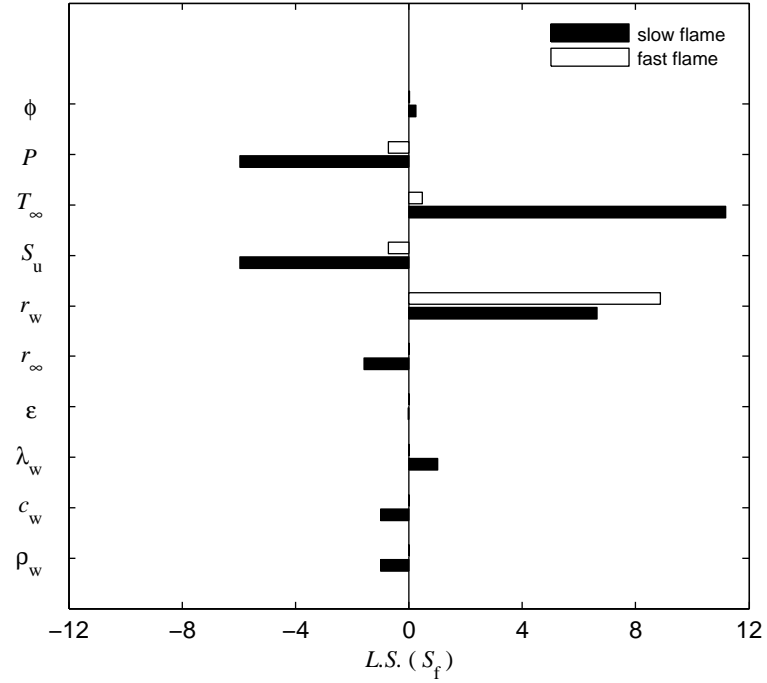


Figure E.2 Flame propagation speed logarithmic sensitivities to the boundary conditions for freely-propagating slow fast (white) and slow (white) flames, $Le = 1.0$, $\phi = 1.0$, $T_\infty = 1100$ K.

propagation speed for the fast propagating flame. Such flames are sensitive to heat loss, therefore a larger diameter channel would raise the propagation speed considerably. Slowly propagating flames are sensitive to heat recirculation. This is seen in the wall properties λ_w , c_w and ρ_w , where thermal conductivity enhances propagation speed while an increase in volumetric heat capacity, $(\rho c)_w$, diminishes it. However, it is the boundary conditions T_∞ , r_w , p and S_u which have controlling influence on propagation speed.

Appendix F

Flame Simulations

A numerical code was developed as part of this thesis to predict 1-D volumetric temperature, velocity and species profiles for burner-stabilized and freely-propagating flames inside a tubular channel. The underlying code is built as a collection C++ objects that are integrated with CANTERA [85] for thermo-chemical calculations, with the GNU Scientific Library (GSL) [111] for mathematical functions, and with the SUNDIALS [100] suite of differential equation solvers. To facilitate ease-of-use, these objects are controlled with a PYTHON “flat interface” to give a user access to solution routines and parameters at a high-level. These routines are found in the code in the files `onedim.py`, `BurnerTubeFlame.py` and `FreeTubeFlame.py`, and in the files `BurnerTubeExtensions.py` and `FreeTubeExtensions.py` in solution directories.

F.1 Flame solution scripts

PYTHON scripts are presented below to demonstrate how simulations were performed. Examples are shown for a burner-stabilized case and a freely-propagating case with a participating wall, in Figure F.1 and Figure F.2, respectively. Procedures for both cases follow the same general approach. First, a coarse solution is obtained from an initial guess assuming Newton’s Law of Cooling and a constant Nusselt number. The solution is, then, refined with successive grid refinements until the heat source profile is well resolved. After refinement, a continuation methodology is implemented to slowly convert the formulation to one with uses the boundary layer sub-model for the interfacial heat transfer profile. This

second solution is then refined again, typically to greater than 1500 grid points, to ensure good convergence.

```
#####
#
# BURNER_TUBE_FLAME - A stabilized, premixed methane/air flat
# flame in a steady monotonically increasing wall temperature
# profile
#
from Cantera import *
from Cantera.OneD import *
from Cantera.OneD.BurnerTubeFlame import BurnerTubeFlame
from BurnerTubeExtensions import *

#####
#
# parameters
#
p          = OneAtm          # pressure
tin         = 300.0           # unburned gas temperature
Su          = 1.0             # average inlet velocity [m/s]
Nu          = 4.0             # average Nusselt number []
D           = 0.001           # tube diameter [m]

comp        = 'CH4:1.0, O2:2.0, N2:7.52' # premixed gas composition

locGuess     = 0.65           # flame location guess
                                # percentage of grid

wall_temp_file = 'tdata.dat'

tol_ss       = [1.0e-6, 1.0e-13] # [rtol atol] for steady-state
                                # problem
tol_ts       = [1.0e-6, 1.0e-13] # [rtol atol] for time stepping

loglevel     = 2              # amount of diagnostic output (0
                                # to 5)

#####
# Setup the run

# make the initial grid - set a refined zone of ngrids between z0 and z2
initial_grid = makeSmoothGrid1D(z0 = 0.365, z2 = 0.374, zmax = 0.5715, ngrids = 500, dz_ends = 0.001)

# create the gas object
gas = importPhase('gri30.cti', 'gri30_mix')

# set its state to that of the unburned gas at the burner
gas.set(T = tin, P = p, X = comp)

rho_u = gas.density()

# initialize the burner and set its properties
f = BurnerTubeFlame(gas = gas, grid = initial_grid)
f.burner.set(massflux = rho_u*Su, mole_fractions = comp, temperature = tin)

# read in the fixed temperature profile
[zloc, tvalues] = getData(wall_temp_file)

# set the temperature profile to the values read in
f.flame.setFixedWallTempProfile(zloc, tvalues)

# set the wall values
f.flame.setD(D)

# set solution parameters
f.setMaxJacAge(50, 50)
f.setTimeStep(1.0e-5, [5, 10, 20, 50])
```

Figure F.1 Script for a flame stabilized in a monotonically varying wall temperature profile.


```
#####
#
# initially solve the flame with a constant Nusselt number
#
f.set(tol = tol_ss, tol_time = tol_ts)

# set-up the initial guess
f.init2(loglevel = loglevel, z1 = locGuess, grid = initial_grid, zwall = zloc, twall = tvalues)

f.flame.setNu(Nu)

# restore the solution
f.restoreSolution(loglevel = loglevel, filename = filename+'_input', id = 'coarse', zloc = zloc, tvalues = tvalues)

print '#####'
print 'Do initial calculation...'

print '.....'
print 'Solving... Energy off, no refinement.'

f.set(energy = 'off')
f.setRefineCriteria(ratio = 10.0, slope = 1, curve = 1)
f.setMaxJacAge(50, 50)
f.setTimeStep(1.0e-5, [1, 2, 5, 10, 20])

f.solve(loglevel, 1)
f.save('burner_tube_flame_init_0.xml', 'no_energy',
      'solution with the energy equation disabled')

f.showSolution()

print '.....'
print 'Solving... Energy on, no refinement.'

ratio = 3.0                # initial refinement parameters
slope = 0.1
curve = 0.1

f.set(energy = 'on')
f.setRefineCriteria(ratio = ratio, slope = slope, curve = curve)
f.solve(loglevel, 1)
f.solve(loglevel, 1)      # solve again just to be sure

f.save('burner_tube_flame_init_0.xml', 'energy',
      'solution with the energy equation disabled')

f.showSolution()

#####
#
# Switch on the interfacial heat transfer model
#

# set-up the radial grid
[grid, delr] = makeSmoothRadialGrid(D = D)

qwall_frac = 0.0
for i in range(0, 20):

    del_qwall_frac = 0.05      # step in 5% increments

    f.setTimeStep(1.0e-5, [100, 50])
    f.setTimeStepLimits(1.0e-20, 1.0e-4)

    qwall_frac += del_qwall_frac
```

Figure F.1 Burner-stabilized flame script, continued.

```

if (i >= 1):

    # reset the burner object
    print '#####'
    print 'Reset burner object:'

    # set its state to that of the unburned gas at the burner
    gas.set(T = tin, P = p, X = comp)
    rho_u = gas.density()

    # initialize the burner and set its properties
    f = BurnerTubeFlame(gas = gas, grid = initial_grid)
    f.burner.set(massflux = rho_u*Su, mole_fractions = comp, temperature = tin)

    # set the wall values
    f.flame.setD(D)
    f.flame.setNu(Nu)

    # set solution parameters
    f.setMaxJacAge(50, 50)

    f.set(tol = tol_ss, tol_time = tol_ts)

    # restore solution from previous run
    ext = '.xml'
    id = 'coarse'

    print '.....'
    print 'Restoring solution:'+'burner_tube_flame_qwall'+str(i-1)+ext

    f.restore('burner_tube_flame_qwall'+str(i-1)+ext,id)
    f.flame.setFixedWallTempProfile(zloc, tvalues)
    f._initialized = 1

    # reassert coarse solution in memory

    print '.....'
    print 'Solving... Energy off, no refinement.'

    f.set(energy = 'off')
    f.setTimeStep(1.0e-5, [50, 10])
    f.solve(loglevel,0)
    f.solve(loglevel,0)

    print '.....'
    print 'Solving... Energy on, no refinement.'

    f.flame.setNuCalcFlag(6)          # there are different heat transfer models
                                     # this is the latest one
    f.flame.setNuRadialGrid(rgrid,delr)

    f.flame.setQrxnCalcFlag(1)        # update the heat source profile
    f.flame.setNuQrxnFrac(1.0)        # no qrxn attenuation
    f.flame.setNuQwallFrac(qwall_frac-del_qwall_frac)
    f.flame.setNuQrxnConv(2)         # there are different convolution profiles
                                     # this one is for the zeta model
    f.flame.setNuQrxnConvLe(1.0)

    f.set(energy = 'on')
    f.setTimeStep(1.0e-5, [1000, 500])
    f.setTimeStepLimits(1.0e-20, 1.0e-5)
    f.solve(loglevel,0)
    f.solve(loglevel,0)

    print 'SUCCESS - Solution '+'burner_tube_flame_qwall'+str(i-1)+ext+' restored.'

    f.saveSolutionCSV(filename = 'burner_tube_flame_wall'+str(i-1), ext = '_restored.csv')

```

Figure F.1 Burner-stabilized flame script, continued.

```

# regrid the solution
delzf = 5.0e-4 # half a flame thickness
iter = 0

fg = 1
while (fg > 0):

    f.regrid(loglevel = loglevel, delz01 = 0.003, delz12 = 0.006, dz_min = 1.81e-5)

    f.saveSolutionCSV('regrid_debug'+str(iter))
    iter += 1

    [zf_0,jf_0] = f.findGridMaxTemp()

    tol_ss = [r_tol_ss[i-1], a_tol_ss[i-1]] # [rtol atol] for steady-state
                                              # problem
    tol_ts = [r_tol_ts[i-1], a_tol_ts[i-1]] # [rtol atol] for time stepping

    f.set(tol = tol_ss, tol_time = tol_ts)

    #f.setRefineCriteria(ratio = ratio[i-1], slope = slope[i-1], curve = curve[i-1], prune = prune[i-1])

    f.setTimeStep(1.0e-5, [50, 10])
    f.doEnergyOffSolution(loglevel = loglevel, refine_grid = 0, filename = 'regrid_soln_qwall'+str(qwall_frac[i-1]))

    f.setTimeStep(1.0e-5, [4000, 1000])
    f.setTimeStepLimits(1.0e-20, 1.0e-5)
    f.doEnergyOnSolution(loglevel = loglevel, refine_grid = 0, filename = 'regrid_soln_qwall'+str(qwall_frac[i-1]))

    [zf_1,jf_1] = f.findGridMaxTemp()

    if abs(zf_0 - zf_1) < delzf:
        fg = 0

print '#####'
print 'Step Qwall (mixture averaged formulation):'
print 'Qwall = '+str(qwall_frac[i])

f.flame.setNuCalcFlag(6) # there are different heat transfer models
                        # this is the latest one
f.flame.setNuRadialGrid(rgrid,delr)

f.flame.setQrxnCalcFlag(1) # update the heat source profile
f.flame.setNuQrxnConvThickness(0.0) # uniform radial heat release
f.flame.setNuQrxnFrac(1.0) # no qrxn attenuation
f.flame.setNuQwallFrac(qwall_frac[i])
f.flame.setNuQrxnConv(2) # there are different convolution profiles
                        # this one is for the zeta model

f.flame.setNuQrxnConvLe(1.0)

f.set(tol = tol_ss, tol_time = tol_ts)

f.setTimeStep(1.0e-5, [10000, 1000])
f.setTimeStepLimits(1.0e-20, 1.0e-5)
f.doEnergyOnSolution(loglevel = loglevel, refine_grid = 0, filename = 'burner_tube_flame_qwall'+str(i))

f.showSolution()

# refine the grid one final time
print '#####'
print 'Finish up solution...'

ratio = 3.0 # new refinement parameters
slope = 0.05
curve = 0.05

f.set(energy = 'on')
f.setRefineCriteria(ratio = ratio, slope = slope, curve = curve)
f.solve(loglevel, 1)
f.solve(loglevel, 1)

f.save('burner_tube_flame.xml','energy',
      'solution with the energy equation enabled')
f.saveSolutionCSV('burner_tube_flame')

f.showSolution()

```

Figure F.1 Burner-stabilized flame script, continued.

```
#####
#
# FREE_TUBE_FLAME - A freely-propagating, premixed methane/air flat
# flame propagating in a channel with thermally participating
# walls
#
from Cantera import *
from Cantera.OneD import *
from Cantera.OneD.FreeTubeFlame import FreeTubeFlame
from FreeTubeExtensions import *

#####
#
# parameters
#
p          = OneAtm          # pressure
tin        = 1100.0          # unburned gas temperature
D          = 0.002           # inner tube diameter
t          = 0.0005          # tube thickness
rho_w      = 2650.0          # wall density
cp_w       = 750.0           # wall heat capacity
tcon_w     = 1.1             # wall thermal conductivity
eps        = 0.93            # wall emissivity

comp       = 'CH4:1.0, O2:2.0, N2:7.52' # premixed gas composition

# make the initial grid - set a refined zone of ngrids between z0 and z2
initial_grid = makeSmoothGrid1D(z0 = 0.018, z2 = 0.022, zmax = 0.06, ngrids = 500, dz_ends = 0.001)

tol_ss     = [1.0e-5, 1.0e-9] # [rtol atol] for steady-state
# problem
tol_ts     = [1.0e-4, 1.0e-6] # [rtol atol] for time stepping

loglevel   = 2                # amount of diagnostic output (0
# to 5)

gas = importPhase('gri30.cti','gri30_mix')

# set its state to that of the unburned gas
gas.setState_TPX(tin, p, comp)

rho_inlet = gas.density()

# initialize the flame - for an isothermal wall set wall to 0
f = FreeTubeFlame(gas = gas, grid = initial_grid, tfix = tin+300.0, wall = 1)

# set the upstream properties
f.setInlet(mole_fractions = comp, temperature = tin)

# set the solution tolerances
f.set(tol = tol_ss, tol_time = tol_ts)

# set the initial guess
f.init()

f.showSolution()

f.set(energy = 'off')
f.setRefineCriteria(ratio = 10.0, slope = 1, curve = 1)
f.setMaxJacAge(50, 50)
f.setTimeStep(1.0e-5, [1, 2, 5, 10, 20])

f.solve(loglevel, 1)
f.save('free_tube_flame_init.0.xml','no_energy',
      'solution with the energy equation disabled')
```

Figure F.2 Script for a freely-propagating flame in a participating channel.

```
#####
#
# initially solve the flame with a constant Nusselt number
# turn on interfacial heat transfer slowly...
#
ratio = 3.0          # initial refinement parameters
slope = 0.1
curve = 0.1

f.setWall(D_in = D, D_out = D+2*t, Nu = 0.001, thermal_conductivity = tconw, specific_heat = cpw, density = rhow)
f.set(energy = 'on')
f.setRefineCriteria(ratio = ratio, slope = slope, curve = curve)
f.solve(loglevel, 1)

print '#####'
print 'Step Nu (mixture averaged formulation):'

Nu = [0.01, 0.1, 1.0, 2.0, 3.0, 3.5, 4.0]

for i in range(1,8):

    f.setWall(Nu = Nu[i])
    f.set(energy = 'on')
    f.setRefineCriteria(ratio = ratio, slope = slope, curve = curve)
    f.solve(loglevel, 1)

# add the radiation loss
f.setWall(emissivity = eps)
f.set(energy = 'on')
f.setRefineCriteria(ratio = ratio, slope = slope, curve = curve)
f.solve(loglevel, 1)

# save initial solution: Su = 0.0, Nu = 4.0, eps = 0.93
f.save('free_tube_flame_init_0.xml', 'energy',
      'solution with the energy equation enabled')
f.saveSolutionCSV('free_tube_flame_init_0')

print '#####'
print 'Step Su (mixture averaged formulation):'

# now slowly increase the inlet velocity to Su = 1.5 m/s
u_inlet = 0.0
for i in range(1,16):

    # make decisions based on propagation speed Sf
    u = f.u()

    if u[0] > 0.1:

        # take large steps in velocity
        delta_u = 0.01

    elif u[0] > 0.02:

        # keep going but restrict the time step size
        f.setTimeStep(1.0e-5, [1000, 500])
        f.setTimeStepLimits(1.0e-20, 1.0e-3)

        # small steps in velocity
        delta_u = 0.001

    else:

        # keep going but restrict the time step size
        f.setTimeStep(1.0e-5, [1000, 500])
        f.setTimeStepLimits(1.0e-20, 1.0e-3)

        # small steps in velocity
        delta_u = 0.0005

    u_inlet += delta_u

# set the new mass flow rate
f.setInlet(massflux = rho_inlet*u_inlet)

f.set(energy = 'on')
f.setRefineCriteria(ratio = ratio, slope = slope, curve = curve)
f.solve(loglevel, refine_grid)

f.save('free_tube_flame_init_'+str(i)+'.xml', 'energy',
      'solution with the energy equation enabled')
f.saveSolutionCSV('free_tube_flame_init_'+str(i))

f.showSolution()
```

Figure F.2 Freely-propagating flame script, continued.

```

# refine the grid

ratio = 3.0                      # new refinement parameters
slope = 0.02
curve = 0.02

f.set(energy = 'on')
f.setRefineCriteria(ratio = ratio, slope = slope, curve = curve)
f.solve(loglevel, 1)

f.save('free_tube_flame_init_'+str(i)+'.xml','energy',
      'solution with the energy equation enabled')
f.saveSolutionCSV('free_tube_flame_init_'+str(i))

f.showSolution()

#####
#
# Switch on the interfacial heat transfer model
#

# set-up the radial grid
[rgrid,delr] = makeSmoothRadialGrid(D = D)

qwall_frac = 0.0
for i in range(0,100):

    del_qwall_frac = 0.01          # step in 1% increments

    f.setTimeStep(1.0e-5, [100, 50])
    f.setTimeStepLimits(1.0e-20, 1.0e-4)

    qwall_frac += del_qwall_frac

    print '#####'
    print 'Step Qwall (mixture averaged formulation):'
    print 'Qwall = '+str(qwall_frac)

    f.flame.setNuCalcFlag(6)          # there are different heat transfer models
                                     # this is the latest one
    f.flame.setNuRadialGrid(rgrid,delr)

    f.flame.setQrxnCalcFlag(1)        # update the heat source profile
    f.flame.setNuQrxnFrac(1.0)        # no qrxn attenuation
    f.flame.setNuQwallFrac(qwall_frac)
    f.flame.setNuQrxnConv(2)          # there are different convolution profiles
                                     # this one is for the zeta model
    f.flame.setNuQrxnConvLe(1.0)      # set the effective Lewis number

    f.set(tol = tol_ss, tol_time = tol_ts)

    f.set(energy = 'on')
    f.solve(loglevel, 0)              # solve with no refinement

    f.saveSolutionCSV('free_tube_flame_qwall'+str(qwall_frac))
    f.save('free_tube_flame_qwall'+str(qwall_frac)+'.xml','energy')

# refine the grid one final time
print '#####'
print 'Finish up solution...'

ratio = 3.0                      # new refinement parameters
slope = 0.008
curve = 0.008

f.set(energy = 'on')
f.setRefineCriteria(ratio = ratio, slope = slope, curve = curve)
f.solve(loglevel, 1)
f.solve(loglevel, 1)

f.save('free_tube_flame.xml','energy',
      'solution with the energy equation enabled')
f.saveSolutionCSV('free_tube_flame')

f.showSolution()

```

Figure F.2 Freely-propagating flame script, continued.

References

- [1] DR Hardesty and FJ Weinberg. Burners producing large excess enthalpies. *Combust. Sci. Tech.*, 8:201–14, 1974.
- [2] Y Ju and B Xu. Theoretical and experimental studies on mesoscale flame propagation and extinction. *Proc. Combust. Inst.*, 30:2445–53, 2005.
- [3] KT Kim, DH Lee, and S Kwon. Effects of thermal and chemical surface-flame interaction on flame quenching. *Combust. Flame*, 146:19–28, 2006.
- [4] J Daou and M Matalon. Flame propagation in poiseuille flow under adiabatic conditions. *Combust. Flame*, 124:337–49, 2001.
- [5] GP Smith, DM Golden, M Frenklach, NW Moriarty, B Eiteneer, M Goldenberg, CT Bowman, RK Hanson, S Song, WC Gardiner, VV Lissianski, and Z Qin. GRI-Mech 3.0. http://www.me.berkeley.edu/gri_mech/.
- [6] DB Spalding. A theory of inflammability limits and flame-quenching. *Proc. Royal Society A*, 240(1220):83–100, 1957.
- [7] H Leuenberger and RA Person. Compilation of radiation shape factors for cylindrical assemblies. In *ASME*, pages 56–144, 1956.
- [8] SN Rea. Rapid method for determining concentric cylinder radiation view factors. *AIAA J.*, 13(8):1122–3, 1975.
- [9] CP Tso and SP Mahulikar. View factors between finite length rings on an interior cylindrical shell. *J. Thermophys. Heat Trans.*, 13:375–9, 1999.
- [10] K Maruta. Micro and mesoscale combustion. *Proc. Combust. Inst.*, 33, 2010. in press.
- [11] H Davy. Some researches on flame. *Phil. Trans. Royal Soc. London*, page 45, 1817.
- [12] K Kuo. *Principles of Combustion*. John Wiley, 1986.

-
- [13] FJ Weinberg. Combustion Temperatures: The Future? *Nature*, 233:239–41, 1971.
 - [14] NI Kim and K Maruta. A numerical study on propagation of premixed flames in small tubes. *Combust. Flame*, 146:283–301, 2006.
 - [15] VS Babkin. Filtration combustion of gases. Present state of affairs and prospects. *Pure Appl. Chem.*, 65(2):335–44, 1993.
 - [16] T Takeno and K Sato. An excess enthalpy flame theory. *Combust. Sci. Tech.*, 20: 73–84, 1979.
 - [17] SA Lloyd and FJ Weinberg. A burner for mixtures of very low heat content. *Nature*, 251, 1974.
 - [18] AR Jones, SA Lloyd, and FJ Weinberg. Combustion in Heat Exchangers. *P. Roy. Soc. A-Math. Phys.*, 360(1700):97–115, 1978.
 - [19] C-H Chen and PD Ronney. Three-dimensional effects in counterflow heat-recirculating combustors. *Proc. Combust. Inst.*, 33(2):3285–91, 2011.
 - [20] MJ Dixon, I Schoegl, CB Hull, and JL Ellzey. Experimental and numerical conversion of liquid heptane to syngas through combustion in porous media. *Combust. Flame*, 154:217–31, 2008.
 - [21] CH Smith, DM Leahey, LE Miller, and JL Ellzey. Conversion of wet ethanol to syngas via filtration combustion: An experimental and computational investigation. *Proc. Combust. Inst.*, 33(2):3317–24, 2011.
 - [22] B Lemke, C Roodhouse, N Glumac, and H Krier. Hydrogen synthesis via combustion of fuel-rich natural gas/air mixtures at elevated pressure. *Int. J. of Hydrogen Energy*, 30(8):893–902, 2005.
 - [23] S Zhdanok, LA Kennedy, A Lawrence, and G Koester. Superadiabatic combustion of methane air mixtures under filtration in a packed bed. *Combust. Flame*, 100(1-2): 221–31, 1995.
 - [24] JP Bingue, AV Saveliev, and Kennedy LA. Hydrogen production in ultra-rich filtration combustion of methane and hydrogen sulfide. *Int. J. Hydrogen Energy*, 27(6): 643–49, 2002.
 - [25] RS Dhamrat and JL Ellzey. Numerical and experimental study of the conversion of methane to hydrogen in a porous media reactor. *Combust. Flame*, 144:698–709, 2006.
 - [26] I Schoegl and JL Ellzey. Superadiabatic combustion in conducting tubes and heat exchangers of finite length. *Combust. Flame*, 151:142–59, 2007.

-
- [27] I Schoegl, SR Newcomb, and JL Ellzey. Ultra-rich combustion in parallel channels to produce hydrogen-rich syngas from propane. *Int. J. Hydrogen Energy*, 34(12): 5152–63, 2009.
- [28] I Schoegl and JL Ellzey. A mesoscale fuel reformer to produce syngas in portable power systems. *Proc. Combust. Inst.*, 32:3223–30, 2009.
- [29] I Schoegl and JL Ellzey. Numerical Investigation of Ultra-Rich Combustion in Counter Flow Heat Exchangers. *Combust. Sci. Tech.*, 182(10):1413–28, 2010.
- [30] A Mehra, X Zhang, AA Ayon, IA Waitz, MA Schmidt, and CM Spadaccini. A six wafer combustion system for a silicon micro gas turbine engine. *J. Microelec. Sys.*, 9:517–27, 2000.
- [31] Fu K, AJ Knobloch, FC Martinez, DC Walther, C Fernandez-Pello, and AP Pisano. Design and experimental results of small-scale rotary engines. *ASME Micro-Electromechanical Systems Division Publication (MEMS)*, 2001.
- [32] RJ Kee, H Zhu, AM Suresh, and GS Jackson. Solid Oxide Fuel Cells: Operating Principles, Current Challenges, and the Role of Syngas. *Combustion Science and Technology*, 180(6):1207–1244, 2008.
- [33] Z Shao, SM Haile, J Ahn, PD Ronney, Z Zhan, and SA Barnett. A thermally self-sustained micro solid-oxide fuel-cell stack with high power density. *Nature*, 435(7043): 795–8, 2005.
- [34] Y Ju and K Maruta. Microscale combustion: Technology development and fundamental research. *Progress in Energy and Combustion Science*, 37(6):669–715, 2011.
- [35] RA Yetter, V Yang, MH Wu, Y Wang, D Milius, and IA Aksay. *Combustion issues and approaches for chemical microthrusters*. Begell House, 2007.
- [36] R Srinivasan, IM Hsing, PE Berger, KF Jensen, SL Firebaugh, and MA Schmidt. Micromachined reactors for catalytic partial oxidation reactions. *AIChE J.*, 43(11): 3059–69, 1997.
- [37] TT Leach and CP Cadou. The role of structural heat exchange and heat loss in the design of efficient silicon micro-combustors. *Proceedings of the Combustion Institute*, 30(2):2437–2444, 2005.
- [38] GA Fateev, OS Rabinovich, and MA Silenkov. Oscillatory combustion of a gas mixture blown through a porous medium or a narrow tube. *Proc. Combust. Inst.*, 27: 3147–53, 1998.

-
- [39] OS Rabinovich, AV Fefelov, and NV Pavlyukevich. Modeling of premixed gas combustion in porous media composed of coarse-sized particles: 1-D description with discrete solid phase. *Proc. Combust. Inst.*, 29:3383–9, 1996.
 - [40] CL Hackert, JL Ellzey, and OA Ezekoye. Combustion and heat transfer in model two-dimensional porous burners. *Combust. Flame*, 116:177–91, 1999.
 - [41] DG Norton and DG Vlachos. A CFD study of propane/air microflame stability. *Combust. Flame*, 138:97–107, 2004.
 - [42] VN Kurdyumov, G Pizza, CE Frouzakis, and J Mantzaras. Dynamics of premixed flames in a narrow channel with a step-wise wall temperature. *Combust. Flame*, 156:2190–2200, 2009.
 - [43] G Pizza, CE Frouzakis, J Mantzaras, AG Tomboulides, and K Boulouchos. Dynamics of premixed hydrogen/air flames in microchannels. *Combust. Flame*, 152:433–50, 2008.
 - [44] G Pizza, CE Frouzakis, J Mantzaras, AG Tomboulides, and K Boulouchos. Dynamics of premixed hydrogen/air flames in mesoscale channels. *Combust. Flame*, 155:2–20, 2008.
 - [45] GG Pizza, CE Frouzakis, J Mantzaras, AG Tomboulides, and K Boulouchos. Three-dimensional simulations of premixed hydrogen/air flames in microtubes. *J. Fluid Mech.*, 658:463–91, 2010.
 - [46] K Maruta, T Kataoka, NI Kima, S Minaev, and R Fursenko. Characteristics of combustion in a narrow channel with a temperature gradient. *Proc. Combust. Inst.*, 30:2429–36, 2005.
 - [47] S Minaev, K Maruta, and R Fursenko. Nonlinear dynamics of flame in a narrow channel with a temperature gradient. *Combust. Theor. Model.*, 11(2):187–203, 2007.
 - [48] Y Tsuboi, T Yokomori, and K Maruta. Lower limit of weak flame in a heated channel. *Proc. Combust. Inst.*, 32:3075–81, 2009.
 - [49] VV Zamashchikov. An investigation of gas combustion in a narrow tube. *Combust. Sci. Tech.*, 166:1–14, 2001.
 - [50] VV Zamashchikov. Experimental investigation of gas combustion regimes in narrow tubes. *Combust. Flame*, 108:357–9, 1997.
 - [51] GL Dugger, S Heimel, and RC Weast. Flame velocity and preflame reaction in heated propane-air mixtures. *Ind. Eng. Chem.*, 47(1):114–6, 1955.

-
- [52] Y Ju and B Xu. Effects of Channel Width and Lewis Number on the Multiple Flame Regimes and Propagation Limits in Mesoscale. *Combust. Sci. Tech.*, 178(10):1723–53, 2006.
- [53] YM Laevskii and VS Babkin. Seepage Gas Combustion. *Combust. Explo. Shock.*, 23(5):531–547, 1988.
- [54] YM Laevskii, VS Babkin, and VI Drobyshevich. Theory of filtration combustion of gases. *Fiz. Goreniya Vzryva*, 20(6):591–600, 2006.
- [55] M Kaviani. *Principles of Heat and Mass Transfer in Porous Media*. Springer-Verlag, New York, second edition, 1995.
- [56] MR Henneke and Ellzey JL. Modeling of filtration combustion in a packed bed. *Combust. Flame*, 117:832–40, 1999.
- [57] N Kaisare and D Vlachos. Optimal reactor dimensions for homogeneous combustion in small channels. *Catalysis Today*, 120(1):96–106, 2007.
- [58] H Oshibe, H Nakamura, T Tezuka, S Hasegawa, and K Maruta. Stabilized three-stage oxidation of DME/air mixture in a micro flow reactor with a controlled temperature profile. *Combust. Flame*, 157(8):1572–1580, 2010.
- [59] TT Leach, CP Cadou, and GS Jackson. Effect of structural conduction and heat loss on combustion in micro-channels. *Combust. Theor. Model.*, 10(1):85–103, 2006.
- [60] L Graetz. ber die wrmeleitus der fhigkeit von flssigkeiten. *Annalen der Physik and Chemie*, 18:79–94, 1883.
- [61] LA Kennedy, JP Bingue, AV Saveliev, AA Fridman, and SI Foutzo. Chemical structures of methane-air filtration combustion waves for fuel-lean and fuel rich conditions. *Proc. Combust. Inst.*, 28:1431–8, 2000.
- [62] JP Bingue, AV Saveliev, and LA Kennedy. NO reburning in ultrarich filtration combustion of methane. *Proc. Combust. Inst.*, 31(2):3417–24, 2007.
- [63] AJ Barra, G Diepvens, JL Ellzey, and MR Henneke. Numerical study of the effects of material properties on flame stabilization in a porous burner. *Combust. Flame*, 134(4):369–79, 2003.
- [64] AJ Barra and JL Ellzey. Heat recirculation and heat transfer in porous burners. *Combust. Flame*, 137(1-2):230–41, 2004.
- [65] N Wakao and F Kaguei. *Heat and Mass Transfer in Packed Beds*. Gordon and Breach Science Publications, New York, 1982.

-
- [66] A Veeraragavan and C Cadou. Theoretical study of conjugate heat transfer effects on temperature profiles in parallel flow with embedded heat sources. *Int. J. Heat Mass Transfer*, 53(9-10):1699–1711, 2010.
- [67] A Veeraragavan and C Cadou. Flame Speed Predictions in Planar Micro / Mesoscale Combustors with Conjugate Heat Transfer. *Combust. Flame*.
- [68] NS Kaisare. A review on microcombustion: Fundamentals, devices and applications. *Progress in Energy and Combustion Science*, 38(3):321–359, 2012.
- [69] M Short and DA Kessler. Asymptotic and numerical study of variable-density premixed flame propagation in a narrow channel. *J. Fluid Mech.*, 638:305, 2009.
- [70] Basic considerations in the combustion of hydrocarbon flames in air. Technical report, National Advisory Committee for Aeronautics, 1957. NACA Report 1300.
- [71] J Daou and M Matalon. Influence of conductive heat-losses on the propagation of premixed flames in channels. *Combust. Flame*, 128:321–39, 2002.
- [72] K Maruta, JK Parc, KC Oh, T Fujimori, SS Minaev, and RV Fursenko. Characteristics of Microscale Combustion in a Narrow Heated Channel. *Combust. Explo. Shock.*, 40(5):516–23, 2004.
- [73] Y Fan, Y Suzuki, and N Kasagi. Experimental study of micro-scale premixed flame in quartz channels. *Proc. Combust. Inst.*, 32:3083–90, 2010.
- [74] Y Fan, Y Suzuki, and N Kasagi. Quenching mechanism study of oscillating flame in micro channels using phase-locked OH-PLIF. *Proc. Combust. Inst.*, 33:3267–73, 2010.
- [75] A Fan, SS Minaev, EV Sereshchenko, Y Tsuboi, H Oshibe, H Nakamura, and K Maruta. Dynamic behavior of splitting flames in a heated channel. *Combust. Explo. Shock.*, 45(3):245–250, 2009.
- [76] SS Minaev, EV Sereshchenko, RV Fursenko, A Fan, and K Maruta. Splitting flames in a narrow channel with a temperature gradient in the walls. *Combust. Explo. Shock.*, 45(2):119–125, 2009.
- [77] A Yamamoto, H Oshibe, H Nakamura, T Tezuka, S Hasegawa, and K Maruta. Stabilized three-stage oxidation of gaseous n-heptane/air mixture in a micro flow reactor with a controlled temperature profile. *Proceedings of the Combustion Institute*, 33(2):3259–66, 2011.

- [78] M Hori, A Yamamoto, H Nakamura, T Tezuka, S Hasegawa, and K Maruta. Study on octane number dependence of PRF/air weak flames at 1–5 atm in a micro flow reactor with a controlled temperature profile. *Combustion and Flame*, 159(3):959–967, 2011.
- [79] RJ Kee, ME Coltrin, and P Glarborg. *Chemically Reacting Flow: Theory and Practice*. John Wiley, New York, 2003.
- [80] RJ Kee, Grcar JF, Smooke MD, and Miller JA. A FORTRAN Program for Modeling Steady Laminar One-Dimensional premixed flames. Technical report, Sandia National Laboratories, 1985.
- [81] R Seiser, H Pitsch, K Seshadri, WJ Pitz, and HJ Curran. Extinction and autoignition of n-heptane in counterflow configuration. *Proc. Combust. Inst.*, 28:2029–37, 2000.
- [82] CK Westbrook. Chemical kinetics of hydrocarbon ignition in practical combustion systems. *Proc. Combust. Inst.*, 28(2):1563–77.
- [83] JM Bergthorson and PE Dimotakis. Premixed laminar C₁-C₂ stagnation flames: Experiments and simulations with detailed thermochemistry models. *Proc. Combust. Inst.*, 31:1139–47, 2007.
- [84] GMG Watson and JM Bergthorson. The effect of mixture composition on stabilized flames in a meso-scale channel with a wall temperature gradient. In *23rd International Colloquium on the Dynamics of Explosions and Reactive Systems (ICDERS 2011)*, page 237, 2011.
- [85] DG Goodwin. An open-source, extensible software suite for CVD process simulation. In *Proceedings of CVD XVI and EuroCVD Fourteen*, pages 155–62. Electrochemical Society, 2003.
- [86] M Frenklach, H Wang, C-L Yu, M Goldenberg, CT Bowman, RK Hanson, DF Davidson, EJ Chang, GP Smith, DM Golden, WC Gardiner, and V Lissianski. GRI-Mech 1.2, 1995. http://www.me.berkeley.edu/gri_mech/.
- [87] San Diego Mechanism, 2005. <http://maeweb.ucsd.edu/~combustion/cermech/index.html>.
- [88] SG Davis, CK Law, and H Wang. Propene pyrolysis and oxidation kinetics in a flow reactor and laminar flames. *Combust. Flame*, 119(4):375–399, 1999.
- [89] LJM Benezech. Premixed hydrocarbon stagnation flames: experiments and simulations to validate combustion chemical-kinetic models. Master’s thesis, California Institute of Technology, 2008.
- [90] GMG Watson and JM Bergthorson. The effect of chemical energy release on heat transfer from flames in small channels. *Combustion and Flame*, 159(3):1239–52, 2011.

-
- [91] SV Pantakar. *Numerical heat transfer and fluid flow, First Edition*. McGraw-Hill, New York, 1980.
- [92] T Coffee and JM Heimerl. Transport algorithms for premixed laminar, steady-state flames. *Combust. Flame*, 43:273–89, 1981.
- [93] NN Yanenko. *The Method of Fractional Steps*. Springer, New York, 1971.
- [94] CK Westbrook and FL Dryer. Simplified reaction mechanisms for the oxidation of hydrocarbon fuels in flames. *Combust. Sci. Technol.*, 27:31–43, 1981.
- [95] S Kumar. Numerical studies on flame stabilization behavior of premixed methane-air mixtures in diverging mesoscale channels. *Combust. Sci. Technol.*, 183:779–801, 2011.
- [96] A Kazakov and M Frenklach. <http://www.me.berkeley.edu/drm/>.
- [97] H Wang and M Frenklach. Detailed reduction of reaction mechanism for flame modeling. *Combust. Flame*, 87:365–70, 1991.
- [98] PH Paul and HN Najm. Planar laser-induced fluorescence imaging of flame heat release rate. *Proc. Combust. Inst.*, 27(3):43–50, 1998.
- [99] GP Gauthier, GMG Watson, and JM Bergthorson. An evaluation of numerical models for temperature-stabilized CH₄ / air flames in a small channel. *Combust. Sci. Tech.*, 2012. in press.
- [100] Suite of Nonlinear and Differential/Algebraic Equation Solvers (SUNDIALS), 2006. <https://computation.llnl.gov/casc/sundials/main.html>.
- [101] ME Coltrin, HK Moffatt, RJ Kee, and FM Rupley. CRESLAF - A program for modeling laminar chemically reacting boundary-layer flow in cylindrical or planar channels. Technical report, 2000.
- [102] KE Brenan, SL Campbell, and LR Petzold. *Numerical solution of initial-value problems in differential-algebraic equations*. North-Holland, 1989.
- [103] VV Zamashchikov and SS Minaev. Limits of flame propagation in a narrow channel with gas filtration. *Combust. Explo. Shock.*, 37(1):21–9, 2001.
- [104] C Chao, K Hui, W Kong, P Cheng, and J Wang. Analytical and experimental study of premixed methane air flame propagation in narrow channels. *Int. J. Heat Mass Tran.*, 50(7-8):1302–13, 2007.
- [105] JD Buckmaster and GSS Ludford. *Lectures on mathematical combustion*. Society for Industrial Mathematics, 1983.

-
- [106] B Xu and Y Ju. Experimental study of spinning combustion in a mesoscale divergent channel. *Proc. Combust. Inst.*, 31:3285–92, 2007.
 - [107] G Joulin and B Deshaies. On radiation-affected flame propagation in gaseous mixtures seeded with inert particles. *Combust. Sci. Tech.*, 47:299–315, 1986.
 - [108] RL Reid and JS Tennant. Annular ring view factors. *AIAA J.*, 11(10):1446–8, 1973.
 - [109] SS Katte and SP Venkateshan. Accurate Determination of View Factors in Axisymmetric Enclosures with Shadowing Bodies Inside. *J. Thermophys. Heat Trans.*, 14(1):68–76, 2000.
 - [110] E Mallard and HL LeChatelier. Combustion des melanges gazeux explosifs. *Ann. Mines*, 4:274–381, 1883.
 - [111] GNU Scientific Library (GSL), 2012. <http://www.gnu.org/software/gsl/>.